Coupled dislocation/dislocation and solute strengthening mechanisms in metal alloys

by

Yi Dong

M.Sc. in Engineering, Brown University, RI, 2010

M.Sc. in Applied Mathematics, Brown University, RI, 2009

M.Eng., University of Science and Technology of China, P.R.China,2006

B.Sc., University of Science and Technology of China, P.R.China, 2003

A dissertation submitted in partial fulfillment of the
requirements for the degree of Doctor of Philosophy
in the School of Engineering at Brown University

PROVIDENCE, RHODE ISLAND

May 2013

Abstract of " Coupled dislocation/dislocation and solute strengthening mechanisms in metal alloys " by Yi Dong, Ph.D., Brown University, May 2013

In most engineering metal alloys, the overall plastic resistance is contributed by two or more strengthening mechanisms operating simultaneously. Two major sources of strengthening in metal alloys are substitutional solutes and forest dislocations. Theoretical, experimental and numerical studies have been carried out and extensively explored the strengthening mechanism due to solid-solution or forest dislocation, whereas a clear understanding of how different strengthening mechanisms operate together to generate a macroscopically measured strength is missing. In this thesis, the hardening behavior containing solid-solution strengthening and forest dislocations strengthening is studied both numerically and theoretically. In order to study the basic scaling law proposed, $\tau^k = \tau_1^k + \tau_2^k$, in previous theories, with $1 \leq k \leq 2$, where τ_1 and τ_2 are the strengths of the two individual strengthening mechanisms, line-tension simulations of dislocation glide through two types of point obstacles are firstly performed to examine the friction limit. Our results show clearly that the applicability of the linear rule $k = 1$ is dependent on the relative density difference of two different strengthening mechanisms. When the obstacle spacing ratio is larger than 67, the friction limit ($k = 1$) is ensured. Because the studies of dislocation-obstacle interaction rely greatly on an accurate value of line tension of dislocation, a robust atomistic simulation approach is then proposed in this thesis to compute the line tension in FCC and HCP metals. Using this method, the requirements for an accurate line tension calculation at atomic scale are listed and the line tension for dislocation of edge and screw character in FCC aluminum and basal edge dislocation in HCP magnesium are computed, providing a reliable data set for further studies. The results and remaining unclarity in simulations on continuum scales inspire further studies of solute/dislocation-junction interaction at atomistic resolution. Therefore, we in this thesis realize massive atomistic simulations to investigate the formation and strength of dislocation junctions in FCC Al/Mg alloys. Compared with previous

dislocation dynamics results, the shielding effect due to solute atoms on dislocation-dislocation interaction is not observed at atomistic scale. More importantly, once the space between dislocation-junction remains fixed, the linear supposition rule ($k = 1$) has the ability to account for the combination of solute strengthening and dislocation-junction strengthening in metal alloys at atomistic scale, under which the individual strengthening contribution can be well defined by previous solute strengthening model. Once the overall strength due to multiple strengthening operating together is well evaluated at zero temperature, the thermally-activated plastic flow in the presence of multiple obstacle types is studied both numerically and theoretically in a regime of relative obstacle densities for which the zero-temperature stress is additive. The numerical methods consider the low-density "forest" obstacles first as point obstacles and then as extended obstacles having a finite interaction length with the dislocation, while the high-density "solute" obstacles are treated as point obstacles. Results show that the linear summation fails when a finite interaction width between dislocation and obstacles is considered. An analytical model for the activation energy versus flow stress is then proposed to account for the effect of the finite interaction length. The model predictions agree well with numerical results for a wide range of obstacle properties, showing clearly the effect due to the finite interaction between dislocation and the obstacles.

This dissertation by Yi Dong is accepted in its present form
by the School of Engineering as satisfying the
dissertation requirement for the degree of Doctor of Philosophy.

Date_____ _____
William A. Curtin, Director

Recommended to the Graduate Council

Date_____ _____
Allan F. Bower, Reader

Date_____ _____
Sharvan Kumar, Reader

Approved by the Graduate Council

Date_____ _____
Peter M. Weber, Dean of the Graduate School

The Vita of Yi Dong

Yi Dong was born in Kunming, China on December 12th, 1980. He was raised in Kunming for his entire child hood, along with his older sister Huanqing, by parents Baoman and Kanglai. Kunming, well known by its wonderful climate and mountain view offered a peaceful surrounding for Yi to grow and learn. He attended in Kunming No.1 High School and upon graduation Yi moved to Hefei, to attend University of Science and Technology of China (USTC). While at USTC, Yi studied Engineering with a specialty on Mechanics of Solids. Yi received a B.S. in Theoretical and Applied Mechanics in 2003 and M.E. in Mechanics of solids in 2006. In the Fall of 2006 Yi began his doctoral studies at Brown University in Providence, RI. During his time at Brown he has been a research assistant working in the field of solid mechanics.

Acknowledgments

I would like to express my special and tremendous thanks to my advisor, Professor William A. Curtin. With his encouragement, his inspiration, and his great efforts to explain things clearly and simply, he helped to make this thesis possible. To the entire Brown community and School of Engineering thank you for helping to make my learning experience one I will always remember.

I also want to deeply thank Professor Allan F. Bower and Professor Sharvan Kumar for being my thesis readers and defense committee members. This thesis could not have been completed without their wonderful suggestions to me. To all professors at Brown, thank you for teaching me the courses and introducing me to the field of solid mechanics and computational theories. They shed tremendous light on me and selflessly share their knowledge with me.

To my friends here in Providence you have truly made this home. Festivities, Fishing seasons, Summer Vocations and all other events have been unforgettable and warm because all of you. Specially thank Hongyuan Jiang for taking care of me when I landed on this place in 2006, knowing nothing about how to live in a foreign country. I also want to thank Jun Song, Sutee Olarnrithinun, Fabio Pavia, Thomas Nogaret and Ben Szajewski for their support and help in my graduate study. Special thanks go to Jun and Sutee, who supported me greatly when I was downside of my career. And for all the crews in Professor Curtin's group, the time we hang out in Lausanne made my last year being a student truly special and unforgettable.

Last, and most importantly, I need to thank my family. Without their support and love, this could have been impossible. Especially, I want to thank my girlfriend Jingjing, who has been always supporting me to chase my dream, encouraging me

when facing the toughness. I can not tell you enough how much you mean to me. You are now and always will be the best thing that happens in my life.

Contents

List of Tables

List of Figures

Chapter 1

Introduction

Metals and many important classes of nonmetallic solids are crystalline and the macroscopic mechanical behavior for these materials is essentially dominated by the movement and interaction between atoms arranged in certain crystal structure. Ideally, if the crystalline solid is perfect in a single-crystalline form, it is able to respond only in a reversible elastic manner with the applied load under the critical value which destabilize the crystal structure. However, unless the extreme case, all real crystalline solids usually contain point defects such as vacancies, line defects like dislocations, and planar defects such as grain boundaries. The presence and interaction between these imperfection significantly modify the material response. Among all defects, it is dislocation which offers means of producing plastic shear strain so that it serves as the principle "carrier" of plastic deformation. The primary interests in this thesis includes the dislocation motion inside the materials and the strengthening mechanisms widely used to raise the plastic resistance.

Extensive research has been carried out and showed that the plastic deformation in crystalline materials occurs by the glide of dislocations. The critical strength for the onset of the plastic deformation is then the stress required to move the dislocation. The principle of strengthening can be simply recognized as means to give the material a high intrinsic plastic resistance to begin with. In all materials, the

glide of the dislocations in their slip plane is resisted by a lattice resistance, which provides an intrinsic strengthening mechanism. However, except Body-Centered Cubic (BCC) metals, the lattice resistance in pure close-packed Face-Centered Cubic (FCC) and on the basal plane of Hexagonal Close-Packed (HCP) metals is normally very small and therefore the addition of second-phase obstacles into a crystalline solids to prevent the dislocation motion becomes an effective method of improving the plastic resistance of materials. The second-phase obstacles impede the motion of the dislocations by pinning them at discrete points of contacts with the obstacles until the latter are eventually sheared or overcome by the force of the dislocations pressing on them and consequentially increase the applied stress necessary for dislocation motion to cause plastic deformations. Normal strengthening mechanisms include solid-solution strengthening, strain hardening due to dislocation-dislocation interaction and precipitation hardening. The details of mechanics of strengthening by second-phase obstacles are crucial and have been widely studied at various scales, which will be discussed below. In most general case, the overall strength is however controlled by several different strengthening mechanism operating simultaneously. A typical example is substitutional solute atoms and forest dislocations both are present in metal alloys. Therefore, a clear understanding of how different strengthening mechanism operate together to generate a macroscopically-measure overall strength is required. In spite of considerable theoretical, numerical and experimental efforts over the course of many decades, a full picture of overall hardening behavior due to co-existed strengthening particles does not yet exist. Building on this background, the purpose of this thesis is to study how individual strengthening mechanisms interact with each other and combine together to provide an overall strengthening of the metal alloys. Below in this chapter, a brief introduction to physics of dislocations and individual strengthening mechanism is given first. The theories, methods and set-ups used in the studies of multiple strengthening mechanisms is summarized, together with an overview of the current literatures on this

topic.

1.1 Dislocation

The properties of dislocations, their creation, motion, multiplications and the interactions with each other and crystal defects lie at the center of the plastic deformation in crystalline materials. The theory of dislocations is well presented in depth in several reference works [42, 43]. The presentation here focuses on the necessary concepts used in following chapters.

The dislocation is best conceived of as the line of termination of discontinuity in slip within materials, carrying energy per unit length. The energy of a dislocation can be divided into the linear elastic part E_{el} of the strain energy outside the dislocation core and the core energy E_{core}, that is $E_{\text{total}} = E_{\text{el}} + E_{\text{core}}$. The elastic energy per unit length is calculated in a region bounded by cylinders with inner radius r_0 and outer radius R. In the case of isotropic elasticity, the elastic energy per unit length of a dislocation where the Burgers vector forms an angle θ with the line direction can be expressed as [42, 43]

$$E_{\text{el}} = \frac{\mu b^2(1 - \nu\cos^2\theta)}{4\pi(1-\nu)} \ln\frac{R}{r_0} \tag{1.1}$$

where μ is the shear modulus, b is the magnitude of the Burgers vector and ν is the Poisson's ratio. Due to the complexity of obtaining exact solution for the energy calculation shown in equation ((1.1)), energy calculations in dislocation theory are often made using the so-called line tension approximation. In the line tension approximation, the dislocation is considered to be a smooth flexible string with a line tension Γ, defined by the change in configuration energy δW due to a change in the dislocation line length δL [42]

$$\Gamma = \lim_{\delta L \to 0} \frac{\delta W}{\delta L} \tag{1.2}$$

The line tension concept ignores long-range dislocation segment interactions of the explicit dislocation configuration, and lumps them together with the line energy into a local energy per unit line length. Equilibrium dislocation configurations under a given applied field can then be easily obtained. Analysis of energies of specific dislocation configurations shows that, at the continuum level, the line tension is generally $\Gamma \sim \mu b^2/2$ where the numerical factor of $1/2$ represents a combination of factors. In an anisotropic framework, the line tension depends on the character angle θ of the line as $\Gamma = E_{\rm el}(\theta) + \partial^2 E_{\rm el}(\theta)/\partial\theta^2$ which predicts an anisotropy factor of $(1-2\nu) + 3\nu\cos^2\theta$, and hence a difference between screw and edge dislocations of 4 for $\nu = 1/3$

As discussed above, the understanding of strengthening mechanism due to insertion of second-phase obstacles relates to the interaction of dislocation with various types of obstacles. Using the concept of line tension, the treatment of dislocation-obstacle interaction can be simplified reasonably well. The simplest case shown in figure 1.1(a) is the dislocation interacting with series of equally spaced, localized obstacles. This simple geometry will be used in the later calculations of the exact line tension at atomistic scale. In this situation, the resistance to dislocation motion due to obstacles is represented by a force $F_{\rm ob}$ acting on the pinning points along the dislocation line. Under an applied shear stress τ the initial straight dislocation will bow out between two pinning obstacles and exert force acting to the obstacles. The radius of curvature R is then related to τ and the line tension Γ by [43]

$$\tau b = \frac{\Gamma}{R} \tag{1.3}$$

The equilibrium of the line tension and the obstacle force at the pinning point lead to the following relationship for the angle ϕ shown in figure 1.1,

$$F_{\rm ob} = 2\Gamma\cos\frac{\phi}{2} \tag{1.4}$$

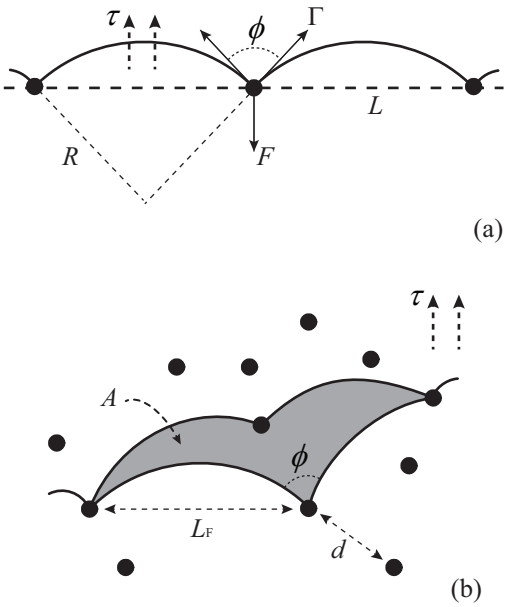

Figure 1.1: Schematic of a dislocation with line tension Γ advancing in a field of weak point-like obstacles. (a). The obstacles are equally spaced linearly array of obstacles; (b). The obstacles are randomly distributed on the slip plane

The dislocation will break away from obstacles separated by a distance L if the maximum resisting force $F_{\mathrm{ob}}^{\mathrm{c}}$ at the obstacle is reached by the driving force τbL which is acting on the entire dislocation line between the obstacles. With equation ((1.4)) the obstacle strength can be characterized by a critical angle ϕ^{c} given by the Critical Resolved Shear Stress (CRSS) τ^{c} for dislocation to break through

$$\phi^{\mathrm{c}} = \cos^{-1}\left(\frac{\tau^{\mathrm{c}} bL}{2\Gamma}\right) \tag{1.5}$$

The CRSS for a regular square array of localized obstacles can thus be expressed as

$$\tau^{\mathrm{c}} = \frac{2\Gamma}{Lb}\cos\frac{\phi^{\mathrm{c}}}{2} \tag{1.6}$$

Furthermore, interaction of dislocation with a statistical field of randomly distributed obstacles has also been studied using a line tension concept. In this framework, the analytical Friedel model [31] well describes the strengthening due to a dilute obstacle

volume fraction c which can be then idealized as weak pinning points, as shown in figure 1.1(b). The basic assumption of the Friedel model is that under the applied shear stress τ, the number of obstacles on the dislocation line is constant. Under this assumption, the distance between obstacles on the dislocation line can be calculated as

$$L_{\mathrm{F}} = d\cos\left(\frac{\phi^{\mathrm{c}}}{2}\right)^{-1/2} \tag{1.7}$$

where d is the average spacing of obstacles. equation ((1.7)) then leads to the CRSS

$$\tau^{\mathrm{c}} = \frac{2\Gamma}{b}\cos\left(\frac{\phi^{\mathrm{c}}}{2}\right)^{3/2} \tag{1.8}$$

The idealization used in Friedel model will permit the development of some other generally useful statistical concepts and these details are present in Ref. [4, 31].

In the above description, dislocations were treated in an ideal elastic continuum. At atomistic scale, a dislocation lattice introduces a disregistry of atomic coordination across the slip plane and details such as dislocation core structure become essential. Specific features of dislocations in FCC metals are briefly introduced here. In FCC metals with lattice constant a_0 the shortest lattice vectors, and therefore the most likely Burgers vectors, are of the type $b = \frac{a_0}{2}\langle 110\rangle$. These perfect dislocations are however usually dissociated into two Shockley partial dislocations according to the reaction [42, 43],

$$\frac{a_0}{2}\langle 110\rangle \rightarrow \frac{a_0}{6}\langle 211\rangle + SF + \frac{a_0}{6}\langle 12\bar{1}\rangle \tag{1.9}$$

including an intrinsic stacking fault (SF) between two partial dislocations, which defines a splitting distance d_{sf} in between the two Shockley partials. Dislocations in FCC metals are best described by the Thompson notation. The Thompson tetrahedron is shown in figure 1.2. Throughout this work, the Thompson tetrahedron is made to describe the dislocation-dislocation interactions in FCC crystals. The dis-

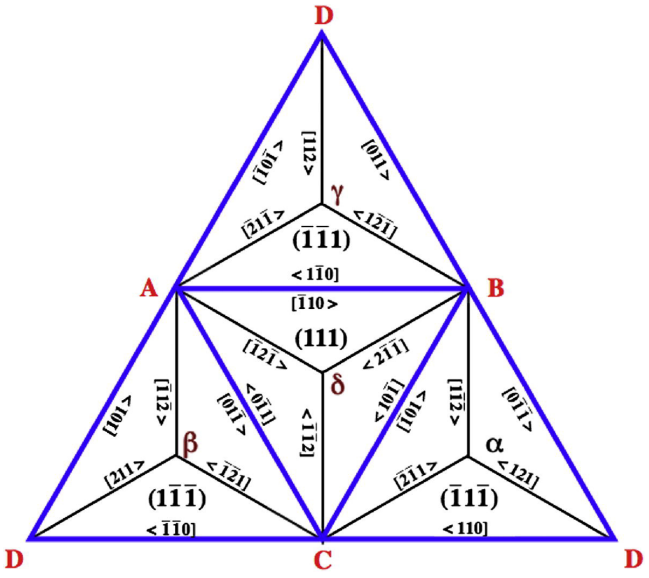

Figure 1.2: Opened up Thompson tetrahedron presenting both the Thompson notation and the usual crystallographic notation. The notation $\langle\bar{1}\bar{1}0]$ is used instead of the usual notation $[\bar{1}\bar{1}0]$ to indicate the sense of the direction. For example, the perfect dislocation with Burgers vector $\frac{a_0}{2}[\bar{1}\bar{1}0]$ on the $(1\bar{1}\bar{1})$ plane is denoted in the Thompson notation by CD and it dissociates into $C\beta + \beta D$ on the same plane

location junction is formed by the dislocation on different slip planes interact with each other such that a minimum energy configuration is obtained. In FCC crystals, these interactions occur between 12 slip systems that involve $\{111\}$ slip plane and associated Burgers vectors [41], all of which can be described by the Thompson tetrahedron. For example, a Lomer junction is explained here using the Thompson notation. The perfect dislocation with Burgers vector $CA = \frac{a_0}{2}[0\bar{1}1]$ on the (111) plane interacts with the dislocation with Burgers vector $DC = \frac{a_0}{2}[110]$ on $(\bar{1}1\bar{1})$ plane to form a Lomer junction with Burgers vector $DA = \frac{a_0}{2}[101]$ and line orientation CB $= [\bar{1}01]$. Note that the cores of the dislocations in FCC crystals are dissociated into partial dislocations separated by a stacking fault, such intersections can lead to more complex dislocation junction structures such as the Lomer-Cottrell (LC) junction [42] which can be visualized by atomistic simulations [95] and will be discussed in more details in following chapters.

1.2 Strengthening mechanism in metal alloys

A dislocation in crystalline lattice introduces a disregistry of atomic coordination across the slip plane, which leads to a dislocation core energy and a resistance against the dislocation motion. Due to its intrinsic scale, such lattice resistance however can not be well described by elastic dislocation theory. The Peierls-Nabarro model [42, 72, 83] instead was developed to address the atomistic structure and regularize the dislocation core and the Peierls stress τ_{P} is then used to quantify the stress needed to move the dislocation in the presence of the intrinsic atomistic-scale misfit.

Beside the lattice resistance, the strengthening due to addition of second-phase obstacles can usually classified into two major categories: strong pinning, such as forest dislocations, voids, precipitates and so on, in which the single obstacle is sufficient to pin the dislocation at the obstacle position; and weak pinning like solutes in which the dislocation is pinned by a favorable collective configuration of solute atoms in a region of the materials. The point-pinning model discussed in section 1.1 shows that the strength due to dislocation-obstacle interaction would be a function of dislocation line energy, obstacle density, geometry and spatial distribution of obstacles. Numerical simulations based on line tension theory were then carried out to compute critical zero-temperature flow stresses under different strengthening obstacle properties. The earliest attempt was carried out by Foreman and Makin [29, 30], in which they studied the glide of the dislocation in random arrays of point-obstacles of various resistance. In the limit of weak point-obstacles, their simulations showed good agreement with Friedel's model. Similar simulations [2, 3, 34, 36, 45, 113] were also performed to address the influence of the obstacle statistical distribution, finite-size simulation cell etc. Except the recent calculation done by Zhu et al. [113], these simulations and theories usually focused on point-pinning obstacles model, which ignore any influence of the interaction length between the dislocation and obstacles. Therefore they are suitable to describe the hardening behavior due to small size precipitates or dilute solute solutions.

The failure of point pinning model for solid-solution with relative high concentration $c \sim 5\%$ inspires alternative approach for the solute strengthening which starts by considering the interaction of the eigenstrain created by the solutes and the stress field of the dislocations. Extensive classical studies [1, 27, 33, 50, 51, 54, 68] have shown that the strengthening due to solid-solution is a function of solute concentration, the magnitude and gradient of the solute/dislocation interaction energy, the dislocation line energy, the shear modulus and the Burgers vector of the matrix metals. Furthermore, It has been shown in theoretical analysis [59] and numerical simulations [80, 82, 87, 88, 92] that it is only the random fluctuations in solute concentration around the dislocation that can provide strengthening and segments along an initially straight dislocation can be attracted to energetically favorable fluctuations, and bow out towards them, at the cost of dislocation line energy, as discussed in the pioneering work of Labusch [54]. Based on Labusch statistics, recent proposed analytical model is then able to predict an accurate CRSS due to solution strengthening [58, 59].

Point-pinning model in certain extent is not suitable either when considering the forests strengthening because of the size of the junction structures. In the frame work of forest hardening, dislocation segments on the glide plane are pinned due to the intersection with forest dislocations on the other glide planes. The intersection between mobile dislocations and forest dislocations results in the formation of junction segments. Depending on types of dislocation intersecting and stress state, some of the junction segment serve as sessile locks impeding the dislocation motion. From the dislocation line energy, the formation and strength can be very well investigated for different type of junctions existed in FCC metals [24, 86, 97, 102, 107]. It has been shown that the junction resistance strongly depends on the geometric disposition of the participating dislocations and can be very well predicted by dislocation line energy approach. The studies of individual junction strengthening then provide key parameters like junction size and hardening coefficient that can be used in mod-

els that predict the work hardening due to collective effect of dislocation network at mesoscale [62]. For the latter, recent developed dislocation dynamics (DD) simulations are proven to be a very powerful tool to explore the evolution of dislocation network during deformation and related work hardening behavior [14, 15, 63, 66, 89].

Theories and simulations mentioned above all describe the dislocation-obstacle interaction at macroscopic scale; approximations therefore have to be made since the direct interaction between dislocation and obstacles is essentially controlled by atomic mechanism, especially when the dislocation core structure is involved in the interaction process. Many computer simulations at atomistic and quantum scale have been developed to analyze the dislocation-obstacle interaction and make more accurate prediction for associated strengthening behavior when single type of obstacle presents. The solid solution strengthening behavior has been investigated through Molecular Dynamics (MD) studies of a single dislocation (either edge or screw character) moving through a field of randomly placed substitutional solutes atoms [80, 82, 87, 88, 92]. Simulations done by Rodary [92], Patinet and Proville [82, 87, 88] for hardening behavior in Al/Mg and Ni/Al alloys all showed that the significant strengthening was due to the short-range interaction of dislocation with particular solutes configurations. MD simulations done by Olmsted et al. [80] analyzed the energy landscape for the motion of a straight dislocation trapped in a local energy minimum generated by the solutes and then well predicted the applied stresses required for dislocation escape from energy minima at different temperatures. More recent density functional theory calculation [57, 59] accurately capture the solute/dislocation interaction energies at quantum scale in and around dislocation core and a parameter-free model is then developed to predict accurately the flow stresses for aluminum alloys based on the analysis concept developed by Labusch [54]. Similar approach was also introduced to describe the strengthening behavior for Mg/Al alloys [58]. On the other hand, forest dislocations strengthening, is also very well investigated by mesoscopic and atomistic simulations [14, 62, 63, 77, 95, 100, 107, 111].

In these simulations, the formation and destruction of dislocation junctions were analyzed in great detail, in which the junction structure is similar as the experimental observations [95, 100]. The hardening behavior due to different junction type can be described in simulations and it was found by far that the collinear lock is the strongest dislocation-dislocation interaction [62]. The predicted strengths from the simulations were then used to validate various models [24, 86, 97, 102, 107] based on the line tension approximations, in which good agreement was reached. Atomistic simulations for hardening behavior due to dislocation interacting precipitates, voids, dislocations loops and stacking fault tetrahedron were also carried out and comprehensively reviewed by Bacon et al. and references therein [9]. In these simulations, the friction stress due to lattice resistance is usually very small and therefore the influence of lattice resistance on the dislocation junction can be safely ignored.

1.3 Hardening due to multiple types of strengthening mechanism

As mentioned earlier, in most engineering alloys the flow stress is controlled by several different obstacle types such as forest dislocations plus solutes and/or precipitates operating simultaneously, and therefore a clear understanding of how different strengthening mechanisms operate together to generate a macroscopically measured flow stress is required.

At zero temperature, knowing the zero-temperature flow stresses $\hat{\tau}_1$ and $\hat{\tau}_2$ for two different strengthening mechanisms acting separately, a general superposition rule [38, 50, 53]

$$\hat{\tau}^k = \hat{\tau}_1^k + \hat{\tau}_2^k \tag{1.10}$$

for the total flow stress $\hat{\tau}$ has been proposed to account for the combination of two different strengthening mechanisms. The exponent $1 \leq k \leq 2$ depends on details of

obstacle densities and relative strengths. Based on the Friedel's model, Kocks and co-workers [50] first proposed that the critical spacing of different obstacles is independent and hence suggested $k = 1$. The linear superposition $k = 1$ is often assumed for interpreting operating mechanisms from strain-rate-sensitivity measurements via the so-called Haasen plot of inverse activation volume vs stress [32, 69, 70, 71]. Linear superposition also emerges immediately if the solute strengthening is modeled as a continuous friction stress, where the stress acting on the other mechanism is simply $\hat{\tau} - \hat{\tau}_1$. Koppenaal and Kuhlmann-Wilsdorf proposed the geometric mean model of $k = 2$ [53] which was then supported by statistical calculations and simulations [30, 35, 47, 52]. A formulation by Labusch [54, 55] suggested $k = 1.5$ by considering the extended range of obstacle/dislocation interactions but applying particularly to multiple solute types. Brown and Ham [13] summarized the numerical works and concluded that linear superposition is a poor approximation, except when a few "strong" obstacles are dispersed in many "weak" obstacles, and that the geometric mean has more general validity. In some special cases, a "mixture rule" $\hat{\tau}^k = c_1^n \hat{\tau}_1^k + c_2^n \hat{\tau}_2^k$ was used, where c_1 and c_2 are the obstacles concentrations [13, 50, 64]. Zhu et al.'s more recent simulations validated this mixture rule and gave $n = k/2$ with k varying from 1 to 2 still. More recently, Hiratani and Bulatov [38] used an approach based on configurational entropy to show that the geometric mean $k = 2$ is a special case prevailing when the pinning strength of obstacles is weak and almost the same.

Due to the difficulty on precise measurement of separate strengthening contribution from the overall strengthening, direct experimental studies of the mixture rule by experiments are very limited and showed various values of the exponents k [16, 25, 40, 56, 74, 75, 91]. For example, experimental work done by Lagerpusch et al. [56] suggested $k = 1.8$ for a copper-gold solid solution strengthened by silica obstacles, whereas Reppich [91] instead suggested a value $k \sim 1.0$ to 1.5 from the experimental results of the Nickel Superalloy hardened by Ni_3Al and Ti, which

was close to the value $k = 1.2$ proposed by Neite et al. [73]. The ambiguity in k from experiments gave poor verification of the proposed mixture of rule. Alternatively, numerical approach is then widely introduced for this topic since individual strengthening obstacle properties can be very well pre-defined in computational simulations. Building on the previous point-pinning line tension model by which the dislocation motion through fields of single type of point obstacles was studied, numerical simulations of dislocation glide through two different strengthening obstacles operating simultaneously were conducted. However, for different combination of obstacles strengthes and densities, the obtained k from simulations still varies in which $k = 1, 1.5, 1.8, 2$ were reported in literatures [30, 35, 56, 112]. More recently, 3D DD techniques were also used to perform the simulations of hardening behavior when two strengthening mechanisms are present. The DD simulations done by Monnet and Devincre [66] approximated the solid-solution strengthening by a homogeneous alloy friction and they found that the forest dislocation strength reduced with alloy friction increasing, resulting in the failure of linear additivity used in friction limit. Similar simulations were conducted by Queyreau et al. for Orowan strengthening and forest hardening superposition [89], where the numerical results supported the reliability of geometric mean model of $k = 2$.

Furthermore, *flow stress* is, however, also dependent on both temperature and strain rate, reflecting the fact that dislocations can overcome obstacles through thermally-activated processes [17, 20, 50], which complicates more the combination of multiple types of strengthening mechanism. Via thermal activation, dislocations can surpass obstacles so that the flow stress τ is a function of strain rate $\dot{\varepsilon}$ and temperature T. Previous studies [4, 17, 50] have revealed that the macroscopic strain rate can be related to the activation enthalpy ΔG [50] via an Arrhenius-type rate equation. ΔG, which is essentially the energy barrier (neglecting entropic contributions) required for thermal activation of dislocation across an obstacle, is stress-dependent at a prescribed $\dot{\varepsilon}$ and T. In this general frame, the thermally-activated motion of

the dislocation and associated macroscopic strain rate can be characterized by some function involving ΔG, τ and T. The strain rate sensitivity (SRS), $m = \partial \ln\dot{\varepsilon}/\partial \ln\tau$, and the apparent activation area, $\Delta a = -\frac{1}{b}\frac{\partial \Delta G}{\partial \tau}$, can then be compared with experiments. The thermally-activated behavior of dislocations through a field consisting of a single type of obstacle has been studied numerically for years [2, 6, 44, 67, 109], where it is shown that factors such as the obstacle strength, density and spatial distribution have strong influences on the flow behavior.

Owing to the complexity of possible mechanisms, the simultaneous operation of and interactions between, different strengthening mechanisms operating together at finite temperature is very complicated. The first question regarding the superposition of flow stress at finite temperature is how the individual strengths should be measured. As pointed out by Kocks et. al [49, 50] and Diak [23], the flow stresses for different mechanisms must be defined at the same $\dot{\varepsilon}$ and T. Building on this foundation, a natural and simple idea is to extend the linear additivity at zero temperature to finite temperature [50], i.e. $\tau(\dot{\varepsilon}, T) = \tau_1(\dot{\varepsilon}, T) + \tau_2(\dot{\varepsilon}, T)$. As a result, linear additivity of the inverse activation area emerges. However, linear additivity cannot predict the reduced slope of the Haasen plot found in experiments of solute-strengthened alloys [21, 22, 23, 32, 69]. The general superposition rule can be extended also, i.e. $\tau^k(\dot{\varepsilon}, T) = \tau_1^k(\dot{\varepsilon}, T) + \tau_2^k(\dot{\varepsilon}, T)$, but without fundamental justification [23, 48]. Schoeck [98] theoretically studied the thermally-activated motion of a dislocation line in a field containing a low density of obstacles with high activation energy and a high density of obstacles having low activation energy. He concluded that the linear additivity at finite temperature did not follow from linear additivity at $T = 0$. Aresenault and Cadman [5] simulated the thermal motion of a dislocation across a random array of point obstacles having different strengths and zero-stress activation energies at finite temperature. Their simulations gave an overall flow stress $\tau(\dot{\varepsilon}, T)$ lying between $\tau_1(\dot{\varepsilon}, T) + \tau_2(\dot{\varepsilon}, T)$ and $(\tau_1^2(\dot{\varepsilon}, T) + \tau_2^2(\dot{\varepsilon}, T))^{1/2}$. In these studies, the relationship between the overall activation energy and the properties

of individual obstacle type and the flow stress was not made clear. More recently, Picu et al. [109] analyzed the SRS for a single type of point obstacle via simulations and developed a model to account for the variation of the SRS parameter m. The model was consistent with simulations at low stress level but deviated at high stresses. They argued that the different regimes for m are associated with different mechanism of dislocation motion (smooth un-zipping mode at low stresses and jerky mode at high stresses). Subsequent simulations with multiple point obstacles type explored similar variation of m with flow stress [85], showing that the SRS was very sensitive to the presence of obstacles with large strength and high activation energy. Insertion of even a small density of strong obstacles gave SRS behavior comparable to that of the strong obstacles operating alone. Picu et al. thus suggested that linear additivity of flow stress at finite temperature would be valid only when the flow stresses due to individual strengthening were measured at the same SRS parameter [84, 85].

1.4 Outline

The above brief literature review shows that the strengthening associated with simultaneous operation of multiple strengthening mechanisms remains far less clear. For the empirical rule of mixture equation used at zero temperature, the guideline of choosing the exponent k for different obstacles properties is still an open question. Moreover, the thermally-activated flow in the presence of multiple strengthening mechanisms remains poorly understood, for which the explicit form of the overall flow stress versus strain rate and temperature requires further development. Complicating the rule of mixture at finite temperature is that most numerical simulations are in a regime where the zero-temperature flow stresses themselves are not additive, making it particularly difficult to extract the interaction effects at finite temperature [5, 85].

From numerical simulation perspective, most of existing simulations have focused on point-pinning obstacles model, which neglects any influence of the interaction length between the dislocation and obstacles. However, the point-pinning assumption has to be treated with care since previous simulations have shown that, at zero temperature, the interaction width of the obstacles affects the way in which the dislocation samples the field of obstacles during glide, and thus affects the shear resistance of obstacles [99, 112, 113]. Moreover, we have shown in section 1.2 that the clear understanding of various strengthening mechanism relies greatly on the atomistic details of dislocation-dislocation interaction and/or dislocation-solute interaction. However, to our knowledge, the forest hardening due to dislocation junction combined with the solutes strengthening has never been investigated at atomistic scale.

In summary, the purpose of this work is therefore to understand the coupled dislocation/dislocation and solute strengthening mechanisms in metal alloys. The focus is thereby to provide quantitative information on the overall strength when solid-solution strengthening and forests strengthening operate simultaneously, using numerical techniques both at continuum scale and atomistic scale. The remainder of this thesis is organized as follows. Chapter 2 is to explore the scaling of dislocation strengthening by multiple obstacle types, where we examine the strengthening of two mechanisms operating in tandem within the classical framework of the line-tension model with point obstacles. Chapter 3 is to develop an atomistic model for line tension calculation of dislocation in metals, which will provide a reliable data set for further studies in the strengthening mechanisms at different scales. Chapter 4 is to explore the solute/dislocation-junction interactions in metal alloys at atomistic scale, providing detailed information about the effect of solute atoms on the formation, geometry and strength of dislocation junctions. Based on the clear understanding of the basic scaling law of strengthening by multiple strengthening particles, chapter 5 is to study, both numerically and theoretically, the rate- and temperature-dependent

plastic flow in a material containing two types of thermally-activatable obstacles to dislocation motion in a regime of relative obstacle densities for which the zero-temperature stress is additive. The effect of a finite-size interaction width in between dislocation-obstacle interaction is also investigated extensively in chapter 5. All the results of this work are then summarized in chapter 6, in which further development for this topic is also proposed.

Chapter 2

Scaling of Dislocation Strengthening by Multiple Obstacle Types

2.1 Introduction

In the considerations of dislocation in linear elastic continua at zero temperature, the simulations based on the line tension model with point obstacles have been proven to be a valid statistical algorithm to study the dislocation motion in a field with single type of randomly distributed obstacles. However as reviewed in chapter 1, when the similar approach was used for the glide of dislocation across the field having two different types of strengthening obstacles, various results were reported, making it hard to compare the numerical finding with the zero-temperature flow stress predictions made with different rules of mixtures.

$$\hat{\tau}^k = \hat{\tau}_1^k + \hat{\tau}_2^k \tag{2.1}$$

In order to explore the basic scaling of dislocation strengthening due to two differ-

ent obstacles operating simultaneously, we examine in this chapter the strengthening of two mechanisms operating in tandem within the classical framework of the line-tension model with point obstacles. In contrast to most similar studies, however, we focus on the regime wherein one type of obstacle is very weak but of very high density, thus approaching the friction limit. When combined with a second set of obstacles, this limit requires a very large number of obstacles and is thus computationally demanding, which is why this limit was not investigated previously. Our results show a transition from additive ($k = 1$) to geometric mean ($k = 2$), primarily as a function of the density of the second obstacle. The additive regime is obtained when the obstacle spacings differ by more than a factor of ~ 67, even when the strength $\hat{\tau}_2$ is large compared to $\hat{\tau}_1$. These results put much of the prior metallurgical wisdom on a firm foundation, clarifying the range of validity of the friction ($k = 1$) and geometric mean ($k = 2$) limits that have been applied to interpret many experiments.

2.2 Simulation methods

We simulate glide of a single dislocation along its glide plane, with two different types of obstacles on the glide plane impeding dislocation motion. The dislocation is represented using an isotropic line tension model, and the obstacles act as points that pin the dislocation. As shown in figure 2.1, the dislocation line is defined by a sequence of consecutive segments pinned between unbroken obstacles. In between the pinning points, the dislocation bows out into a section of circular arc with radius of curvature predicted by equation (1.3), $R = \frac{\Gamma}{\tau b}$, where Γ is the dislocation line tension, τ is the applied shear stress, and b is the magnitude of the Burgers vector. At each pinning obstacle, the two adjacent pinned dislocation segments define an angle ϕ and exert a force on the obstacle. Using equation (1.5), the obstacles are characterized by (1) the breaking angle, ϕ_i^c, at which point the force on obstacle type i reaches

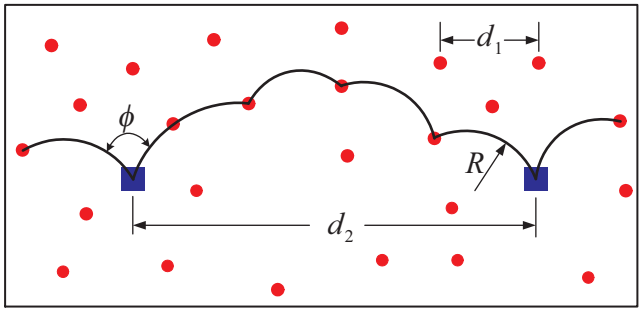

Figure 2.1: Schematic of a dislocation line on a slip plane composed of segments pinned by two types of obstacles. Red circles: randomly positioned type 1 obstacles; blue squares: linear periodic array of type 2 obstacles.

the maximum resisting force and the dislocation overcomes the obstacle; and (2) the average space d_i between obstacles of type i. Two types of obstacles, denoted by 1 and 2 with corresponding $\phi_1^c > \phi_2^c$ and $d_1 \ll d_2$, are placed in the glide plane. Type 1 obstacles are randomly distributed throughout the plane. Because d_2/d_1 is large, it is not computationally feasible to introduce type 2 obstacles at random, because accurate results for a random distribution require at least 200 obstacles along the length of the dislocation line [78]. Instead, a linear periodic array of type 2 obstacles is inserted, as shown in Figure 2.2. Periodic boundary conditions are applied on the lateral boundaries. The simulation box is square with a size L determined by the number of type 1 particles, N_1, and their average spacing d_1 as $L = d_1\sqrt{N_1}$. In these line tension simulations, the line tension is taken as $\Gamma = \mu b^2/2$, where b is the magnitude of the Burger's vector and μ is the shear modulus. All lengths are normalized by d_1 as $R = R/d_1$. All stresses can then be normalized as $\tau^* = \tau d_1/\mu b$ such that $\tau^* = 1$ for a stress that bows the dislocation into a semicircle with a diameter of d_1.

The algorithm developed by Nogaret and Rodney [78] is employed to simulate dislocation motion through the field of obstacles. As illustrated in figure 2.2, a segment pinned by obstacle n_S and n_F can evolve in three distinct ways to which correspond three critical stresses that can be computed analytically. The first possibility, figure

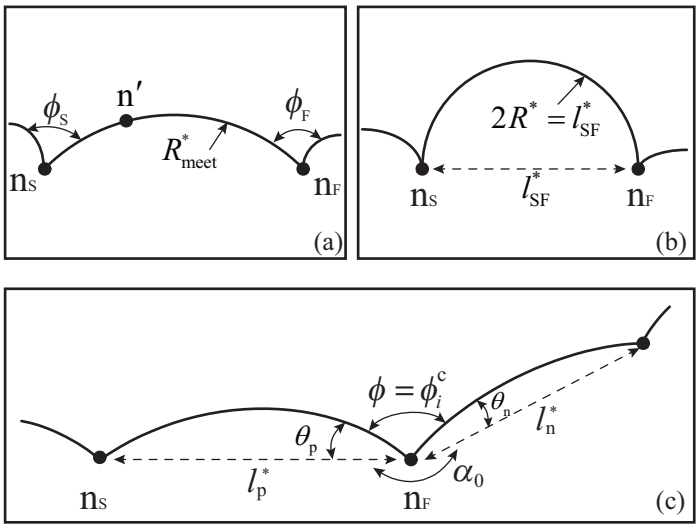

Figure 2.2: Schematic of the three possible evolution mechanisms for a dislocation segment. (a). meet a new obstacle n'; (b). become unstable; (c). break one of the obstacles that pins the segment ($n_{\rm F}$ in the present sketch).

2.2(a), is that the segment, when bowing out, meets a new obstacle n', in which case the segment is cut in two to incorporate the n' on the dislocation. The potential obstacle is found by searching the obstacles that are in the half-circle of diameter equal to $l^*_{\rm SF}$, the distance between $n_{\rm S}$ and $n_{\rm F}$. The first obstacle that the dislocation will meet corresponds to the maximum radius of curvature $R^*_{\rm meet}$ and the stress is $\tau^*_{\rm meet} = \frac{1}{2R^*_{\rm meet}}$. The second possibility in figure 2.2(b) is that the segment becomes unstable if its shape reaches a half-circle. Its bow-out radius is then $R^* = l^*_{\rm SF}/2$ and the corresponding stress is the segment Orowan stress: $\tau^*_{\rm Orowan} = 1/l^*_{\rm SF}$. The third possible event is one of the obstacles (either $n_{\rm S}$ or $n_{\rm F}$) that currently pin the segment is broken of which the angle reaches the critical breaking angle $\phi^{\rm c}_i$ ($i = 1$ or 2). For example in figure 2.2(c), the angle ϕ on $n_{\rm F}$ becomes smaller than $\phi^{\rm c}_i$ and the corresponding obstacle is overcome. Both segments pinned at this obstacle are removed and replaced by a single segment. With the notation in figure 2.2(c), where $\vec{\rm l}^*_{\rm p}$ and $\vec{\rm l}^*_{\rm n}$ are the vectors joining the broken obstacle to its two neighbors on the

dislocation line and $\theta_{\rm p}$ and $\theta_{\rm n}$ the corresponding angles, the obstacle breaks if

$$\phi = \phi_i^{\rm c} = 2\pi - \alpha_0 - \theta_{\rm p} - \theta_{\rm n} \tag{2.2}$$

where α_0, $\theta_{\rm p}$ and $\theta_{\rm n}$ are expressed as

$$\cos(\alpha_0) = \frac{\vec{\mathbf{l}}_{\rm p}^* \cdot \vec{\mathbf{l}}_{\rm n}^*}{l_{\rm p}^* l_{\rm n}^*}, \quad \sin(\theta_{\rm p}) = \tau_{\rm break}^* l_{\rm p}^*, \quad \sin(\theta_{\rm n}) = \tau_{\rm break}^* l_{\rm n}^* \tag{2.3}$$

Substituting equation (2.3) into equation (2.2), after simple algebra, gives

$$\tau_{\rm break}^* = \frac{\left|\sin\left(\alpha_0 + {\phi_i}^{\rm c}\right)\right|}{\sqrt{2\cos\left(\alpha_0 + {\phi_i}^{\rm c}\right) l_{\rm p}^* l_{\rm n}^* + l_{\rm p}^{*2} + l_{\rm n}^{*2}}} \tag{2.4}$$

In this third case, a search is made for non-broken obstacles in the area below the new segment, in which case the segment is subdivided in order to incorporate these obstacles on the dislocation.

Using the preceding computational model, arrays of obstacles with different average spacings, d_1 and d_2, and breaking angles, $\phi_1^{\rm c}$ and $\phi_2^{\rm c}$, are simulated. In order to make sure there is no finite-size effect introduced during calculation, the total number of obstacles is always larger than 40000 [78]. The code was first validated by investigating the zero-temperature flow stress for a single weak obstacle type randomly distributed in the plane. For two different average spaces, d_1, and a range of critical angles $145^\circ < \phi_1^{\rm c} < 180^\circ$, our simulations are in essentially perfect agreement with Friedel's law,

$$\hat{\tau}_1 = 0.9\tau_{\rm F} = 0.9\frac{\mu b}{d_1}\cos^{\frac{3}{2}}\left(\frac{\phi_1^{\rm c}}{2}\right) \tag{2.5}$$

For strong obstacles positioned in a periodic linear array, as shown in figure 2.2, the zero-temperature flow stress is simply

$$\hat{\tau}_2 = \frac{\mu b}{d_2}\cos\left(\frac{\phi_2^{\rm c}}{2}\right) \tag{2.6}$$

Normalized strengths and lengths are used throughout the remainder of this article, so that

$$\hat{\tau}_1^* = \frac{\hat{\tau}_1 d_1}{\mu b} = 0.9\cos^{\frac{3}{2}}\left(\frac{\phi_1^c}{2}\right), \quad \hat{\tau}_2^* = \frac{\hat{\tau}_2 d_1}{\mu b} = \frac{1}{d_2^*}\cos\left(\frac{\phi_2^c}{2}\right), \quad \hat{\tau}_t^* = \frac{\hat{\tau}_t d_1}{\mu b} \tag{2.7}$$

where $\hat{\tau}_t$ is the overall strength due to two strengthening obstacles and $d_2^* = d_2/d_1$ is the normalized average space for type 2 obstacles, which characterizes the relative density difference for two types of obstacles. The length d_1 is the basic length unit in this theoretical framework, and hence, its absolute value is not relevant for our study. In the following simulations, we choose two different values of d_1 so that we can examine two different choices of ϕ_1^c while maintaining a constant $\hat{\tau}_1^*$ so as to test the dependence on the breaking angle. No physical significance should be attached to the values of d_1 used here though.

2.3 Results

In order to discuss the case of strengthening by solute atoms or forest dislocations operating in tandem with solid solution strengthening, we set a very small average spacing and very large critical angle for type 1 to represent the solid solution matrix. In order to mimic the hardening behavior due to solid-solution in Al-1%Mg alloy, we set $d_1 = 0.2$ nm with $\phi_1^c = 179.5°$ or $d_1 = 0.6$ nm with $\phi_1^c = 178.9°$, both of which combine to give a solute strength of $\hat{\tau}_1 \approx 10$ MPa. For type 2 obstacles, we incorporate the definition in reference [30], setting the average spacing varying from 2.66 to 120 nm, so that d_2^* ranges from 13 to 200. The critical angle for type 2 is in the range $45° < \phi_2^c < 176°$, so that the two obstacles together span the range from the *weak-strong* limit $\phi_2^c \sim 45°$ to $60°$, *weak-medium* limit $\phi_2^c \sim 145°$ to $160°$, to the *weak-weak* limit $\phi_2^c = 176°$ to $60°$, as defined in reference [30].

The simulation results for the normalized total strength as a function of the normalized strength of type 2 obstacles are shown in figure 2.3 in the weak-medium

and weak-weak regimes. To clearly show the relative strength of the two mechanisms (e.g., two different obstacle types), the strengths in figures 2.3 and 2.4 are all scaled by the normalized strength of type 1 obstacles $\hat{\tau}_1^*$, as $\hat{\tau}_t^*/\hat{\tau}_1^*$ and $\hat{\tau}_2^*/\hat{\tau}_1^*$ shown in figure 2.3. The simulation results for the scaled total strength $\hat{\tau}_t^*/\hat{\tau}_1^*$ as functions of the normalized average spacing of type 2 obstacles d_2 are shown in figure 2.4 using logarithmic scales. In both figures, the predictions of the linear rule and geometric mean rule for the total strength are also shown. The total strengths in all simulations are within the domain between the additive and geometric mean rules, which confirms that the empirical superposition shown in equation (2.1) with $1 \leq k \leq 2$ is adequate to describe mixtures of different strengthening obstacles. Figure 2.3 clearly shows the transition from the linear to geometric rule with increasing type 2 strength. In all weak-medium cases, the linear rule is applicable at lower strengths. The transition to the geometric rule with increasing $\hat{\tau}_2^*$ is weakly dependent on the obstacle critical angle. It is only in the weak-weak limit that the geometric rule is attained over most (but not all, as subsequently discussed) values of obstacle strengths. Interpretation of the strengthening in terms of $\hat{\tau}_2^*$ and ϕ_2^c is limited, however, and more insight is gained by examining the role of obstacle spacing, as shown in figure 2.4.

Figures 2.4(a) and (b) clearly show that the linear rule applies when $d_2^* > 67$ for both the weak-medium and weak-strong limits. For the weak-weak limit, $k = 1$ is valid only at very large $d_2^* = 200$. These results confirm Kock's argument that when the density of obstacles differs greatly, the two obstacles will act independently and, hence, the linear rule will apply. Moreover, our results show that the linear rule always holds for very large density differences. This result differs from the results by Hanson and Morris,[35] because their values of d_2^* were only in the range of about 1 to 10. It also differs from the results of Hiratani and Bulatov,[39] whose analysis indicates applicability of the geometric mean rule when ϕ_2^c is very close to ϕ_1^c (weak-weak limit here) and is supported by their dislocation dynamics simulation data with $\phi_1^c = 168.17°$ and $\phi_2^c = 166.80°$. The difference may also be due to their study of a

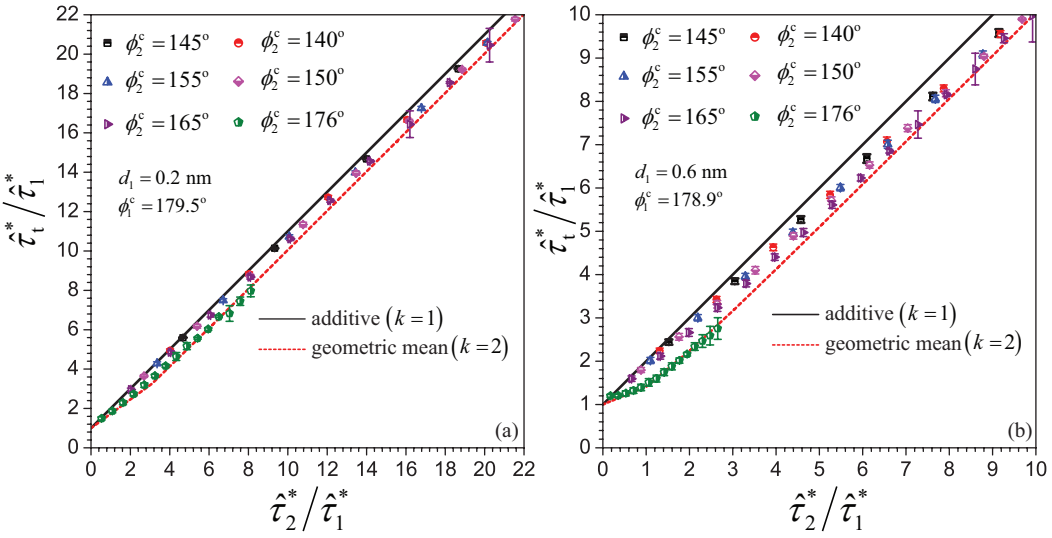

Figure 2.3: Total normalized strength $\hat{\tau}_t^*/\hat{\tau}_1^*$ versus normalized strength of type 2 obstacle $\hat{\tau}_2^*/\hat{\tau}_1^*$ for a wide range of critical angles and type 2 obstacle spacings in the weak-medium and weak-weak regimes (results in the weak-strong regime are on a different scale). Also shown are the additive rule and the geometric mean (equation 2.1 for $k = 1$ and $k = 2$, respectively). (a) $d_1 = 0.2$ nm, and $\phi_1^c = 179.5°$; and (b) $d_1 = 0.6$ nm and $\phi_1^c = 178.9°$.

limited range of d_2^*.

The subplots in figure 2.4(a) and (b) also show that the geometric mean rule describes the strengthening very well when $d_2^* < 20$ for both the weak-medium and weak-strong limits. Koppenaal et al. [53] predicted such a result by arguing that when the densities of two types of obstacles are similar (small d_2^* in our case), dislocation glide through the mixed obstacle field will require the bowing of dislocations at the average space of $d_t \propto \sqrt{N_1 + N_2}$; where N_1 and N_2 are the number of type 1 and 2 obstacles. As a consequence of equation (2.1), the total strength $\hat{\tau}_t^*$ is then the geometrical mean of individual obstacle strength.

Figures 2.3 and 2.4 show that the transition from the linear rule to the geometric mean rule occurs gradually over a range of strengths and, more strictly, a range of distances d_2^*. In the weak-medium and weak-strong regimes, the transition occurs over the range $20 < d_2^* < 67$, as shown in figure 2.4. For the weak-weak limit, the

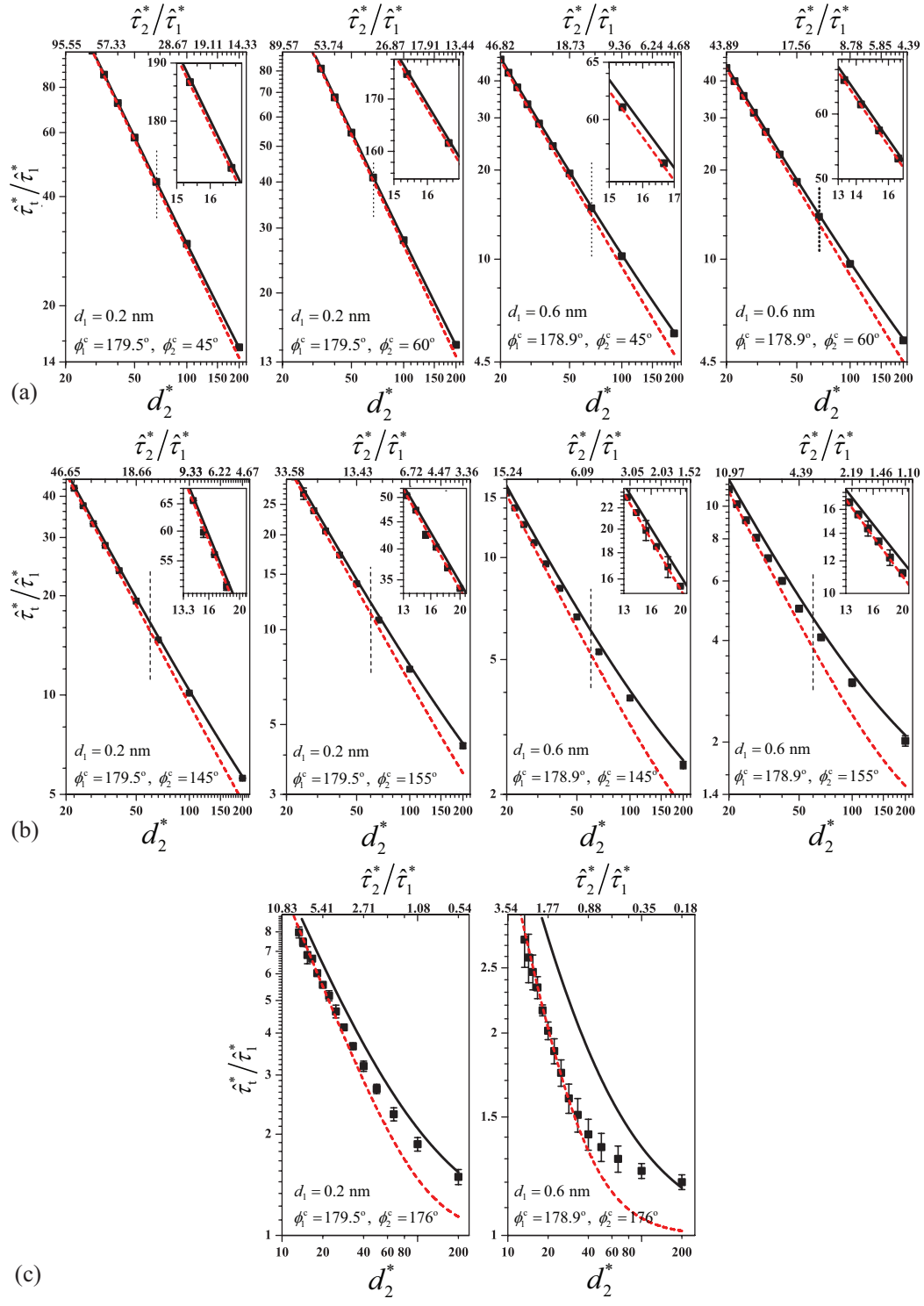

Figure 2.4: Total normalized strength $\hat{\tau}_t^*/\hat{\tau}_1^*$ vs normalized type 2 obstacle space d_2^* for various cases on a logarithmic scale. Also shown on the top axes are the corresponding normalized strengths $\hat{\tau}_2^*/\hat{\tau}_1^*$. Solid line: additive rule $k = 1$; dash line: geometric mean $k = 2$; dotted line indicates where the transition starts (at $d_2^* \sim 67$); and symbols: numerical results. (a) Weak-strong limit $\phi_1^c = 178.9°, 179.5°$ with $\phi_2^c = 45°, 60°$; (b) weak-medium limit $\phi_1^c = 178.9°, 179.5°$ with $\phi_2^c = 145°, 155°$; and (c) weak-weak limit $\phi_1^c = 178.9°, 179.5°$ with $\phi_2^c = 176°$.

transition is even wider, $30 < d_2^* < 150$; with the strength decreasing below the $k = 1$ limit immediately upon decreasing d_2^* below 200. In this limit, with ϕ_2^c very close to ϕ_1^c, a mobile dislocation cannot recognize the difference between the two obstacles and so glides as if in a field with a single type of obstacle, which is strictly attained when $\phi_2^c = \phi_1^c$. The apparent differences between figures 2.4(b) and (c) for different (d_1, ϕ_1) combinations are due to the use of a different scale on the y-axis and the relatively large variance in results for the weak-weak limit simulation, and are not due to the differences in d_1 chosen here. This is confirmed in figure 2.3 for the two weak-weak cases where the different (d_1, ϕ_1) cases yield the same behavior.

2.4 Discussions

To compare the model predictions to the experiment, we consider the study by Lagerpusch et al., [56] where both a Cu-0.65%Au solid solution alloy and a Cu-0.65%Au-0.1865%Si alloy strengthened by additional incoherent SiO_2 particles were studied. TEM results showed SiO_2 particles of radius $r \approx 49$ nm and volume fraction $f \approx 0.0066$, while mechanical compression tests were used to obtain the total and solute contributions to strengthening of $\hat{\tau}_t \approx 27.2$ MPa and $\hat{\tau}_s \approx 20$ MPa. Theoretical estimates of the stress due to particle strengthening, $\hat{\tau}_p$ [8, 56, 113], were then used, and a value of $k = 1.76$ was deduced for this system [53]. Here, we consider the Labusch model [54], accounting for the spatial range of the solute/dislocation interaction, as it is appropriate for the solid solution. This is however not a "point pinning" model, but the Labusch model identifies a length ξ_L over which statistical pinning by favorable solute configurations can occur. In a point-pinning model, these domains of size ξ_L can approximately be treated as point pinning entities with spacing $d_1 = \xi_L$. The length is $\xi_L \sim 2^{4/3} \left(\Delta\tilde{E}_{el}/\Delta\tilde{E}_p\right)^{2/3}$; where $\Delta\tilde{E}_p$ is the potential energy change per unit length due to fluctuations in the solute concentration and $\Delta\tilde{E}_{el}$ is the elastic energy per unit length due to dislocation bowing in search

of favorable configurations. Approximating the solute-dislocation interaction energy as $\bar{u} = \bar{p}\Delta V$, where $\bar{p}$ is the pressure at distance $w/2$, w is the range of the solute-dislocation interaction, and ΔV is the volume mismatch of the solute atom, then

$$\begin{aligned} \Delta\tilde{E}_{\mathrm{p}} &= \left(\frac{4c_0}{\sqrt{3}b}\sum_i u_i^2\right)^{1/2} \approx \left(\frac{16c_0w^2}{\sqrt{3}b^3}\bar{u}^2\right)^{1/2} \\ \Delta\tilde{E}_{\mathrm{el}} &= \frac{1}{4}\mu b^2 w^2 \end{aligned} \tag{2.8}$$

where c_0 is the volume fraction of solute atoms. The corresponding solute strength is

$$\hat{\tau}_{\mathrm{s}} = \frac{3b}{2^{8/3}w}\left(\frac{\Delta\tilde{E}_{\mathrm{p}}^4}{\Delta\tilde{E}_{\mathrm{el}}}\right)^{1/3} \tag{2.9}$$

Using the Cu shear modulus $\mu = 48$ GPa, Poisson ratio $\nu = 0.34$, Burgers vector $b = 0.255$ nm, $\Delta V = 3.72 \times 10^{-3}$ nm^3, $c_0 = 0.65\%$, and the experimental value $\hat{\tau}_{\mathrm{s}} \approx 20$ MPa, the interaction range w can be estimated as 1.1 nm and then the length as $d_1 = \xi_L \approx 23$ nm. For this spacing and strength, the critical angle when treated as a stop pointpinning object is $\phi_1^{\mathrm{c}} = 166°$, consistent with the angle $180° - 2\tan(2w/\xi_L) = 169°$ defined by bowing out of length w over length ξ_L. The spacing for the SiO_2 particles can be estimated by placing them in an FCC-type arrangement as $d_2 = \sqrt[3]{16\pi/3fr} \approx 682$ nm. The relative density of the obstacles is then ≈ 30, which we predict to be in the transition region between linear and geometric mean scalings, and thus broadly consistent with the value of $k = 1.76$ deduced in literature [56]. Using $\hat{\tau}_{\mathrm{p}} = 16.6$ MPa at 90 K [56], the critical angle for the point obstacles is $\phi_2^{\mathrm{c}} = 45.53°$, putting this system in the moderate-strong regime, approaching the weak-strong regime. We have used our simulation model to predict the strength given these values of ϕ_1^{c}, ϕ_2^{c}, d_1, and d_2 and obtained an exponent $k = 1.4$. Given the uncertainty in the value of $\hat{\tau}_{\mathrm{p}} = 16.6$ MPa, we consider this agreement to be reasonable but not definitive. Certainly, both theory and experiment indicate that this material system is in neither the $k = 1$ nor $k = 2$ regime.

Our results showing a regime where the friction model applies indicate that the use of the linear rule implicit in the interpretation of Haasen plots [23] may be justifiable in many systems. As an example, we consider the combination of solute and forest strengthening in Al-Mg alloys. The Mg in Al is a weak pinning entity so that, again, the Labusch model is appropriate. Scaling the results by Olmsted et al. on Al-5% Mg [80] to the case of Al-0.8% Mg studied by Diak et al. [23], the length for Al-0.8% Mg is $\xi_L \approx 18$ nm and the associated strengthening is $\hat{\tau}_1 \approx 14$ MPa, the latter consistent with experiments (≈ 11 MPa). Our results then suggest that forest hardening is expected to be approximately additive for forest dislocation spacings larger than $45\xi_L \approx 800$ nm, corresponding to forest strengthening contributions up to $\hat{\tau}_2 \sim \mu b/d_2 \approx 11$ MPa. The Haasen plot data of Diak et al. [23] on Al-0.8% Mg suggested additive strengthening up to $\hat{\tau}_2 \sim 30$ MPa or more, corresponding to forest spacings of ~ 266 nm or smaller. The experiments thus indicate additive strengths down to a smaller density ratio, suggesting that treating the Labusch solute pinning model in terms of point pinning overestimates the relevant solute spacing.

2.5 Summary

In summary, we have shown that a friction limit ($k = 1$) always arises in the limit of high obstacle density ratio, for point obstacles and line tension model. This is physically satisfying and indicates that the point-obstacle model can represent the friction limit. With applicability to dilute soultes and forest hardening in tandem with friction or solute strengthening, our results suggest applicability of the linear rule for obstacle spacing ratios larger than ~ 67, independent of the absolute strengths of the operating mechanisms, with a transition to the geometric mean rule only for spacing ratios smaller than ~ 20. Comparisons with experiments that provide the necessary data on several strengthening mechanisms show some qualitative agreement, while quantitative agreement requires more in-depth study of the friction model as applied

to solute-strengthened alloys.

Chapter 3

An atomistic model for line tension calculation of dislocation in metals

3.1 Introduction

The simulation conducted in last chapter is one example that uses line tension concept to analyze the equilibrium dislocation configurations under a given applied field. The line tension model has been widely used to analyze many problems, including the motion of dislocations through fields of obstacles and dislocation-dislocation junction formation and breaking [24, 95, 107]. Studies of interacting ensemble of dislocations, solute strengthening, dislocation-obstacle interactions, etc. [9, 57, 58, 59, 65, 80, 87, 88] all involve determinations of the energetically-favored dislocation configuration, and thus accurate line tension values have an influence on the quantitative predictability of a range of dislocation phenomena. The line tension for large scale simulations like dislocation dynamics [24, 62, 63] or the validity of various models which incorporate the line tension as a fundamental parameter [7, 106] provides connections between dislocation structures observed in simulations and experiments with the underlying models.

To increase the quantitative accuracy of results based on line tension models,

accurate values are needed and this naturally suggests resource to explicit atomistic simulations, of which there are a number of studies in the literature [11, 19, 37, 79, 87, 101]. In principle, given a reliable interatomic potential energy function for the atomic system, the molecular dynamics method provides the detailed configuration of a dislocation without any approximation and should be suitable for quantitative calculation of line tension. However, since directly capturing line tension by analyzing energy differences from simulations with different dislocation lengths is not accessible due to issues like boundary condition in the simulation cell, most studies obtain the line tension by analyzing the dislocation line structure when it interacts with pinning obstacles, such as solute atoms [87], vacancies [65], and forest dislocations [94], which have been well reviewed by Bacon, Osetsky and Rodney [9]. However, this seemingly simple approach shows great variation in the value of the line tension. For example, values for Al edge or screw vary from 0.06 to 1 eV/Å [19, 80, 87, 101]. An atomistic simulation with rigid side boundaries to pin the dislocation, and a post-processing scheme to partially account for the boundary effect, gave $\Gamma = 0.72 \pm 0.08$ eV/Å for the Al screw dislocation [101]; we will show that such boundary conditions have a huge impact on Γ. In contrast, Proville et al. [87] introduced a fictitious obstacle in the aluminium matrix to impede dislocation but only measured the dislocation shape within 5 nm around the obstacle to obtain $\Gamma = 0.06$ eV/Å; our results show that the obstacle unduly influences the dislocation shape near it, which is manifested by a strong size effect of the line tension for dislocation lengths shorter than about 40 nm, which is similar to effects obtained when fitting the shape over a small region near the obstacle. A similar approach was followed by Hardikar et. al [37], but no actual line tension value was reported, and the numerical results and line-tension-model dislocation configurations did not match very well.

Evidently, an accurate measurement of line tension at the atomistic scale is subtle. Many details — constraints due to boundary condition, simulation cell size, and obstacle size — unduly affect the dislocation configuration and introduce large

errors in the deduced line tension. To overcome these issues, we demonstrate in this chapter a procedure to accurately measure the line tension of dislocation in metals at atomistic scale based on molecular simulations. Our results show clearly a dependence of the deduced line tension on the length of the bowing dislocation segment and the applied stress, but with convergence to a single value with sufficiently high stress, sufficiently long line lengths, and sufficiently small pinning obstacles. Using this method, we report what we believe to be the most reliable line tension values for dislocations in aluminum and magnesium, and the method is easily applied to other materials. Our results for Al show that the high anisotropy predicted by the continuum model is not observed, with the difference between screw and edge line tensions being only about 20%, rather than a factor of ~ 4 as implied by continuum theory.

3.2 Simulation methods

The MD simulation at zero temperature models the motion of an initial straight edge or screw dislocation of infinite length pinned by a periodic array of rigid obstacles, bowing under a constant applied resolve shear stress. In our simulations, the Ercolessi-Adams EAM potential [26] is used for the Al simulations and the Sun EAM potential is used for Mg [105]. Dislocation core structures for these potentials are generally good in comparison to first-principles computations [76, 108, 110].

A single dislocation of either edge or screw character with line direction along the y axis is placed in a slip plane perpendicular to the z direction in a rectangular cell of dimensions $L_x \times L_y \times L_z$, as shown schematically in figure 3.1(a). We impose periodicity along the dislocation glide direction (x axis) and line direction (y axis), following the procedure developed by Osetsky et al. [81] for edge dislocations and that of Rodney [93] for screw dislocations. The desired simple shear stress was obtained using external forces applied to atoms in the outer top and bottom layers

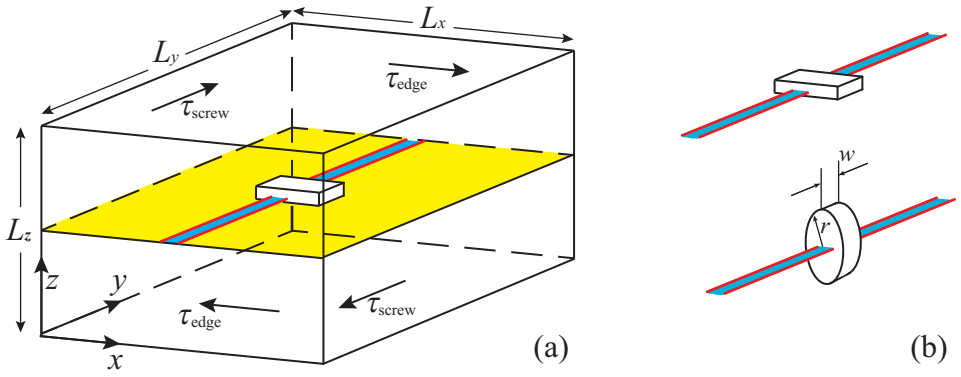

Figure 3.1: (a) Schematic illustration of the simulation cell with a single dislocation pinned by a rigid obstacle subject to an applied shear stress τ (τ_{xz} for edge dislocation and τ_{yz} for screw dislocation); (b) Shapes of rigid obstacles introduced to pin the mobile dislocation line.

in the z direction of thickness equal to the cutoff radius for the interatomic potential (3 atomic layers for Al, 4 atomic layers for Mg). For example, to achieve stress τ_{xz} acting on the edge dislocation in aluminium, the force acting on each atom in these boundary layers is $F_x = \pm\tau_{xz}A/N$, where A is the area of the surface and N is the number of the atoms in the relevant planes. The $\pm$ sign here means forces acting on the top layers and bottom layers are equal and opposite. Boundary conditions for the y and z atomic degrees of freedom are discussed below.

Once a full dislocation is introduced into the simulation cell, the system is relaxed first by conjugate gradient such that the full dislocation dissociates into two partial dislocations. A series of initial calculations were performed to check for any size effects along the x and z direction (dislocation spacing along the glide plane and simulation cell height, respectively). The splitting distance of the aluminium edge dislocation d_{sf} was evaluated and compared with previous simulations; a simulation cell with $L_x = L_z = 20$ nm is sufficient to obtain the value $d_{\text{sf}} = 14.4$ Å well known in the literature [103]. The total number of atoms in the systems is then determined by the obstacle spacing $L = L_y$. In all simulations, the largest value used is $L = 100$ nm, yielding a total of 1.8 million atoms in the simulation cell. For the aluminium edge dislocation, the Peierls stress τ_{P} was also calculated and found to be very sensitive

to the boundary conditions on the loading surfaces and the relaxation technique used. Careful previous studies gave 2.0 $\sim$ 3.0 MPa [79] and we obtain the value of $\tau_{\mathrm{P}} = 2.4$ MPa by using force boundary conditions $F_x = F_y = 0, F_z = \tau_{xz}A/N$ on the top and bottom layers and using a combination of quasi-dynamic relaxation i.e., "quench methods" [10, 12], followed by conjugate gradient with a force tolerance 1.0×10^{-8} eV/Å on any single atom. Similar studies yield $\tau_P = 14$ MPa for the screw dislocation in Al and $\tau_P = 0.4$ MPa for the basal edge dislocation in Mg, matching previous reported values [76, 79, 110].

To create an immobile obstacle that pins the dislocation, a group of atoms in the center of the dislocation line were fixed in all directions. The obstacle size along the x direction is ~ 2.6 nm, long enough to pin both partials so that the two partials have essentially the same bowing out curvature under any applied stress. The obstacle width along the y direction is $w \sim 1$ nm and the height is 2 atomic layers above and below the dislocation core in the z direction. Since the simulation cell is periodic in the y direction, the effective obstacle spacing is L_y and the dislocation segment length is $L = L_y - w$, which is essentially equal to L_y and so these are used interchangeably. In subsequent calculations, a cylindrical obstacle with radius r is introduced to investigate the influence of the rigid cluster size on the deduced line tension. The equilibrium dislocation line was examined under an increment of 1 MPa shear stress. Atoms on the dislocation line were characterized and visualized using the common neighbor analysis (CNA) [46] and potential energy, which give the same dislocation configurations. The Large-Scale Atomic/Molecular Parallel Simulator (LAMMPS) is used to perform the simulations [96] and atomic configurations were visualized using OVITO [104].

Under an applied stress $\tau > \tau_{\mathrm{P}}$, the dislocation line bows out into curved equilibrium configuration. Note that at applied stress τ the effective stress acting on the bowing dislocation is $\tau - \tau_P$. Figure 3.2 shows the bow-out shape of an edge dislocation in Al with $L = 50$ nm and $\tau = 40$ MPa, where only the atoms in the

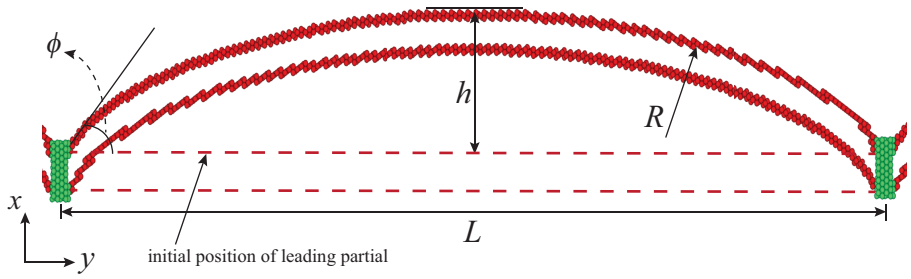

Figure 3.2: Equilibrium edge dislocation configuration in Al, for obstacle spacing $L = 50$ nm, applied stress $\tau = 40$ MPa. Red atoms: partial dislocation core atoms; green atoms: rigid obstacles, as visualized using CNA; red dash line: the initial position of partial dislocations at zero applied stress.

dislocation and obstacle are shown. It can be seen that the obstacle pins both partial dislocations and ensures the leading partial and trailing partial having almost same equilibrium curvature. For either the leading or the tailing partial dislocation, we assume the dislocation line tension Γ is a constant during the shear deformation such that at stress τ, the dislocation is approximated as an arc of a circle with radius R satisfying $(\tau - \tau_{\mathrm{P}})Rb = \Gamma$ where b is the magnitude of the Burgers vector of the partial dislocation. To obtain the value of line tension Γ, we then measure the dislocation radius of curvature R from the atomistic configurations by fitting the configuration of the leading partial dislocation using the coordination of atoms in the Levenberg-Marquardt non-linear optimization method. Values obtained using the trailing partial dislocation give the same results. The fitting accuracy can reach RMS $= 0.99$ at large τ, showing clearly that the dislocation configuration can accurately be represented by a smooth circle function. The bowing height h, as shown in figure 3.2, can also be calculated as $h = R - (R^2 - L^2/4)^{1/2}$. Figure 3.3 shows the fitted circle configuration from the atomistic configuration at different applied stresses. Values of dislocation line tension (either edge or screw character) are then calculated for different obstacle spacings L and obstacle geometries.

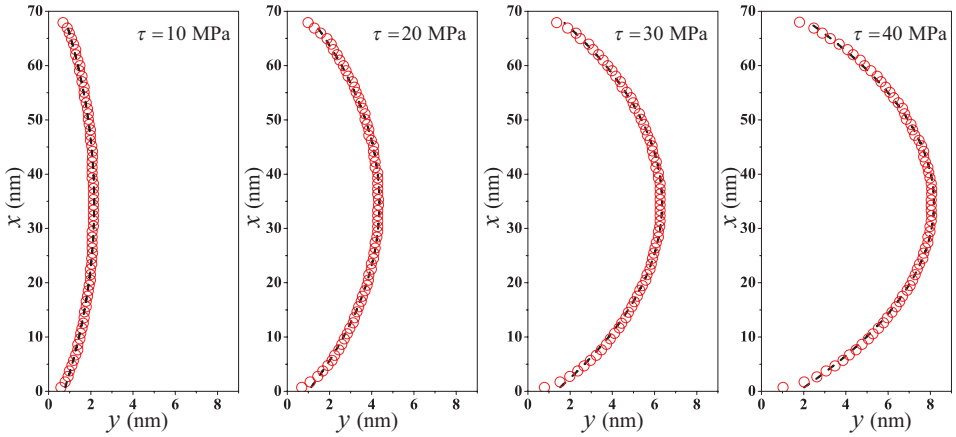

Figure 3.3: Dislocation configuration and corresponding fitted circular arc of radius R (dashed lines) at different shear stress τ, for edge dislocation in Al, obstacle spacing $L = 70$ nm.

3.3 Results and discussions

The computed line tension values for the edge dislocation in Al as a function of the applied stress τ are shown in figure 3.4(a). Figure 3.4(a) clearly shows that the deduced line tension value depends on both the obstacle space L (=dislocation length) and applied stress τ. Most importantly, the line tension values converge to a single value for large obstacle spacings $L \geq 40$ nm and large shear stresses. At low applied stresses, the deduced line tension varies greatly, from 0.1 to 0.8 eV/Å. Moreover, the values obtained using small L are always lower than those obtained for large L, and values obtained for $L = 10, 20$ nm are always far below the values obtained for longer lengths. Noting that when τ increases, the dislocation line will have reduced radius R and increased bow-out height h, more insight can be gained by examining the variation of Γ with the dimensionless parameter h/L, as shown in figure 3.4(b). The deduced value of Γ converges for large $h/L > 0.1$ when $L \geq 40$ nm. We define the converged value of Γ as the valid line tension value, obtaining $\Gamma = 0.47 \pm 0.01$ eV/Å. For the screw dislocation in Al, similar simulations and analysis are performed and yield $\Gamma = 0.57 \pm 0.01$ eV/Å, as shown in figure 3.5. Compared to previous reported values and predictions of orientation-dependent line tension

	Edge dislocation (eV/Å)	Screw dislocation (eV/Å)
aluminium	0.47 ± 0.01	0.57 ± 0.01
magnesium	0.40 (basal)	

Table 3.1: Line tension Γ for the edge and screw dislocation in Al, and the basal edge dislocation in Mg

theory, the anisotropy we measure here between edge dislocation and screw dislocation is small, with $\Gamma_{\text{edge}}/\Gamma_{\text{screw}} = 0.82$. Thus, the use of an isotropic line tension for dislocations in Al appears to be more suitable than the continuum anisotropic model for determining dislocation configurations for complicated problems. Simulations for the basal edge dislocation in magnesium are performed also, as shown in figure 3.6, providing a line tension $\Gamma = 0.40$ eV/Å. Table 3.1 lists these calculated line tensions.

For comparison, Cheng and Gumbsch [19] estimated the line tension by fitting the equation of motion to the trajectories of an accelerating straight dislocation line as measured in MD simulations and obtained a value of $\Gamma = 0.49 \pm 0.05$ eV/Å for edge dislocation in Al, very close to our result. Since the dynamic study involves no pinning or explicit bowing, it does not suffer from artifacts that arise in quasistatic simulations using explicit pinning. The agreement between two values confirms the validity of both approaches.

Our results here clearly show a size-dependence when measuring the dislocation line tension at the atomistic scale. The key concept for line tension approximation is that the dislocation is able to be represented by a smooth curve. However, at the atomistic scale, the dislocation configuration is confined in a real discrete lattice. The inability to deduce an accurate value for Γ at small τ and small segment length L stems from the fact that the atomistic dislocation motion is based on kink motion and is not flexible enough to have a smooth curvature. Our simulations show that $h/L > 0.1$ is necessary for a converged line tension value. For $L = 40$ nm, the minimum valid dislocation segment length $h/L = 0.1$ corresponds to $h = 4$ nm and a number of kinks $h/a = 10$ out of a total number of kink sites $L/a \approx 100$, where a is the lattice constant. Therefore, $h/L > 0.1$ essentially suggests that the number of

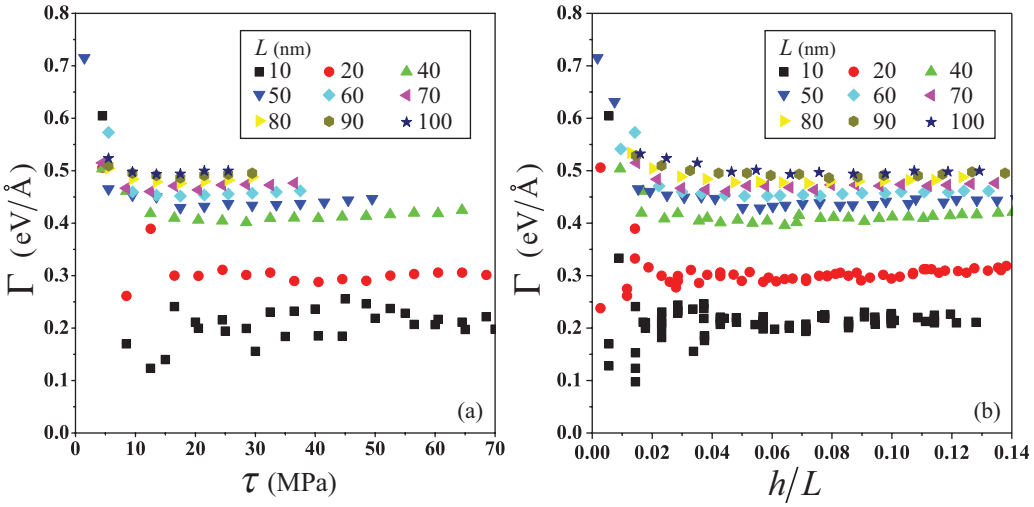

Figure 3.4: Line tension Γ for edge dislocation in Al versus (a) applied stress τ and (b) ratio of bow-out height to obstacle space h/L.

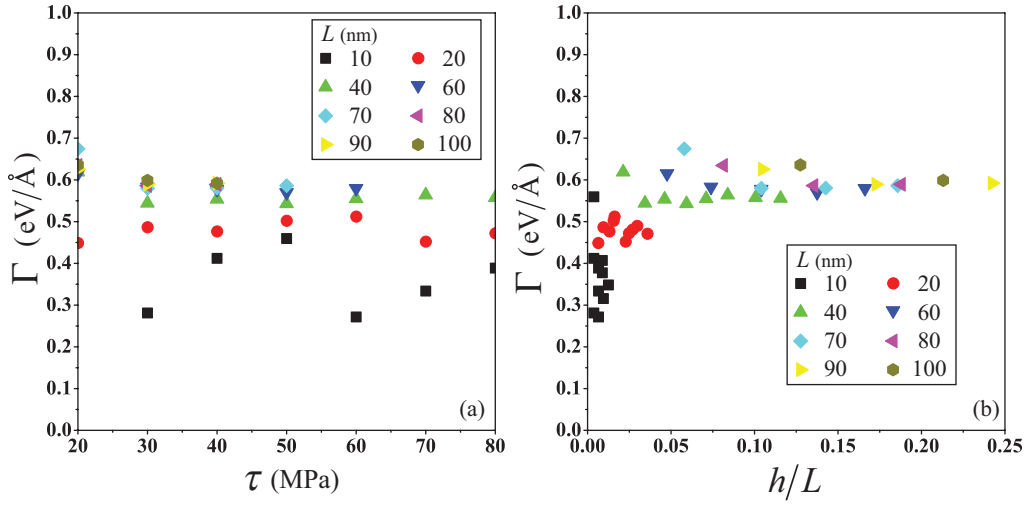

Figure 3.5: Line tension Γ for screw dislocation in Al versus (a) applied stress τ and (b) ratio of bow-out height to obstacle space h/L.

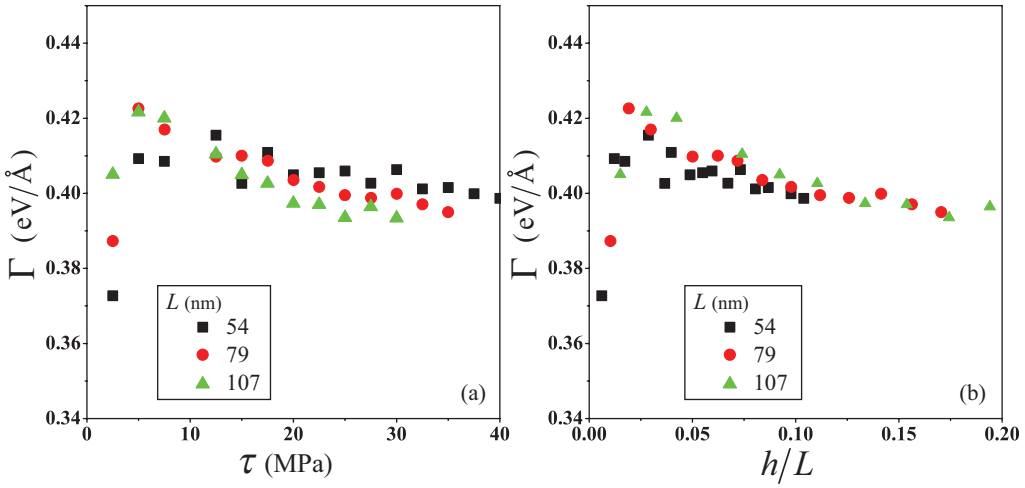

Figure 3.6: Line tension Γ for basal edge dislocation in Mg versus (a) applied stress τ and (b) ratio of bow-out height to obstacle space h/L.

kinks on the dislocation line must be at least 1/10 the number of kink sites to ensure a sufficiently smooth curved dislocation configuration. For example, figure 3.7 shows the kink configuration and kink-assisted motion of the edge dislocation in Al at $\tau = 3.5$ MPa and $L = 40$ nm, corresponding to small $h/L = 0.009$. The dislocation clearly can not be approximated as an arc having constant curvature. For small h/L, i.e. relatively few kinks along the dislocation line, the dislocation line energy involves more detailed consideration such as the kink configuration and kink-kink interactions, so that the approximation of the dislocation lines as a smooth flexible string with constant energy per unit length fails. The size dependence observed here explains the feature of previous measurement of line tension under small applied shear stress, i.e. small h/L [37].

The introduction of rigid obstacles to pin the dislocation leads to a so-called "backstress" exerted on the dislocation line [90, 101], so that raw simulation data must be adjusted by some means to correct for these spurious stresses. To gain some more quantitative insight, we investigate the influence of obstacle size on the estimated line tension. We use cylindrical rigid obstacles of varying radii r and fixed width $w = 1$ nm, as shown in figure 3.1(b). We use a single obstacle spacing

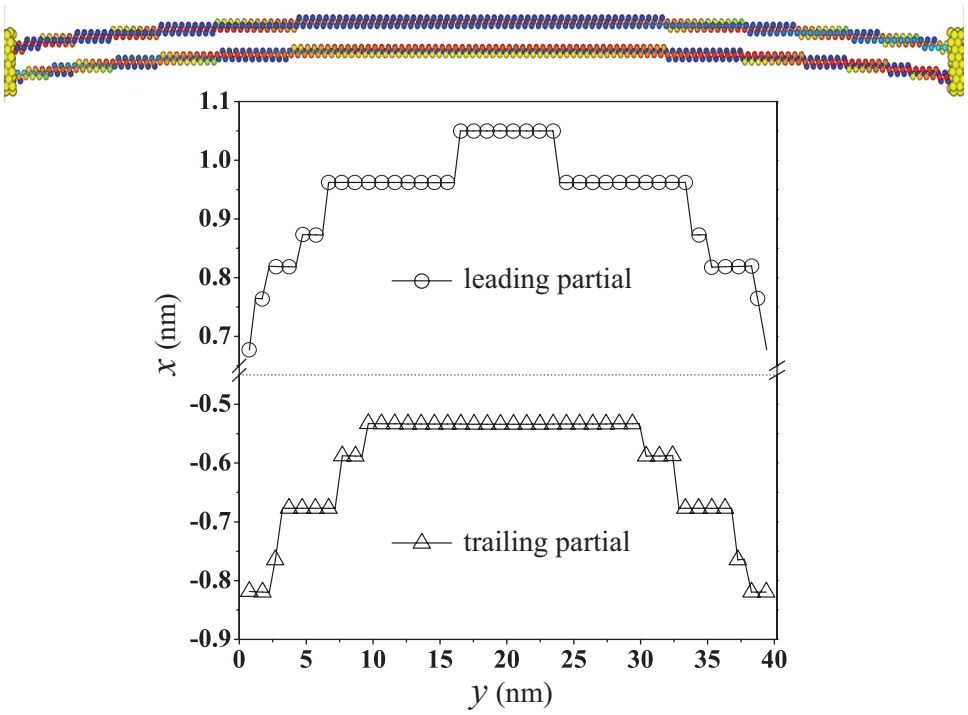

Figure 3.7: Kink configuration observed in atomistic simulations for an edge dislocation in Al of length $L = 40$ nm at low shear stress $\tau = 3.5$ MPa. Atoms in the core are colored by the potential energy.

$L = 60$ nm which is sufficient to obtain converge results for small obstacles. The parameter $\alpha = \pi r^2/(L_x L_z)$ ($\alpha = \pi r^2/(L_y L_z)$ for screw dislocations) is introduced to quantify the results, where $\alpha = 1$ is equivalent to a fixed lateral boundary condition along the dislocation line. Figure 3.8 shows the deduced line tension Γ versus the boundary parameter α, clearly demonstrating the influence of obstacle constraint on the dislocation configuration. For comparison, the line tension of screw dislocation calculated by Shenoy and Phillips are also shown in figure 3.8, including the values with/without the boundary force correction [101]. It can be seen that with increasing α, the apparent line tension values increases significantly. The boundary force correction procedure for $\alpha = 1$ by [101] reduces the final result by 50% but it still differs significantly (25%) from the true value, demonstrating that making large corrections to highly inaccurate estimates in not a viable strategy for high accuracy.

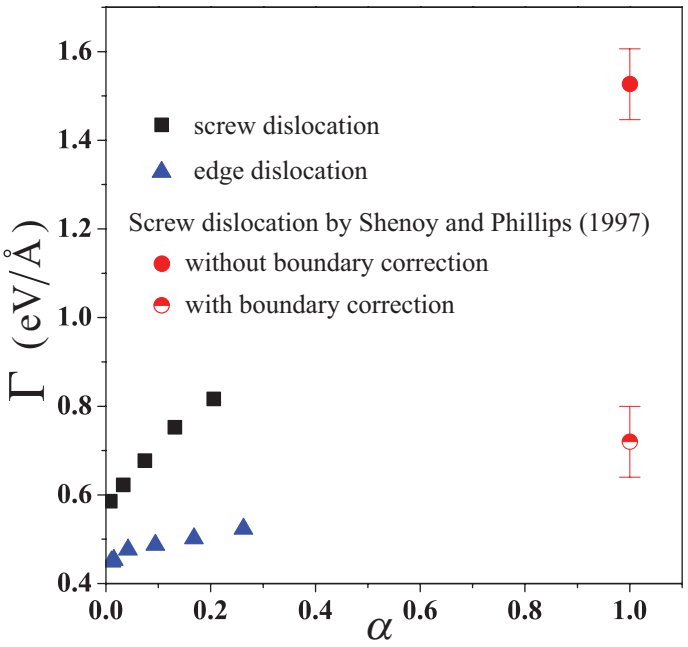

Figure 3.8: Line tension Γ versus the ratio α (rigid obstacle area)/(lateral simulation size), showing a strong effect of boundary conditions. Also shown are results of Shenoy and Phillips with fixed boundary condition before and after applying a boundary correction [101], showing significant error even in the latter case.

An obstacle of any size also influences the shape of the dislocation line in the region around it, which is why long dislocation line lengths are needed to obtain accurate results (figure 3.4-3.6). The small line tension quoted by Proville and Patinet [87] is obtained using the shape only on the dislocation shape within 5 nm of the obstacle, which is inadequate. Our results reflect this trend, with very small values of line tension obtained from small L, i.e. when significant fraction of the entire dislocation line is near the obstacle. This also shows that is it not appropriate to capture the line tension by measuring the bowing angle ϕ. In principle, ϕ and R are related but the obstacle-induced stresses poison the value of ϕ and lead to errors in the estimated line tension.

3.4 Summary

In this chapter, we have proposed a simple but robust method to calculate accurate values of line tension for dislocation in metals at atomistic scale. Using the bow-out configuration of dislocation line pinned by obstacles obtained from atomistic simulations, our results show that the dislocation segment length and magnitude of applied shear stress greatly affect on the line tension measurement, due to the intrinsic kink configuration at atomic scale. Sufficient dislocation line length and a sufficient applied stress are necessary in order to minimized the influence due to intrinsic step-size kink configuration of dislocation at atomistic scale. Sufficiently small obstacle sizes are also need to reduce spurious constraints on the dislocation. The procedure here however can be easily extended further to address anisotropy by using an elliptical shape to approximate the line configuration, as long as the geometry requirements identified here are satisfied. Our results yield accurate line tension values for Al and Mg, for the interatomic potentials used here, that can be used in higher-scale studies of dislocation interactions, dislocations, dislocation dynamics and models where a continuum line tension is required.

Chapter 4

Solute dislocation-junction interactions in metal alloys

4.1 Introduction

The line-tension simulation with point-pinning assumption presented in the chapter 2 has clearly shows that the validity of linear additivity of the total strength due to two strengthening mechanisms is dependent on the relative density difference of two strengthening precipitates. The rule of mixture, equation (1.10) taking an exponent value $k \neq 1$ implies the involved individual strengthening mechanisms have influence on each other, which then leads to the reduction of their strength. The interaction between two strengthening mechanisms remain unclear yet. The reported study in this topic is very rare. Chen et al. studied the solute segregation on the dislocation junctions using kinetic Monte Carlo method and 3-D DD simulations [18]. They found that the solute segregation can result in both strengthening and weakening effect, depending on the evolution of dislocation junctions. Recent 3D DD simulations conducted by Monnet and Devincre probably is the most extensive study on the solute friction effect on the forest hardening behavior [66]. With the friction limit, the solute strengthening in their work was represented by a homogeneous

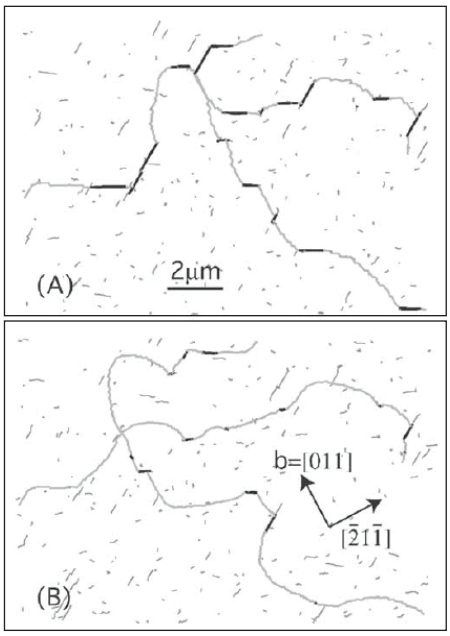

Figure 4.1: Microstructure obtained from 3D DD simulations [66]. Gray lines are dislocation of the primary slip system cutting forest dislocations $\rho_{\mathrm{f}} \approx 10^{12} m^{-2}$; bold segments are Lomer junctions. (A) DD simulation with $\tau_{\mathrm{F}} = 1$ MPa and (B) with $\tau_{\mathrm{F}} = 30$ MPa.

friction stress along the whole slip plane. Such a constant friction stress introduces a shielding of elastic interaction when dislocation intersects with each other to form dislocation junctions, resulting in a reduction of the length of the formed junction. This effect is then verified by the DD simulations which modeled the formation of junction under alloy friction at zero applied stress. Moreover, as shown in figure 4.1, the microstructure taken from the DD simulations clearly shows that the number of formed junctions decreases due to the existence of solute friction, resulting in the reduction of the strength provided by the network of junction locks. A model based on dislocation elasticity is the proposed to address the modification of the reduced dislocation-dislocation interaction observed in DD simulations and suggests such a softening is mainly due to the decrease of the line tension of dislocations involved in the dislocation-dislocation interactions.

As discussed in chapter 1, the line tension approximation of the dislocation has its

limitation on atomic scale and most of simulations and theories at macroscopic scale rely greatly on the information obtained from atomistic simulations. Even though simulations at atomistic and quantum scale have been developed extensively to study the individual strengthening mechanism, the numerical study at atomic scale on the combination of two different strengthening mechanisms operating together has never been carried out.

Therefore, missing the atomistic details for dislocation junction structure in metal alloy systems and previous success in atomistic simulations for strengthening due to individual strengthening obstacles inspire us to numerically study the junction structure and associated strength with solute atoms present at atomistic scale. In this chapter, we use Molecular Static (MS) method to simulate the formation and strength of the Lomer-Cottrell (LC) locks in FCC Al/Mg alloys. The results obtained from MS simulations is then compared with the previous 3D DD simulations and the effect of the solute friction due to solute atoms on the dislocation junction is analyzed in detail.

4.2 Simulation Methods

The Molecular Statics (MS) models the motion of an initial straight edge dislocation of infinite length pinned by two forest dislocations in aluminum matrix strengthened by Mg solute atoms. A schematic of the simulation cell used in the atomistic simulations is shown in figure 4.2(a). The simulation cell has a rectangular shape with the x-axis oriented along $[0\bar{1}1]$, y-axis along $[2\bar{1}\bar{1}]$ and z-axis along [111]. The dimensions of the simulation cell are 85 nm along x direction, 150 nm along y direction and 15 nm along z direction, about 11 million atoms in total, which is sufficient to minimize the influence due to boundary condition and loading techniques as shown below. Three dislocations are initially inserted in the simulation cell to form two LC junctions. Using the technique developed by Osetsky and Bacon [81], one edge

dislocation with the $a_0/2[01\bar{1}]$ Burgers vector where a_0 is the lattice constant residing in the center of the simulation cell on the (111) plane with $[2\bar{1}\bar{1}]$ line direction is introduced to represent the mobile dislocation. Two mixed type forest dislocations are inserted into the simulation cell to generate LC junctions along with the mobile edge dislocation and ensure the periodic boundary condition along the y direction. First forest dislocation with $a_0/2[\bar{1}0\bar{1}]$ Burgers vector residing on $(\bar{1}\bar{1}1)$ plane has $60°[0\bar{1}\bar{1}]$ line orientation and second forest dislocation with $a_0/2[110]$ Burgers vector on $(\bar{1}1\bar{1})$ plane has $120°[0\bar{1}\bar{1}]$ line orientation. Two forest dislocations intersect with the mobile dislocation at coordinates $y = \pm 37.5$ nm such that the forest dislocations have a constant average space $L = 75$ nm along the edge dislocation line direction, corresponding to a forest density $\sim 10^{14}$ m^{-2}. The initial separation between the forest dislocations and the mobile edge dislocation is about 8Å. The geometry of dislocation interactions for the three dislocations here is bested understood by the Thompson tetrahedron shown in figure 4.2(b). Mg atoms with certain concentration c is introduced in the Al matrix by randomly choosing c atomic fcc sites in each plane parallel to the slip plane and replacing the Al atoms on these sites by Mg atoms, with the remaining sites occupied by Al atoms.

In our simulations, the Ercolessi-Adams EAM potential [26] was used for Al and was augmented by the Liu et al. EAM potentials [60, 61] for the Al/Mg simulations. Dislocation core structures for these potentials are generally good in comparison with the first principle computations [108]. For these potentials, the Burgers vector $b = 0.2851$ nm, the zero temperature elastic modulus $C_{11} = 126.8$ GPa, $C_{12} = 59.3$ GPa and $C_{44} = 36.7$ GPa. Variation of elastic modulus due to addition of Mg solutes concentration is negligible [80].

The chosen boundary condition and loading techniques along the x and z direction are then chosen based on a series of initial calculations. The splitting distance of the Al edge dislocation d_{sf} was evaluated and compared with previous simulations to verify that a simulation cell with height $L_z = 15$ nm is sufficient to obtain

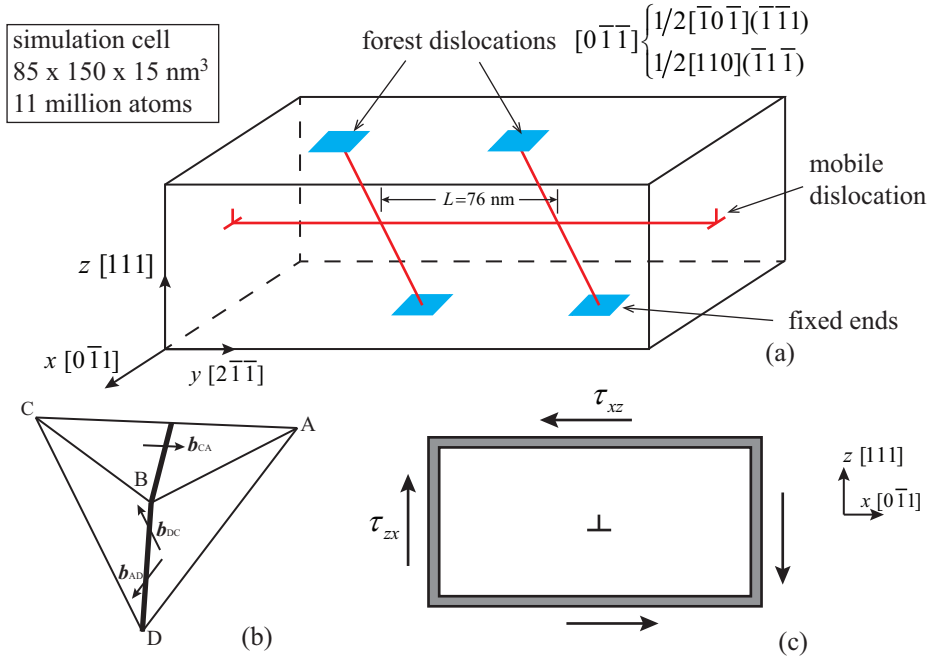

Figure 4.2: (a) Schematic illustration of the simulation cell where a single edge dislocation is pinned by two mixed-type forest dislocations in Al/Mg alloy systems. (b) Thompson tetrahedron showing the dislocation structure used to form two LC locks inside the simulation cell. (c) Schematic of the simulation cell subject to a pure shear deformation by force loading techniques.

the value $d_{\mathrm{sf}} = 14.4$Å well known in the literature [103]. Simulations in chapter 3 have shown that imposing shear deformation to the simulation cell by applying external force on atoms close to the surface was able to predict an accurate Peierls stress value. Note that the insertion of 60°/120° forest dislocations breaks the periodicity along x direction, the simulation box therefore has four free surfaces, left and right in x direction and top and bottom in z direction, as shown in figure 4.2(c). We then impose pure shear deformation on the simulation cell by adding external forces on the atoms in the outer layers along x and z directions of thickness equal to the cutoff radius of the interatomic potential (3 atomic layer for Al), denoted as shaded region in 4.2(c). To achieve shear stress τ_{xz} applied to the simulation cell, the force acting on each atom in the top and bottom layers is $\vec{\mathbf{F}}_{\mathrm{z}} = (F_x = \pm\tau_{xz}A_z)/N_z, F_y = 0, F_z = 0)$ where A_z is the area of the surface and N_z is the number of the atoms in the relevant planes. The $\pm$ sign here means forces acting on the top layers and bottom layers are equal and opposite. Similarly, shear stress τ_{zx} is applied by adding force $\vec{\mathbf{F}}_{\mathrm{x}} = (F_x = 0, F_y = 0, F_z = \pm(\tau_{zx}A_x)/N_x)$ on each atom in the right and left atomic layers along x direction with A_x and N_x defined accordingly. To ensure the torque equilibrium, the surface area A_x and A_z are defined as follows, $A_x = L_y\left(\langle z\rangle_{\mathrm{top}} - \langle z\rangle_{\mathrm{bottom}}\right)$ where $\langle z\rangle_{\mathrm{top}}$ and $\langle z\rangle_{\mathrm{bottom}}$ are the average value of z coordinates of atoms in the top and bottom loading layers; $A_z = L_y\left(\langle x\rangle_{\mathrm{right}} - \langle x\rangle_{\mathrm{left}}\right)$ where $\langle x\rangle_{\mathrm{right}}$ and $\langle x\rangle_{\mathrm{left}}$ are the averages of x coordinates of atoms in the right and left loading layers. L_y here is the length of the simulation cell along the y direction. Moreover, atoms on the ends of forests are frozen to fix the forest dislocations during deformation, as shown in figure 4.2(a). The equilibrium dislocations structure is examined under an incremental of 2.5 to 5 MPa shear stress. At given applied stress, the system is relaxed to equilibrium using a combination of quasi-dynamic relaxation i.e., "quench methods" [10, 12], followed by conjugate gradient. The force tolerance is 1.0×10^{-6} eV/Å on any single atom. Using the boundary conditions and loading techniques mentioned above, we obtained the

Peierls stress $\tau_{\mathrm{P}} = 2.7$ MPa for edge dislocation in Al, close to the range $2.0 \sim 3.0$ MPa reported in previous careful calculations [79] and the value $\tau_{\mathrm{P}} = 2.7$ MPa obtained in last chapter. Note that Mg solute atoms are randomly distributed in Al/Mg system, 8 to 10 statistical replicas under same Mg concentration c and junction geometry but spatial difference of the Mg atoms were generated and simulated, and the results quoted below are the average over all these realizations, with error bars indicating standard variation among the set of replicas. Atoms on the dislocation line were characterized and visualized using the common neighbor analysis (CNA) [46]. The Large-Scale Atomic/Molecular Parallel Simulator (LAMMPS) is used to perform the simulations [96] and atomic configurations are visualized using OVITO [104]. For clarity, perfect crystalline atoms except the Mg solute atoms in atomistic configuration are not shown in following figures.

4.3 Results and Discussion

4.3.1 Strengthening due to single type of strengthening mechanism

Atomistic simulations with either solute atoms or forest dislocations operates alone are carried out first to obtain the strength due to single type of pinning site. First, we describe the results from MS simulations of an initially straight edge dislocation with length $L = 150$ nm glide through a field of randomly distributed Mg solutes in Al. The length of dislocation here is much longer than the Labusch length suggested by previous models and simulations [80]. The Mg concentration c considered here varies from 0.01 to 0.08. Since we don't have forest dislocations here, the periodicity of the simulation cell along x direction is maintained such that the dislocation can transit the cell with a shear of the Burgers vector changing the Mg configuration after each pass across the cell length in x direction. Previous simulation [80] showed that the dislocation is pinned by a local solute configuration which corresponds to a

local energy minimum. Under an applied stress, the energy barrier to the dislocation escape from the energy minima is reduced and the dislocation de-pins from the solute configuration at critical stress. What we obtained from the simulations here is the maximum stress required for the dislocation glide through all possible pinning sites inside the simulation cell and we define this value to be the total friction stress τ_{F}. Then the strength τ_{S} due to solute atom hardening is

$$\tau_{\mathrm{S}} = \tau_{\mathrm{F}} - \tau_{\mathrm{P}} \tag{4.1}$$

where $\tau_{\mathrm{P}} = 2.7$ MPa is the Peierls stress calculated above. The values of solute strength τ_{S} for different concentration c is listed in table 4.1 and plotted in figure 4.3. Formal developed analytical model [59] based on the detailed analysis of solute/dislocation interaction energy showed that the zero-temperature solute strength $\tau_{\mathrm{y0}} = Kc^{2/3}$, where K is defined by the characteristic energy change ΔE_{c} associated with each pinned mobile dislocation segment of Labusch length ξ_{L} and surrounding segment with length ξ_{L}. Previous Molecular Dynamics calculations [80] using same potential provided a characteristic energy $\Delta E_{\mathrm{c}} = \Delta E_{\mathrm{p}} - \Delta E_{\mathrm{el}} = 4.88 - 1.22 = 3.66$ eV, with $\xi_{\mathrm{L}} = 11$ nm which is smaller than the forest spacing $L = 75$ nm used below. ΔE_{p} is the potential energy change due to solute/dislocation binding and ΔE_{el} is the elastic energy variation in dislocation length change. From ΔE_{c}, the model gives $\tau_{\mathrm{y0}} = 182.32c^{2/3}$. Here, we don't have the fluctuations and therefore the strength is instead related to the potential energy ΔE_{p} only, leading to a scaling $\tau_{\mathrm{y0}} \sim \frac{\Delta E_{\mathrm{p}}}{\Delta E_{\mathrm{c}}} 182.32c^{2/3} = 243c^{2/3}$. For comparison, the model prediction is shown in figure 4.3. The $c^{2/3}$ dependency on τ_{S} still exists for numerical results but the fitted parameter $K = 351.3$ is higher than model prediction where $\tau_{\mathrm{y0}} = 243c^{2/3}$. This is due to the fact that τ_{S} here is the upper bound of the solutes contribution rather than the model prediction that the mobile dislocation is able to encounter on average as gliding through the whole field. The difference of τ_{S} and the analytical model prediction will be discussed more below where two strengthening mechanisms

c_{Mg}	τ_{F} (MPa)	τ_{S} (MPa)	L (nm)	τ_{J} (MPa)	τ_{T} (MPa)	$\tau_{\mathrm{S}}+\tau_{\mathrm{J}}+\tau_{\mathrm{P}}$ (MPa)
0.01	19.2	16.5	75	52.3	66.3	71.5
0.02	28.0	25.3	75	52.3	73.3	80.3
0.05	51.3	48.6	75	52.3	85.3	103.6
0.08	67.5	64.8	75	52.3	97.5	119.8

Table 4.1: The simulated total friction stress τ_{F} and the strengths for Mg solutes hardening $\tau_{\mathrm{S}} = \tau_{\mathrm{F}} - \tau_{\mathrm{P}}$ ($\tau_{\mathrm{P}} = 2.7$ MPa) at difference solute concentration c; the junction strength τ_{J} at forest spacing $L = 75$ nm, associated with a forest density $\sim 10^{14}\mathrm{m}^{-2}$; the simulated overall hardening strength τ_{T} due to combination of solute and forest hardening; the linear summation of solute strength, junction strength and Peierls stress $\tau_{\mathrm{S}}+\tau_{\mathrm{J}}+\tau_{\mathrm{P}}$.

involves together.

The strength introduced by the LC locks is computed by simulating the mobile edge dislocation breaking through two forest dislocations in pure Al. The initial dislocation structure is shown in figure 4.2(a). At free state (without any applied stress), the dislocation arms dissociate into Shockley partial dislocations in their glide plane and two LC junctions are formed by the interaction of the dissociated partial dislocations as shown in figure 4.4. The two formed LC junctions in our simulation cell have same strength while they have different line direction along the line of intersection between glide planes of initial dislocations. The inset in figure 4.4 gives one example of the detail structure of the LC junctions at atomistic scale. The junction segment itself is built up of two parts, a stair-rod Lomer-Cottrell segment with a $a_0/6[\bar{1}\bar{1}0]$ Burgers vector $\delta\gamma$ and a Lomer dislocation with $a_0/6[\bar{1}\bar{1}0]$ Burgers vector DC, as expected from the crystallographic analysis using the Thompson tetrahedron in figure 4.2(b). Figure 4.5 shows the destruction process of the LC junctions. Note that the shear stress we applied on the simulation cell has very small component acting on the forest dislocations such that we assume the forest arms don't experience any external force acting on it. Only the mobile edge dislocation bows out due to the resolved shear stress acting on it. And the motion of the forest dislocation arms are only due to the movement of junction ends. In our simulations, the junctions translate along its line direction and its length increases first under

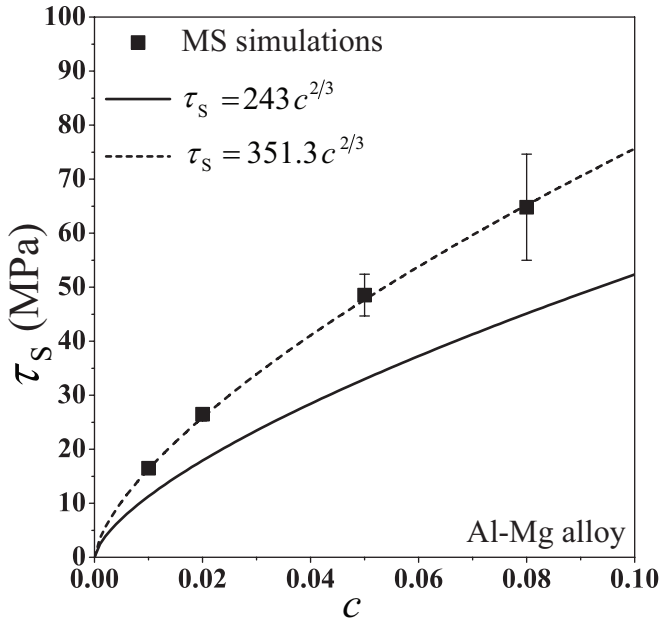

Figure 4.3: The variation of the strength of Mg solutes τ_S with the solute concentration c.

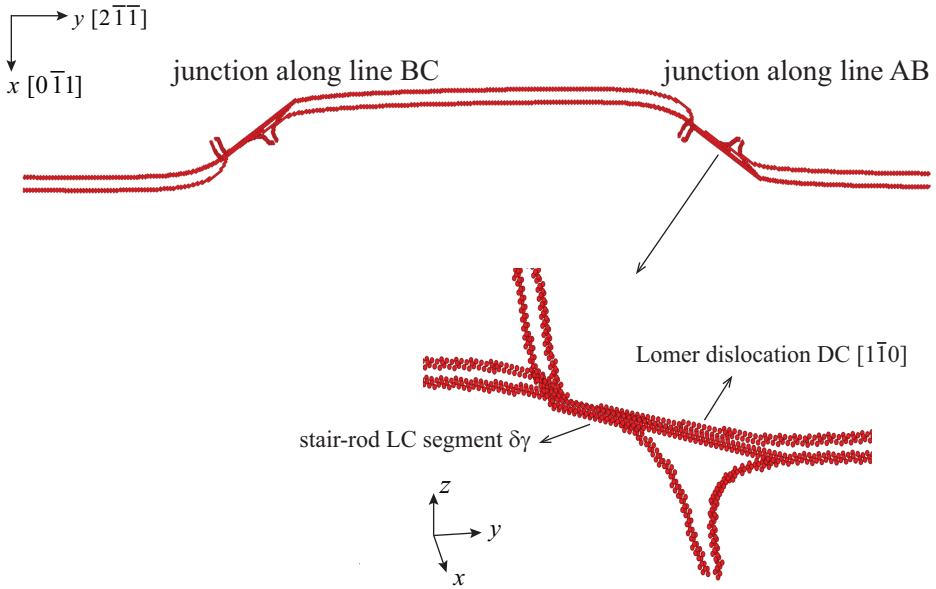

Figure 4.4: Junction geometry at free state (zero applied stress) obtained from MS simulations. Red atoms are the atoms on the dislocation line, chosen based on their CNA.

small stress level and monotonically decreases with increasing applied stress. The junction length eventually decreases to zero and the segment vanishes altogether at some critical shear stress value τ_{J}, corresponding to the forest strength. Once the mobile dislocation breaks through the forest dislocations, the step on the mobile dislocation after bypassing the forests leads to a tube of vacancies formed behind the mobile dislocation. In our simulations, the LC junctions were destructed under an applied stress equal to 55 MPa, giving the junction strength $\tau_{\mathrm{J}} = 55 - \tau_{\mathrm{P}} = 52.3$ MPa, where the Peierls stress is treated as the homogeneous friction stress. With the forest model, the junction strength τ_{J} to destruct the junction is proportional to $\mu b/L$, or $\mu b\sqrt{\rho_{\mathrm{f}}}$ equivalently, where $\mu = C_{44}$ is the shear modulus, b is the magnitude of the Burgers vector, L is the forest spacing and ρ_{f} is the density of forest dislocations. That leads to $\tau_{\mathrm{J}} = \alpha\mu b/L$ and α denotes the dimensionless hardening coefficient. The value of α depends on the junction type and initial dislocation structures [24, 86, 97, 102]. Having the value in our simulations, $\tau_{\mathrm{J}} = 52.3$ MPa, $\mu = 36.7$ MPa, $b = 0.2851$ nm and $L = 75$ nm, we have the hardening coefficient for the LC locks $\alpha_0 = \tau_{\mathrm{J}} L/\mu b = 0.37$.

4.3.2 Dislocation-junction interactions in Al/Mg metal alloys

In previous section, we have obtained the strength due to individual type of strengthening obstacles present. Both the results give similar scaling compared with previous theoretical predication [57] and calculations [95]. We now explore the overall strength due to the combination of solute atoms and forest dislocation, i.e. dislocation junction locks. More specifically, we are interested in whether the solutes friction has effect on dislocation-dislocation interactions, as observed in 3D DD simulations [66].

Note that we have shown in previous simulations that the strength due to solute atoms relates to certain local solutes configuration. Here we firstly conduct simulation in which the mobile dislocation glides through a given randomly distributed

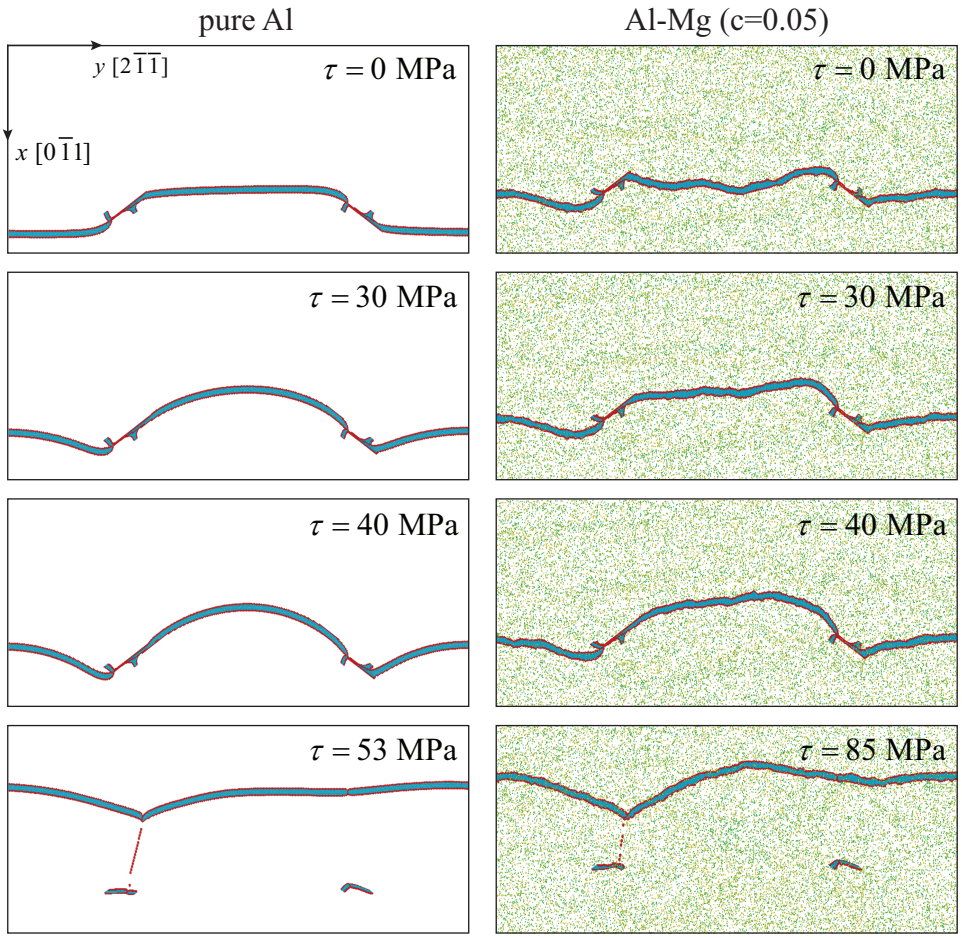

Figure 4.5: The structure of the dislocations during the formation and destruction of LC junctions in pure aluminium and Al/Mg alloys ($c = 0.05$). τ in the figure is the stress applied on the simulation cell. Red atoms, dislocation lines; blue atoms, the stacking faults; yellow/green atoms: Mg atoms positioned on the first plane above/below the slip plane of the mobile dislocation.

Mg solutes field, obtaining the strength τ_S under the predefined solutes distribution and also the position of the local solutes configuration which contributes τ_S. Once hardening at given solutes contribution is confirmed, two full forest dislocations are inserted into the simulation cell under the same Mg solutes distribution. The position of the forest dislocations is chosen such that the local solute configuration associated with τ_S is inside the region where the mobile dislocation glides through during its breaking the LC locks. Note that the insertion of a mixed-type forest dislocation will deform the atoms associated with its edge and screw component. In our case, the displacement due to the edge components of the two forests is canceled out by each other but the screw components will introduce a rigid shift for each atom along x and z direction. The rigid shift of atoms inside the simulations cell however will not change the relative solute configuration to the mobile dislocation and therefore the solute strength τ_S is ensured to be same as previous calculation in which the forest dislocations is missing under the same solute distribution.

In the following discussion, we firstly denote the solute hardening contribution by its solute strength τ_S and treat τ_S constant along the whole glide plane. As discussed before, τ_S is the upper limit of all possible hardening effect that the solutes can contribute on the whole glide plane. Figure 4.5 shows the formation and destruction of the LC junctions with/without Mg solutes in Al matrix. The formation and structure of the LC junction in Al/Mg alloys remain same as the junction structure evolution in the pure Al. Two LC junctions are formed by the interaction of the dissociated Shcokley partial dislocations and the junction segments are composed by the stair-rod Lomer-Cottrell segment and Lomer dislocations. The destruction happens when the applied shear stress reach the critical value τ_T by which the mobile dislocation bows out sufficiently to reduce the junction length to zero.

We firstly check the initial length of the formed LC junctions at zero applied shear stress, under the influence of solute strengthening. Note that the initial junction length is a function of the length of the dislocation arms which form the junction.

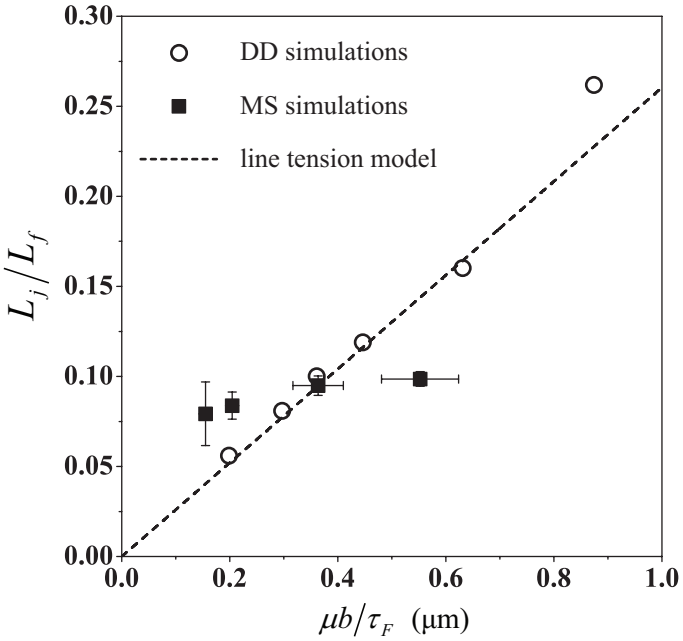

Figure 4.6: The variation of the normalized LC junction length $L_\mathrm{j}/L_\mathrm{f}$ at zero applied stress with the inverse total friction stress $\mu b/\tau_\mathrm{F}$.

Here we have asymmetric dislocation junction with the mobile dislocation segment length $L_\mathrm{m} = 75$ nm and the forest segment length $L_\mathrm{f} = 15$ nm, therefore the formed junction length L_j is mainly determined by L_f. At certain solute concentration c, the LC junction will experience a total friction stress $\tau_\mathrm{F} = \tau_\mathrm{S} + \tau_\mathrm{P}$. For pure Al, we have total friction $\tau_\mathrm{F} = \tau_\mathrm{P} = 2.7$ MPa and the initial junction length at free state $L_\mathrm{j} = 1.28$ nm which gives $L_\mathrm{j}/L_\mathrm{f} = 0.09$. Figure 4.6 gives the variation of the junction length normalized by the segment length $L_\mathrm{j}/L_\mathrm{f}$ with the inverse friction stress $\mu b/\tau_\mathrm{F}$ for c from 0.01 to 0.08. Also shown in figure 4.6 are the results obtained from 3D DD simulations done by Monnet and Devincre [66]. The results show noticeable difference in MS and DD simulations. In the DD simulations, the junction length L_j at zero load is linearly dependent on the inverse friction stress $1/\tau_\mathrm{F}$, which can be explained by the line tension model with a homogeneous alloys friction. However, in MS simulations, the variation of initial junction length L_j under zero load is not obvious under different friction stress τ_F, i.e. different solute strength τ_S. In the DD

simulations, the friction stress τ_{F} is homogenous along the whole field and therefore dislocation arms connected at the junction triple nodes exhibit a significant bow-out curvature which is proportional to $\mu b/\tau_{\mathrm{F}}$ when they interact together to form the junction locks. The bow-out geometry due to τ_{F} introduces a screening effect and leads to a linear scaling of the junction length with inverse friction. Whereas in the MS simulations, the friction stress τ_{F} due to solutes hardening is not a global quantity and the formed initial junction length L_{j} is actually dominated mostly by the local solute configuration around the junction position. We tried in the MS simulations with incorporating different solutes configurations around the junction formation site, including the configuration that gives the upper limit of the solute strength τ_{S} and even at high solute concentration $c = 0.08$, no significant curvature observed for the dislocation arms close to the triple nodes of the junctions. Therefore, the screening effect of solute strengthening in the DD simulations on the dislocation junction length at zero applied shear stress is not observed at atomistic scale.

Consequently, in DD case, the reduction of junction length at zero load due to alloy friction will indirectly lead to a reduction of junction strength with alloys frictions. But from the results showing here at atomistic scale, we should not expect the junction strength reduction due to such screening effect of solute friction on the initial formation of the junction. Next we consider whether there is any other factor that the solute friction will influence the strength of the LC locks. Normally, when solute atoms and forest dislocation operate together, the overall strength can be written as the summation of solute strength τ_{S}, the Peierls stress τ_{P} and the forest strength which is the junction strength τ_{J}

$$\tau_{\mathrm{T}} = \tau_{\mathrm{F}} + \tau_{\mathrm{J}} = \tau_{\mathrm{S}} + \tau_{\mathrm{P}} + \alpha\frac{\mu b}{L} \tag{4.2}$$

and α is associated forest hardening coefficient as mentioned before. Previous 3D DD simulation has shown that given a homogeneous alloy friction, the dislocation reaction is reduced due to the solutes screening effect acting on the junction triple

points. Here we check this with the atomistic simulations, combined with the values of solute contribution τ_S (upper limit) and the forest strength τ_J, which were measured individually. Table 4.1 lists the obtained overall strength τ_T obtained from MS simulations required for the mobile dislocation glide though both the LC locks and solute atoms. It clearly shows that the value of τ_T is smaller than the summation of τ_S, τ_J and τ_P. Using the strength values τ_T, τ_S, τ_J, we can calculate the hardening coefficient α at different solute concentration using equation (4.2), and compare the result with the 3D DD simulations. Figure 4.7 gives the variation of the normalized forest hardening coefficients α/α_0 with the inverse total friction stress $\mu b/\tau_F$ at log scale. $\alpha_0 = 0.37$ in the MS simulation corresponds to the pure Al where forest dislocations operate alone and $\tau_F = \tau_P = 2.7$ MPa. $\alpha_0 = 0.27$ in DD simulation is obtained at $\tau_F = 0.1$ MPa. Given the values listed in table 4.1, similar scaling law is observed from the MS simulations to the DD simulations. At high friction stress, $\mu b/\tau_F < 1$ μm, the hardening coefficient α decreases linearly with the $\log(\mu b/\tau_F)$ increasing. Once the friction stress is smaller than 10 MPa ($\mu b/\tau_F > 1$ μm), α is a constant which suggests that the two types of strengthening obstacles act independently. In DD observations, such a linear reduction of α versus $\log(\mu b/\tau_F)$ can be attributed to two factors: (i), the initial junction length is greatly reduced due to the screening effect of homogenous alloy friction, as discussed above; (ii), the average spacing between pinning junctions l, i.e. the number of forests that currently interact with the mobile dislocation, decreases with τ_F increasing, visualized in figure 4.1. Note that the forest strength scales as $l \sim F^{-1/2}$ from Friedel statistics [31], the reduction of l due to homogenous alloy friction results in the reduction of the forest strength. However, these two factors do not come into consideration in the atomistic simulations. As shown in figure 4.6, the variation of initial junction length L_j changes only by 10% with τ_F varying from 2.7 to 67 MPa, whereas in DD simulations, L_j changes greatly by almost 80% with same variation of alloys friction. And in the atomistic simulations, the average space of forest dislocation remains fixed

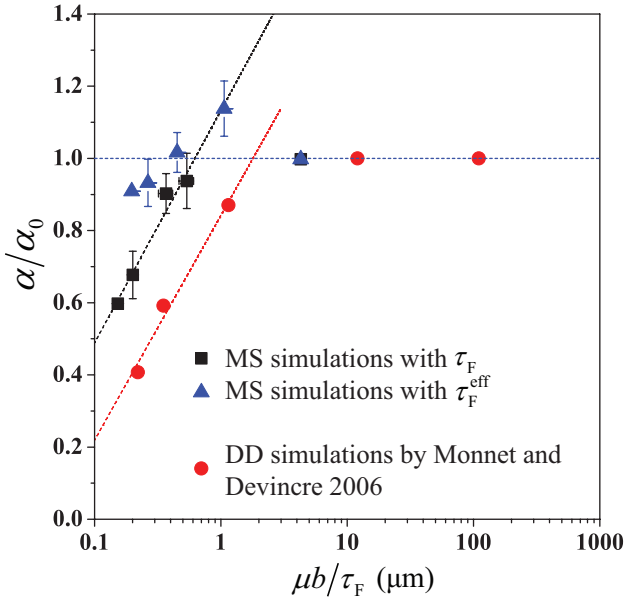

Figure 4.7: Variation of the normalized forest hardening coefficient α for LC junctions with the friction stress in reduced unit $\mu b/\tau_F$ at log scale measured from atomistic simulations and DD simulations. Mg concentration is $c = 0.05$ for the MS simulations. Dash lines show schematically the basic scaling.

in all solute concentrations and therefore the possibility of reduction of hardening coefficient α due to collective effect of alloy friction on the dislocation network is excluded.

Based on the discussion above, the observations and explanation in DD simulations can not interpret the measured reduction of hardening coefficient α due to solute friction in MS simulations. Note that the analysis above for the atomistic simulations ignores details of the local solute configuration and simply represents the solute effect by τ_S, which is the largest pinning strength that the dislocation will encounter as it glides through the solute field. Since τ_S only relates to certain local solutes configuration, unless the region is exactly in some *right* place, the solute-strengthened segment or the junction will be overloaded, resulting in an smaller measured overall strength compared to the additive amount. Therefore, when the mobile dislocation breaks through the LC locks, the mobile dislocation may encounter somewhat solute effect less than its absolute strength τ_S. We now verify this by checking the detailed

dislocation configuration during the destruction process. As shown in figure 4.5, the solutes friction reduces the bow-out curvature of the dislocation compared to the pure Al at same applied stress τ. As discussed in chapter 1, assuming the dislocation has a certain line tension Γ, the atomistic bow-out configurations can be fitted by a circle function with radius R and we can quantify the variation of bow-out curvature $1/R$ as a function of the applied stress τ as $(\tau - \tau_{\mathrm{F}})bR = \Gamma$. Figure 4.8 gives the fitting results at Mg concentration $c = 0.01$ and $c = 0.05$, also shown in the figure 4.8 is the results obtained from pure aluminum. Both in pure Al and Al/Mg system, the curvature $1/R$ nearly scales linearly with the applied stress τ, which verifies that the isotropic line tension model is appropriate in describing the evolution of the mobile dislocation structure. Linear fitting for pure Al results gives an line tension value $\Gamma = 0.43$ eV/Å at $\tau_{\mathrm{F}} = \tau_{\mathrm{P}}$, which is very close to the value $\Gamma = 0.47$ eV/Å calculated in last chapter 3. If we assume the solutes provide a strength on the dislocation which equal to the maximum solute strength τ_{S}, $1/R$ would equal zero when the applied stress τ is equal to total friction stress τ_{F}, which is $\tau = 51.3$ MPa at c=0.05 and $\tau = 19.2$ at c=0.01. However, non-zero curvature at $\tau = \tau_{\mathrm{F}}$ is clearly shown in the figure 4.8 and therefore the actual effective alloy friction $\tau_{\mathrm{F}}^{\mathrm{eff}}$ acting on the mobile dislocation must be smaller than the upper limit τ_{F} introduced before. Using the line tension value Γ obtained from pure aluminium calculation, we can obtain the effective total friction stresses $\tau_{\mathrm{F}}^{\mathrm{eff}}$ by fitting the bow-out curvature for different solute concentrations. From $\tau_{\mathrm{F}}^{\mathrm{eff}}$, an effective solute strength $\tau_{\mathrm{S}}^{\mathrm{eff}}$ acting on the dislocation when it breaks from the LC locks can be calculated from $\tau_{\mathrm{S}}^{\mathrm{eff}} = \tau_{\mathrm{F}}^{\mathrm{eff}} - \tau_{\mathrm{P}}$ and the values are listed in table 4.2. Then we use $\tau_{\mathrm{S}}^{\mathrm{eff}}$ to recheck the forest hardening coefficient, as shown figure 4.7. With the effective solute strength obtained directly from the atomistic configuration, the hardening coefficient α remains nearly a constant (close to α_0), clearly show that the solute strength has no influence on the dislocation junction strengthening at atomistic scale as the spacing between junctions is fixed.

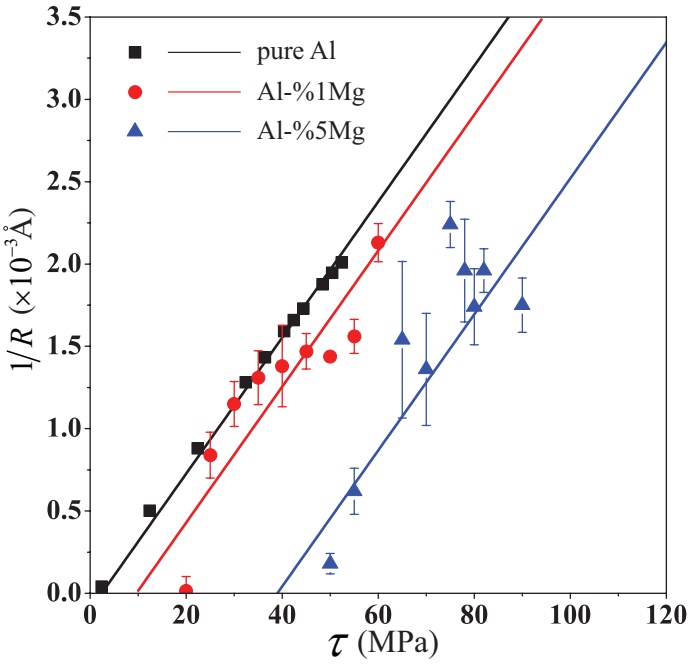

Figure 4.8: The bow-out curvature $1/R$ versus the applied stress τ at different solute concentration. Solid lines here are the linear fitting with the isotropic line tension model with $\Gamma = 0.43$ eV/Å. The zero bow-out curvature corresponds to the effective frication stress $\tau_{\mathrm{S}}^{\mathrm{eff}}$. Error bars in figures are the standard variation of using a circle function to fit the atomistic configurations obtained from the simulations

c_{Mg}	τ_{S} (MPa)	$\tau_{\mathrm{S}}^{\mathrm{eff}}$ (MPa)	$\tau_{\mathrm{S}}^{\mathrm{eff}} + \tau_{\mathrm{J}} + \tau_{\mathrm{P}}$ (MPa)	τ_{T}
0.01	16.5	6.98	62.0	66.3
0.02	25.3	20.1	75.1	73.3
0.05	48.3	36.2	91.2	85.3
0.08	64.8	49.6	104.6	97.5

Table 4.2: The effective solute strength $\tau_{\mathrm{S}}^{\mathrm{eff}}$ measured from the bow-out curvature of dislocation configurations at different solute concentration c.

Furthermore, except the case where $c = 0.01$, the calculated effective solute strength τ_S^{eff} are about 75% of the absolute solute strength τ_S. The deviation at low concentration attributes to the inaccuracy when using a circle function to fit the atomistic configuration. Recall that in previous calculations, we have shown that the model predication $\tau_{y0} = 243c^{2/3}$ differs from the solute strength τ_S by the ratio $243/351 = 70\%$, very close to the ratio $\tau_S^{\text{eff}}/\tau_S$ here. It suggests that the effective solute strength τ_S^{eff} is essentially the average of the solute contribution which the mobile dislocation will encounter as it breaks through the LC locks. And it better describes the solute effect on the forest hardening rather than the solute strength τ_S. Knowing that the effective solute strength τ_S^{eff} is essential the solute strengthening predicted by the analytical model, we now try to use model prediction τ_{y0} to check the linear summation rule implied by the constancy of α, such that the error introduced by the numerical procedure of evaulating τ_S^{eff} is excluded. The prediction of linear summation $\tau_T = \tau_{y0} + \tau_J + \tau_P$ is plotted in figure 4.9 and compared with the numerical results. Clearly, the liner summation gives reasonably well prediction of the total strength for the system where solute hardening and forest hardening operate simultaneously. The linear summation predictions using τ_S^{eff} are also listed in table 4.2 and the predication are still close to the total strength τ_T.

4.4 Summary

Based on recent development of atomistic study on the individual strengthening mechanism for FCC metals, we performed in this chapter the Molecular Static simulations of dislocation motion strengthened by both Mg solute atoms and forest dislocations in Al/Mg metal alloys. The numerical results obtained at atomistic scale show noticeable difference with previous mesoscale 3D DD simulations and continuum analysis. For the dilute solute concentration $c < 0.1$, the discrete distributed solute atoms will not introduce significant bow-out geometry on the dislocation arms

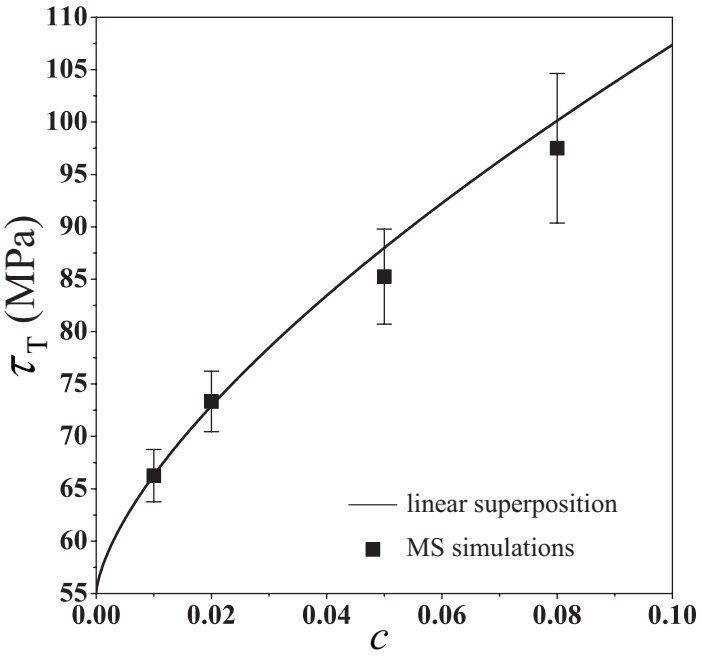

Figure 4.9: The prediction of the linear superposition rule $\tau_{\mathrm{T}} = \tau_{\mathrm{y0}} + \tau_{\mathrm{J}} + \tau_{\mathrm{P}}$ compared with MS simulation results.

that interact to form LC junctions. Therefore, the initial junction length at zero load will remain constant under different solute concentration. Consequently, the reduction of strength due to initial junction reduction is then excluded at atomistic scale. When considering the solute effect on the junction strength, our simulations show that rather than the absolute friction strength τ_{S} of solute atoms, the solute effect on the dislocation/junction locks should rather be defined by an effective solute strength $\tau_{\mathrm{S}}^{\mathrm{eff}}$ which the mobile dislocation will experience at it bows out to break through the junction structures. The effective friction stress $\tau_{\mathrm{S}}^{\mathrm{eff}}$ can be obtained from atomistic dislocation configurations and our calculations show that values of $\tau_{\mathrm{S}}^{\mathrm{eff}}$ agree well with the previous developed Labusch-type model prediction, confirming that $\tau_{\mathrm{S}}^{\mathrm{eff}}$ is essentially the average of the solute contribution to the dislocation-junction. Using the solute strengthening model prediction and the calculated junction strength, we prove that the linear summation is valid to describe the overall strength due to combined solute and forest hardening, which leads to a constant forest hardening

coefficient, given the space between dislocation-junction remaining fixed.

Chapter 5

Thermally-activated plastic flow in the presence of multiple obstacle types

5.1 Introduction

Previous chapters all focus on the hardening behavior with multiple strengthening mechanism operating simultaneously at zero temperature and have confirmed that the linear additivity is valid for certain cases both at continuum and atomistic scale. As mentioned in chapter 1 however, the thermal fluctuation at finite temperature provides another possible unpinning mechanism for a dislocation blocked by strengthening obstacles and the "flow stress" is therefore a function of strain rate $\dot{\varepsilon}$ and temperature T.

The topic of strengthening at finite temperature under a combination of multiple strengthening mechanisms is interesting but only a few investigations on this subject were reported in literature. As discussed in chapter 1, the thermally-activated flow in the presence of multiple strengthening mechanisms remains poorly understood and the explicit form of the overall flow stress versus strain rate and temperature

requires further development. Furthermore, simulations and theory have focused on point-pinning obstacles model, which neglects any influence of the interaction length between the dislocation and obstacles. However, the point-pinning assumption has to be treated with care since previous simulations have shown that, at zero temperature , the interaction width of the obstacles affects the way in which the dislocation samples the field of obstacles during glide, and thus affects the shear resistance of obstacles [112, 99, 113]. And atomistic simulations in last chapter clearly showed that the formed junction length is actually comparable to the Labusch length of solute strengthening and therefore for obstacles such as forest dislocation having high zero-stress activation energy and moderate strength, the physical obstacle interaction length scale (in the case of forest, the junction length) may not be negligible compared to the spacing of dispersed solute-type obstacles, calling into question the applicability of the point-pinning obstacle model for multiple obstacle types. The full atomistic details for this problem is desirable but due to the computational cost, the high value of strain rate $\dot{\varepsilon}$ place restrictions on the MD simulations of thermally activated process. Typical MD simulations have used $\dot{\varepsilon}$ in the range of $10^6 \sim 10^8$ s^{-1}, more than 10 order of magnitude larger than the typical strain rate of 10^{-4} s^{-1} applied to macroscopic tensile specimens in laboratory tests. The fundamental thermal activation frequency ν_0 is usually 10^7 ms^{-1}, resulting in the fact that the time which a dislocation can spend in contact with an obstacle is more than 10 order of magnitude larger than the MD ability and the probability of a thermally activated process occurring is not accessible in MD simulations.

To address the above issues, we focus in this chapter on thermally-activated flow in the case where the zero-temperature flow stress is known to be additive from chapter 1, and consider both point and extended obstacle models for the forest obstacles. We compute, via simulation, the effective activation energy for dislocation escape across the field of combined obstacles types, and develop an analytical model for thermally-activated flow stress based on numerical simulations. We show that the

linear additivity of flow stress at finite temperature is valid only when all strengthening obstacles can be treated as point-like obstacles. Obstacles with finite interaction length and associated high activation energy result in a non-additive overall flow stress at finite temperature even while linear additivity holds at $T = 0$. Our simulations show that at low stresses, the high-density "solute" obstacles provide a thermal backstress $\tau_{\rm b}$ acting on the dislocation, influencing the thermal activation over the extended "forest" obstacles. An analytical model for the overall activation energy $\Delta G(\tau, T)$ is then proposed based on the simulations and shown to agree well with simulations for a wide range of obstacle properties.

5.2 Simulation models for thermally-activated flow

In this section, we describe the algorithms used to simulate the thermal motion of a dislocation line across a slip plane along which two different types of obstacles are present. The dislocation line is modeled as a flexible string with isotropic line tension $\Gamma = 0.5\mu b^2$, where μ is the shear modulus and b is the magnitude of the Burgers vector. An initial dislocation of length L will glide in a plane that contains a random array of point obstacles representing the weak solute 's' obstacles with density $1/d_{\rm s}^2$, where $d_{\rm s}$ is the average space between 's' obstacles. The overall simulation cell is a square of size $L \times L$ so that the number of 's' obstacles $N_{\rm s}$ satisfies $L = d_{\rm s}\sqrt{N_{\rm s}}$. In all cases, we maintain $N_{\rm s} \geq 40000$, a size sufficient to exclude finite-size effect in the simulations [78]. A single forest obstacle of type 'f' is positioned at the center of the glide plane. Periodic boundary conditions are applied on the lateral boundary of the square simulation cells so that the 'f' obstacles are effectively periodic with space $d_{\rm f} = L$.

For thermal activation, we consider a typical case as illustrated in figure 5.1(a), where an obstacle interacts with the dislocation over a finite length w. The energy of the dislocation-obstacle interaction as a function of the distance y measured along

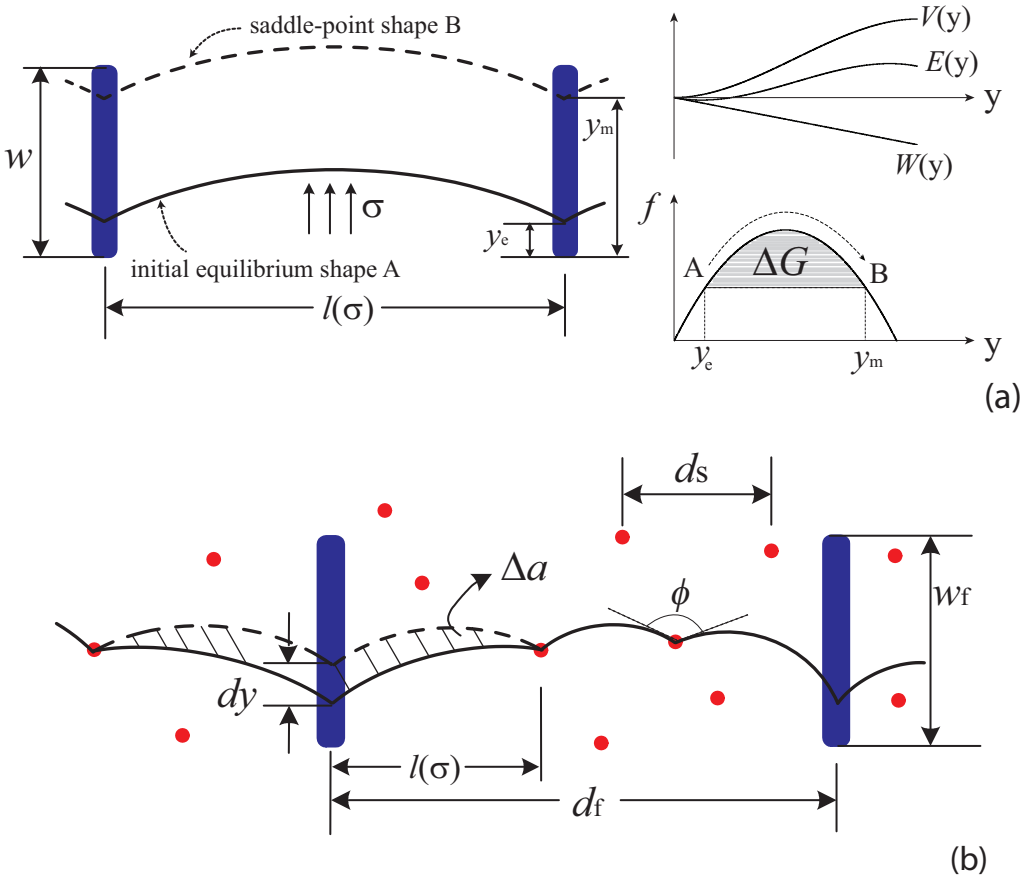

Figure 5.1: (a) Schematic of thermal activation for a dislocation bypassing obstacles with finite interaction length w; (b) Schematic of the algorithm used in the extended obstacle model (see text). Blue bars: extended obstacles; red dots: point obstacles; black lines: mobile dislocation

the direction of dislocation penetration into the obstacle can be expressed in terms of the zero-stress activation barrier ΔG^0 and the interaction length w. Several energy profiles for dislocation-obstacle interaction have been proposed in former studies and summarized in references [4, 17]. Here we introduced a third-order polynomial, which is simple but captures the essential physics [50, 59, 80]:

$$V(y) = \Delta G^0 \left(3\Big(\frac{y}{w}\Big)^2 - 2\Big(\frac{y}{w}\Big)^3 \right) \tag{5.1}$$

and present an analysis along the lines of Kocks et al. [50]. Accordingly, the resisting force on the dislocation can be expressed as

$$f\,(y) = \frac{\partial V}{\partial y} = \frac{6\Delta G^0}{w} \left(\Big(\frac{y}{w}\Big) - \Big(\frac{y}{w}\Big)^2 \right) = 4f^{\mathrm{c}} \left(\Big(\frac{y}{w}\Big) - \Big(\frac{y}{w}\Big)^2 \right) \tag{5.2}$$

where $f^{\mathrm{c}} = 3\Delta G^0/(2w)$ is the maximum resisting force of the obstacle. Under an applied stress τ, the dislocation will progress through the obstacle to an equilibrium distance y_{e}, with a force $f = \tau b l(\tau)$ exerted on the obstacle where $l(\tau)$ is the characteristic spacing of obstacles on the dislocation line, as shown in figure 5.1(a). At the same force f, i.e. the same τ, there is also unstable equilibrium position y_{m}. The energy barrier that must be overcome to reach the unstable (saddle-point) configuration is

$$\Delta G = \Delta V - \Delta W \tag{5.3}$$

where ΔV is the interaction energy difference from y_{e} to y_{m} and ΔW is the work done by τ during the activation process, which are given by

$$\begin{aligned} \Delta V &= V\,(y_{\mathrm{m}}) - V\,(y_{\mathrm{e}}) \\ \Delta W &= f\,(y_{\mathrm{m}} - y_{\mathrm{e}}) = \tau b l\,(\tau)\,(y_{\mathrm{m}} - y_{\mathrm{e}}) \end{aligned} \tag{5.4}$$

y_{e} and y_{m} can be obtained by solving $\mathrm{d}E/\mathrm{d}y = 0$ where $E(y) = V(y) - W(y)$. Substituting solved y_{e} and y_{m} into equations (5.3) and (5.4) gives the activation

energy

$$\Delta G = \Delta G^0 \left(1 - \frac{f}{f^{\mathrm{c}}}\right)^{3/2} \tag{5.5}$$

The stress dependence of ΔG can be related to equation (5.5) for two cases. In the Friedel limit [31] for the randomly distributed weak obstacles, $l(\tau) \sim \tau^{-1/3}$ and $f \sim \tau^{2/3}$ give

$$\Delta G = \Delta G^0 \left(1 - \left(\frac{\tau}{\hat{\tau}}\right)^{2/3}\right)^{3/2} \tag{5.6}$$

where $\hat{\tau}$ is the flow stress at zero temperature. For a linear array of obstacles, $f \sim \tau$ and thus ΔG follows

$$\Delta G = \Delta G^0 \left(1 - \frac{\tau}{\hat{\tau}}\right)^{3/2} \tag{5.7}$$

Based on the derivation above, each set of obstacles is now characterized by three parameters: the interaction length w; the zero-stress activation barrier ΔG^0; and the average space d which is related to the distance l. As shown in figure 5.1(b), at each pinning obstacle the two adjacent pinned dislocation segments define an angle ϕ and exert a force $f = \mu b^2 \cos(\phi/2)$ on the obstacle. The critical breaking angle ϕ^{c}, at which point the force on the obstacle reaches the maximum resisting force, is thus related to the obstacle resistance f^{c} and consequently gives $w = 3\Delta G/(4\Gamma \cos(\phi^{\mathrm{c}}/2))$. Therefore, in simulations, ϕ^{c}, d, and ΔG^0 are used to define the different obstacles types, i.e. the set $\{d_{\mathrm{s}}, \phi^{\mathrm{c}}_{\mathrm{s}}, \Delta G^0_{\mathrm{s}}\}$ defines the properties of the 's'obstacles and the set $\{d_{\mathrm{f}}, \phi^{\mathrm{c}}_{\mathrm{f}}, \Delta G^0_{\mathrm{f}}\}$ for 'f' obstacles.

The algorithm developed in chapter 2 for athermal simulations was modified to implement thermally-activated dislocation motion. Briefly, a single dislocation is initially put at the bottom of the glide plane and its motion is described by a succession of incremental changes in the position of individual segment as the pinning obstacles are overcome. For athermal simulations ($T = 0$), and to start thermally-activated simulations, in any given dislocation configuration each segment will bow out until it (i) reaches the unstable half-circle configuration, where the bowing out radius of the segment equals one-half the distance between its pinning obstacles;

(ii) meets a new obstacle; or (iii) breaks at a pinning point at which the force has exceeded f^{c}. The stresses required for each of the three events are computed for all segments along the line, and the event and segment requiring the minimum stress among all events and all segments are selected. If this minimum stress is below the desired applied stress, then the dislocation is advanced to the next configuration based on the chosen event. If the minimum stress over all events is larger than the desired applied stress, then the dislocation is in a static equilibrium configuration and thermal activation is required for the dislocation to move further.

For thermally-activated motion starting from a static equilibrium configuration, a kinetic Monte Carlo (kMC) procedure is introduced. Previous simulations [30, 35, 85, 109] normally ignored the details of the obstacle structure and directly implemented equation (5.5) to calculate the activation energy for a dislocation passing any pinning obstacle. We refer to this type of simulation as a 'Point-Pinning' simulation (PP simulation). In the PP simulation, at each static equilibrium configuration, the activation energy ΔG_i for the i^{th} pinning obstacle is computed from the force f_i via equation (5.5). The probability for overcoming the i^{th} obstacle is computed as $p_i = \exp\left(-\frac{\Delta G_i}{k_B T}\right)$, where k_B is the Boltzmann's constant. The normalized cumulative probability for the i^{th} obstacle r_i is then calculated as $\sum_{j=1}^{i} p_j / \sum_{j=1}^{M} p_j$, where M is the total number of obstacles that currently pin the dislocation line. A random number $R \in (0, 1)$ with uniform distribution is then chosen and the event i that satisfies $r_{i-1} < R < r_i$ is chosen to advance the dislocation to a new configuration. The time required to accomplish this thermally-activated step is $\Delta t = \left(\nu_0 \sum_{j=1}^{M} p_j\right)^{-1}$, where ν_0 is the fundamental "attempt" frequency [4]. The new dislocation configuration is then evaluated for any athermal event and, if any, is advanced to next static equilibrium configuration. The output from the PP simulation is the total time required for the dislocation to glide across the slip plane. Since the time spent in dislocation glide in between static equilibrium configurations is very short compared to the waiting time for each thermal activation event, the total time here is defined as the sum of

the times consumed at each thermal activation event. An average strain rate $\dot{\varepsilon}$ is obtained from the total time and the overall activation energy can be computed from $\dot{\varepsilon}$ using the usual Arrhenius-type rate equation

$$\dot{\varepsilon} = \dot{\varepsilon}_0 \exp\left(-\frac{\Delta G}{k_B T}\right) \tag{5.8}$$

where $\dot{\varepsilon}_0$ is the reference strain rate and related to the fundamental "attempt" frequency as $\dot{\varepsilon}_0 \sim \nu_0$ [4, 50]. Inverting equation (5.8), a thermally activate process occurring at strain rate $\dot{\varepsilon}$ and temperature T must have an activation barrier

$$\Delta G = k_B T \ln \frac{\dot{\varepsilon}_0}{\dot{\varepsilon}} \tag{5.9}$$

The point-pinning limit ignores the influence of the interaction width w, that is, it assumes that $w \ll d$ and thus w does not come into the consideration. This assumption might be applicable for distributed solute atoms or small precipitates [4, 99] but its applicability to forest strengthening is questionable. For forest dislocations, there is a moderate critical force but a large zero-stress activation energy [28], leading to a large interaction length w_f. In fact, the simulation in chapter 4 and other simple models of forest junction formation clearly show that the junction length scales with the forest space itself [24, 95]. Most importantly for the present work is the recognition that when both solute and forest mechanisms act together, treatment of the forests as point obstacle would also require $w_\mathrm{f} \ll d_\mathrm{s}$, which is unlikely to be valid. Therefore, the use of non-point-pinning model seems desirable, and perhaps essential, for the treatment of thermal activation in the presence of both solutes and forests.

We have thus developed an 'Extended-Obstacle' simulation (EO simulation) that uses the kMC-type algorithm schematically shown in figure 5.1(b) and described as follows. At an applied stress τ, the dislocation is pinned by an extended 'f' obstacle with penetration distance y and also pinned by point-like 's' obstacles nearby. We

then analyze a possible fluctuation of the dislocation position at the 'f' obstacle by a small distance dy. The energy change ΔE associated with this fluctuation is composed of the interaction energy change, $\Delta V = V(y + \mathrm{d}y) - V(y)$, the work done by τ as the dislocation glides between the surrounding pinning sites through some area Δa, $\Delta W = \tau b \Delta a$, and the change in line energy due to the length change of the dislocation segments, ΔE_{line}. The activation energy for this possible fluctuation is then $\Delta G = \Delta E = \Delta V + \Delta E_{\text{line}} - \Delta W$ and the probability of this event in kMC algorithm is obtained from ΔG. If this event is selected, the penetration of the dislocation into the 'f' obstacle is advanced to $y + \mathrm{d}y$. Series of tests for different values of dy showed that $\mathrm{d}y \leq 10^{-4} d_{\text{f}}$ is sufficient for the convergence and accuracy of the overall results. Due to the computational cost, solute obstacles here are still treated as point-pinning obstacles. For the EO simulation, we track the total energy of the dislocation during its evolution through the computed thermally activated path and take the highest energy barrier encountered by the dislocation as the overall activation energy.

In the results shown in the next section, all lengths are normalized as $l^* = l/(d_{\text{s}})$, all forces are normalized as $f^* = f/(\mu b^2)$, and all energies are normalized as $\Delta G^* = \Delta G/\Delta G^0_{\text{s}}$. Simulations at two different temperature $T = 78$ and 312 K are carried out, corresponding to the normalized thermal energies $k_B T/\Delta G^0_{\text{s}} = 6.7 \times 10^{-3}$ and 26.8×10^{-3} for $\Delta G^0_{\text{s}} = 1$ eV. All stresses are normalized as $\tau^* = \tau d_{\text{s}}/(\mu b)$. Note that $\hat{\tau}^*_{\text{s}} = 0.9 \cos^{3/2}(\phi^{\text{c}}_{\text{s}}/2)$ [31, 78] and $\hat{\tau}^*_{\text{f}} = \frac{d_{\text{s}}}{d_{\text{f}}} \cos(\phi^{\text{c}}_{\text{f}}/2)$ since the 'f' obstacles are in a periodic linear array. We consider a system with a large density difference between 's' and 'f' obstacles ($d_{\text{f}} \gg d_{\text{s}}$) such that the linear additivity of the zero-temperature flow stress $\hat{\tau}^* = \hat{\tau}^*_{\text{s}} + \hat{\tau}^*_{\text{f}}$ is ensured which has been verified in chapter 2. In the PP simulation, the time is normalized by ν_0 as $t^* = \nu_0 t$. In the EO simulations, the shear modulus μ and the magnitude of the Burgers vector b are $\mu = 26$ GPa and $b = 0.286$ nm, corresponding to aluminum alloys. Simulations with different $\phi^{\text{c}}_{\text{f}}$ and $\phi^{\text{c}}_{\text{s}}$ are investigated. The flow stress is the input applied stress τ^*, and we will also

refer to a normalized flow stress $\eta = \tau^*/\hat{\tau}^*$.

The results from different simulation models are interpreted in terms of the normalized overall activation energy ΔG^* as a function of the normalized applied flow stress η at temperature T. As an example of the direct output of the EO simulation, figure 5.2 shows the energy variation as the dislocation advances by thermally activated steps when interacting with the extended 'f' obstacle and point-like 's' obstacles, and the highest energy barrier at different η is shown. Note that we are interested in the presence of both forest and solute obstacles in the simulation, we have linear additivity at zero T, and we focus on the region where the normalized flow stress $\eta \geq \hat{\tau}_\mathrm{s}/\left(\hat{\tau}_\mathrm{s} + \hat{\tau}_\mathrm{f}\right)$ so that the forests must play a role in restraining the dislocation motion. In all cases, a large number of statistical replicas using the same obstacle parameters but spatial differences of the point-pinning solute obstacles were generated, and the results quoted are the average over all these realizations, with error bars indicating various among the set of replicas.

5.3 Results and discussions

5.3.1 Single obstacle results

Before starting thermal activation behavior in the system with mixed-type obstacle strengthening, plastic flow in the presence of single obstacle type at finite temperature is investigated to validate the basic models and simulation methods. We have shown that for random point obstacles the activation energy should follow equation (5.6) while for periodic obstacles the activation energy should satisfy equation (5.7).

Thermally-activated motion of the dislocation in presence of 's' obstacles alone is firstly simulated via the PP simulation. Figure 5.3(a) shows the analytical model of equation (5.6) and the numerical results for the activation energy at different flow stress, and excellent agreement is achieved. This confirms that the Friedel limit is still valid at finite temperature for random positioned point-pinning obstacles.

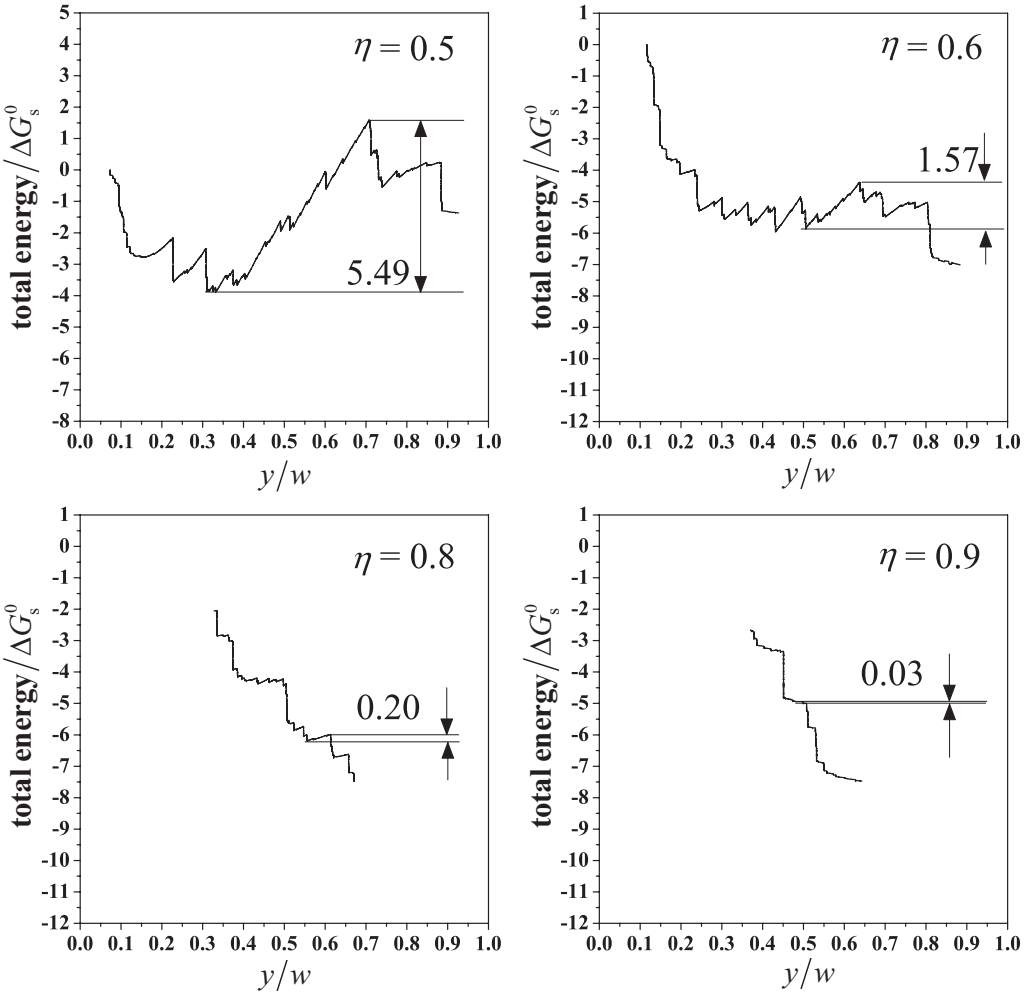

Figure 5.2: Normalized total energy evolution versus dislocation position within the forest obstacle during the thermally-activated motion of dislocation glide through the mixed-type obstacles for different applied stresses, with the energy barrier indicated. Obstacle properties $\hat{\tau}_{\mathrm{s}}^{*} = 8.5 \times 10^{-4}$, $\hat{\tau}_{\mathrm{f}}^{*} = 15 \times 10^{-4}$ and $\Delta G_{\mathrm{f}}^{0*} = 30 (w_{\mathrm{f}}^{*} = 11.3)$

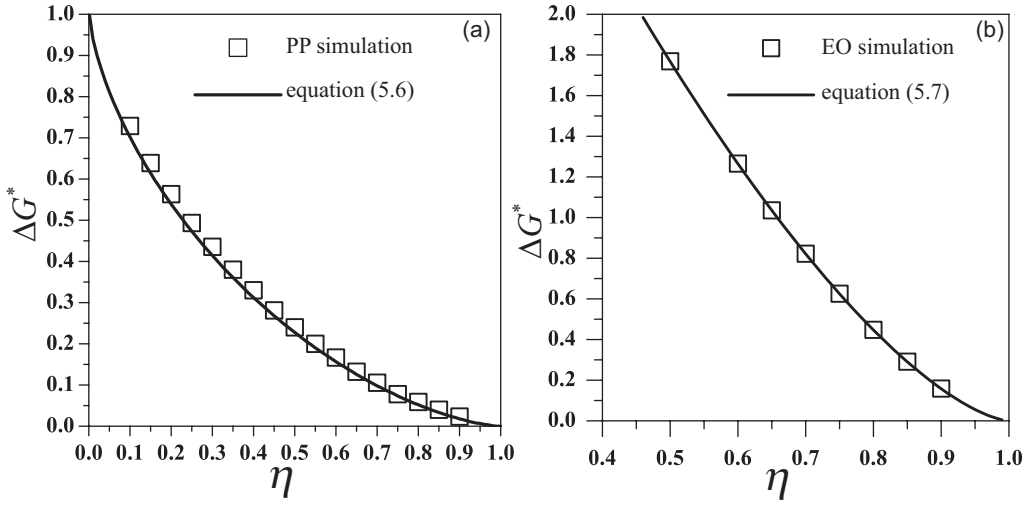

Figure 5.3: Activation energy versus normalized flow stress by a single obstacle type. (a) Solute obstacles only, with $\hat{\tau}_s^* = 8.5 \times 10^{-4}$; (b) Extended forest obstacles only, with $\hat{\tau}_f^* = 25 \times 10^{-4}$ and $\Delta G_f^{0*} = 5$

Therefore, in following analysis, equation (5.6) is used to characterize the finite-temperature flow behavior of the solute strengthening system. The EO simulation is then used to simulate thermal activation over the extended forest obstacles in the absence of solutes. The results are shown in figure 5.3(b) and confirm that equation (5.7) is quantitatively accurate for a linear array of forest obstacles, validating the EO simulation method implemented. Therefore, we will use equation (5.7) to characterize the thermal activation of dislocations past the extended forest obstacles.

5.3.2 Mixture of point obstacles

Based on the tests above, the two numerical models can now be used to simulate the plastic flow in the presence of two different types of obstacles. The overall activation energy for dislocation glide through fields with two types of *point-like* obstacles were computed by the PP simulation for different zero-stress forest activation energies ΔG_f^{0*} ranging from 1 to 10. Figure 5.4 shows the total activation energy ΔG^* as a function of the flow stress η. The dislocation configuration during the thermal motion is shown in figure 5.5, and is consistent with the physical process proposed

by Kocks et al. [50]. The dislocation line initially reaches a static equilibrium configuration, pinned by both solute obstacles and forest obstacles. Since the rate for the dislocation to thermally bypass the forest is much lower than that of the solutes, the dislocation continues to bow-out by thermal de-pinning from the solutes. The overall curvature of the dislocation line increases, leading to an increase of the force acting on the forest, and hence an increase of the escape rate past the forest. At the critical configuration, the rate of thermal activation over the forest becomes equal or at least comparable to that of the solutes, and thermal activation for dislocation de-pinning from the forest becomes favorable. Once the dislocation escapes from the forest obstacles, the backstress due to the forests is lost and the dislocation moves rapidly through the solute field until it encounters another forest obstacle. Since the activation rate is exponential in the activation energy, the overall time for moving past the forests is dominated by the time spent very near the final configuration just before thermal activation on the forests. The configurational evolution can be quantified by examining the force acting on the forest obstacle during the thermal activation. Figure 5.5 shows the variation of the force acting on the forest obstacle, f_{f}^{*}, during the thermal activation in the PP simulations, for one random solute configuration.

To make analytical progress, we start with equation (5.6) and (5.7) for individual strengthening mechanism and assume that the mechanism 's' provides a temperature- and rate-dependent friction stress $\Delta\tau(\dot{\varepsilon}, T)$ acting on the 'f' mechanism. The total stress acting on the dislocation is then partitioned between the two different obstacles resisting the dislocation motion, so that the stress on mechanism 's' operating in equation (5.6) is $\tau(\dot{\varepsilon}, T) - (\hat{\tau}_{\mathrm{f}} - \Delta\tau(\dot{\varepsilon}, T))$ and the stress on mechanism 'f' obstacle

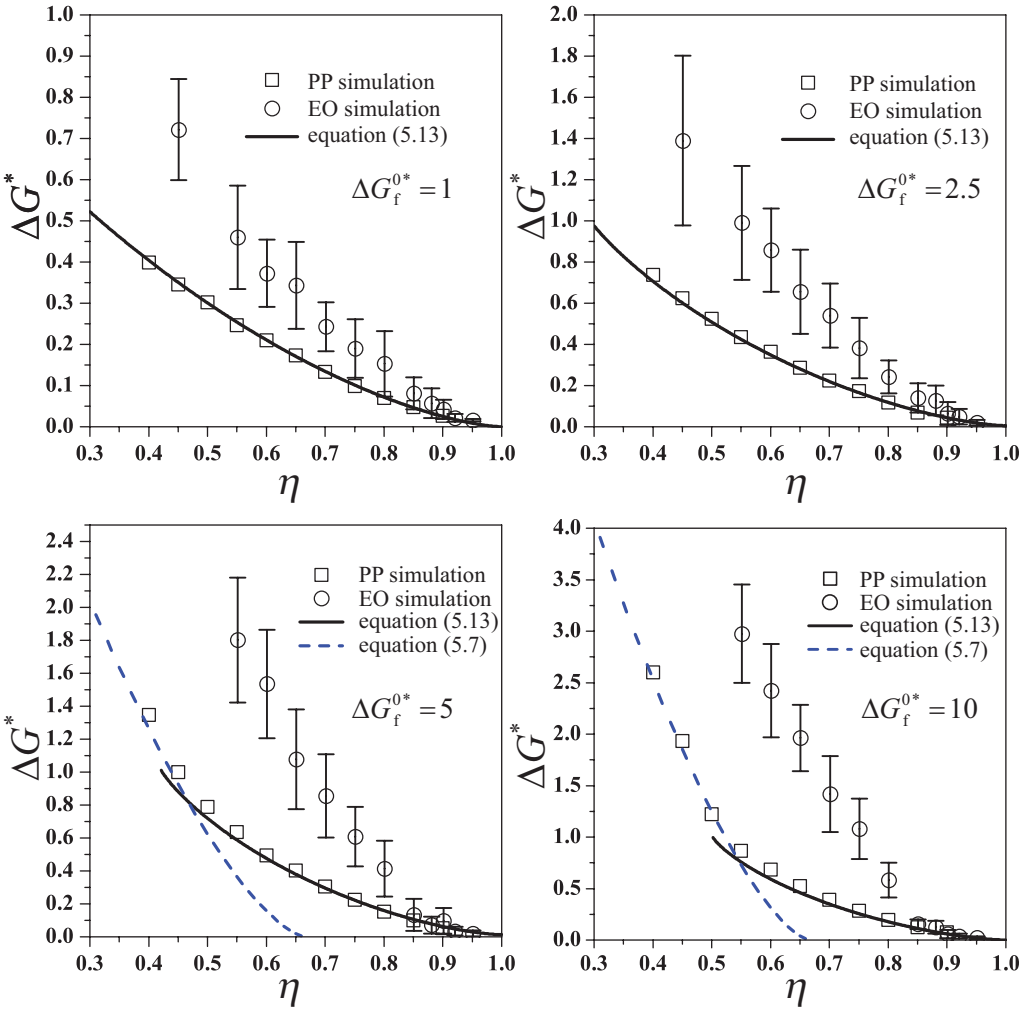

Figure 5.4: Overall activation energy ΔG^* versus normalized flow stress η, for different values of the zero-stress activation energy ΔG_f^{0*}, for $\hat{\tau}_s^* = 8.5 \times 10^{-4}$ and $\hat{\tau}_f^* = 15 \times 10^{-4}$. Symbols: simulation data; black solid lines: equation (5.13) (Kocks model); blue dashed lines: equation (5.7)

operating in equation (5.7) is $\hat{\tau}_{\mathrm{f}} - \Delta\tau(\dot{\varepsilon}, T)$. Thus we have

$$\begin{aligned} \Delta G_{\mathrm{s}} &= \Delta G_{\mathrm{s}}^{0} \left(1 - \left(\frac{\tau - (\hat{\tau}_{\mathrm{f}} - \Delta\tau(\dot{\varepsilon}, T))}{\hat{\tau}_{\mathrm{s}}} \right)^{2/3} \right)^{3/2} \\ \Delta G_{\mathrm{f}} &= \Delta G_{\mathrm{f}}^{0} \left(1 - \frac{\hat{\tau}_{\mathrm{f}} - \Delta\tau(\dot{\varepsilon}, T)}{\hat{\tau}_{\mathrm{f}}} \right)^{3/2} \end{aligned} \tag{5.10}$$

At the flow stress, the rate of dislocation escape from both obstacle types are assumed equal[50], and so the activation energies must be equal to the overall activation energy for the entire process, i.e.

$$\Delta G(\tau, T) = \Delta G_{\mathrm{s}}(\tau, T) = \Delta G_{\mathrm{f}}(\tau, T) \tag{5.11}$$

$\Delta\tau$ can be solved by substituting equation (5.10) into equation (5.11). Substituting $\Delta\tau$ back into equation (5.10) and using equation (5.8) to relate to the strain rate leads, after some algebra, to the flow stress at temperature T and strain rate $\dot{\varepsilon}$

$$\begin{aligned} \tau(\dot{\varepsilon}, T) &= \left(1 - \left(\frac{k_B T}{\Delta G_{\mathrm{s}}^{0}} \ln \frac{\dot{\varepsilon}_0}{\dot{\varepsilon}} \right)^{2/3} \right)^{3/2} \hat{\tau}_{\mathrm{s}} + \left(1 - \left(\frac{k_B T}{\Delta G_{\mathrm{f}}^{0}} \ln \frac{\dot{\varepsilon}_0}{\dot{\varepsilon}} \right)^{2/3} \right) \hat{\tau}_{\mathrm{f}} \\ &= \tau_{\mathrm{s}}(\dot{\varepsilon}, T) + \tau_{\mathrm{f}}(\dot{\varepsilon}, T) \end{aligned} \tag{5.12}$$

(5.12) shows that the total flow stress $\tau(\dot{\varepsilon}, T)$ is the summation of the individual flow stresses $\tau_{\mathrm{f}}(\dot{\varepsilon}, T)$ and $\tau_{\mathrm{s}}(\dot{\varepsilon}, T)$ measured at same $\dot{\varepsilon}$ and T, i.e. the linear additivity of flow stresses postulated by Kocks et al.

To compare the above predication to the numerical results, the overall flow stress $\tau(\dot{\varepsilon}, T)$ from equation (5.12) is rewritten as a function of the overall activation energy ΔG as

$$\tau = \left(1 - \left(\frac{\Delta G}{\Delta G_{\mathrm{s}}^{0}} \right)^{2/3} \right)^{3/2} \hat{\tau}_{\mathrm{s}} + \left(1 - \left(\frac{\Delta G}{\Delta G_{\mathrm{f}}^{0}} \right)^{2/3} \right) \hat{\tau}_{\mathrm{f}}. \tag{5.13}$$

Equation (5.13) is compared with the numerical results obtained from the PP simulation in figure 5.4, and good agreement is found for a wide rage of obstacle properties.

The model of equation (5.12) and (5.13), which is hereafter referred to as the Kocks model, must fail when $\Delta G > \Delta G_{\rm s}^0$, which occurs at low flow stress η and large $\Delta G_{\rm f}^{0*} > 5$. Since the thermal activation rate is exponential in the activation energy, at high $\Delta G_{\rm f}^{0*} > 5$ the escape rate of the forest obstacles at low stress is so small compared to that of the solutes that the dislocation is pinned only by the forests, and with large activation energy. This is verified by comparing the numerical data in this low-stress regime with the prediction of equation (5.7), using the total applied stress $\tau = \eta\,(\hat{\tau}_{\rm s} + \hat{\tau}_{\rm f})$ acting only on the forests. As shown in figure 5.4, good prediction is achieved at low η and high $\Delta G_{\rm f}^0$, where the Kocks model fails.

We conclude that if all obstacles are point-like, then (i) at high flow stress and low forest activation energy, the total flow stress at finite temperature T and strain rate $\dot{\varepsilon}$ can be obtained by summing over all individual flow stresses measured at same T and $\dot{\varepsilon}$ and (ii) when $\Delta G_{\rm f}^0$ is high and the flow stress is low, the thermal activation is controlled by the forests alone, which can also be predicted by a point-based model. Simulations and models predictions for different combinations of $\hat{\tau}_{\rm f}$ and $\hat{\tau}_{\rm s}$ were also investigated for the point-pinning case, and found to be qualitatively very similar to the case shown in figure 5.4.

5.3.3 Mixture of extended forests and point solute obstacles

The simulation results for the overall activation energy obtained from the EO simulation are also shown in figure 5.4, to permit direct comparison between the PP simulation and EO simulation for exactly the same system parameters. The EO and PP simulations only agree at high flow stress, as shown in figure 5.6 for $\eta > 0.85$ where the Kocks model predictions (matching the PP simulations data not shown) captures the EO simulations well. At such high flow stresses η, the penetration distance into the extended 'f' obstacle is such that the activation length $y_{\rm m} - y_{\rm e} \sim 0.1 d_{\rm s}$ is small compared to the solute spacing. A point-pinning approximation for the forest obstacles is thus reasonable, and linear additivity of the flow stresses follows.

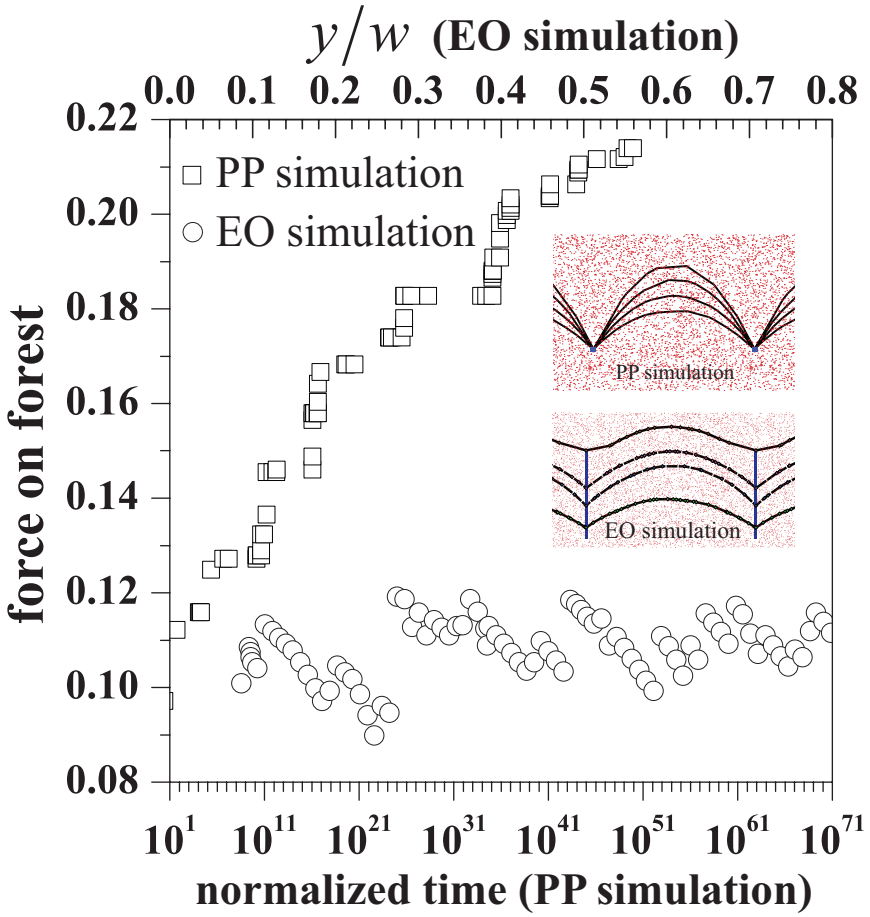

Figure 5.5: Force on the forest obstacles versus the normalized time in the PP simulation and versus the penetration distance of dislocation into the forest in the EO simulation, during the thermal motion of dislocation across the mixed-type obstacle field for one random solute configuration. Inset: evolution of dislocation configuration during thermal activation processes in the PP and EO simulations. Blue bars/dots: forest obstacles; red dots: point solute obstacles; black lines: dislocation. Shown for $\eta = 0.5$, $\Delta G_{\mathrm{f}}^{0*} = 5$, and $\hat{\tau}_{\mathrm{f}}^{*} = 15 \times 10^{-4}$

Therefore, it is not the total obstacle length w_f that determines whether the forest behaves as a point or extended obstacle, but rather the activation length $y_\mathrm{m} - y_\mathrm{e}$, which is stress dependent. Generally, $y_\mathrm{m} - y_\mathrm{e} \sim w_\mathrm{f}$ but at sufficiently high stress $y_\mathrm{m} - y_\mathrm{e}$ can be small enough so that the extended obstacle acts like a point obstacle. At lower flow stresses $\eta < 0.85$, the EO simulations yield values of ΔG^* that are much larger than obtained from the PP simulations or Kocks model, and the discrepancy increases as ΔG_f^{0*} increases, i.e. as w_f increases. In this regime, $y_\mathrm{m} - y_\mathrm{e} > d_\mathrm{s}$ and the point obstacle model fails, which is usually coincident with $w_\mathrm{f}/d_\mathrm{s} > 1$, except at very high stresses.

Figure 5.7 shows the EO simulation results and the predictions of the Kocks model at $\Delta G_\mathrm{f}^{0*} = 5$ for different values of the forest strengthening $\hat{\tau}_\mathrm{f}^*$ with fixed solute strengthening $\hat{\tau}_\mathrm{s}^*$. Unlike the Kocks model which predicts decreasing activation energy with decreasing forest strength, as shown in figure 5.6 and figure 5.7, the dependence of ΔG^* on the forest strengthening is negligible, aside its appearance in η at low flow stress level. And since a decreasing forest strength at fixed ΔG_f^{0*} implies an increasing w_f, the failure of the point-pinning model can again be associated with $w_\mathrm{f}/d_\mathrm{s} > 1$.

Examination of the dislocation configuration during the thermal activation process in the EO simulation reveals the key difference between PP and EO simulations. The lower inset in figure 5.5 shows how the dislocation thermally advances in the mixed-type obstacle field for one random solute configuration in the EO simulation. During the activation process, the dislocation gradually moves through the forest obstacle from y_e to the saddle point y_m while maintaining a nearly *constant curvature* during the activation process, corresponding to a *constant force* acting on the forest obstacle. This differs from the PP simulation (upper inset of figure 5.5), and is very similar to the behavior observed when the forest operates alone.

Based on the EO simulation results, we now develop an analytical model to predict the activation energy for extended forest obstacles operating together with

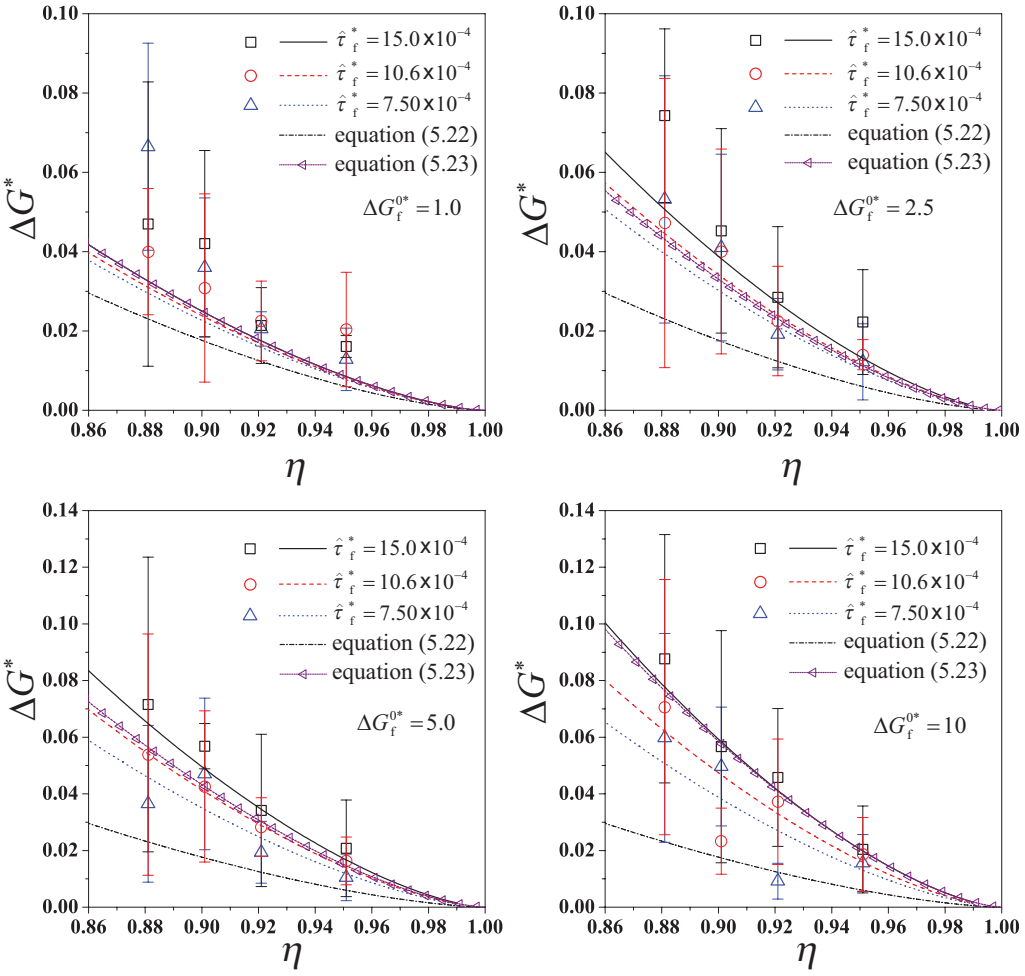

Figure 5.6: Overall activation energy versus normalized flow stress, at high flow stress levels, for $\hat{\tau}_s^* = 8.5 \times 10^{-4}$ and varying $\hat{\tau}_f^*$. Symbols: EO simulations; solid/dash/dot lines: predictions of the Kocks model, equation (5.13); dash-dot lines: predictions of the postulate of Curtin(2010) [21]; dot-triangle lines: predictions of the ad-hoc model, equation (5.23)

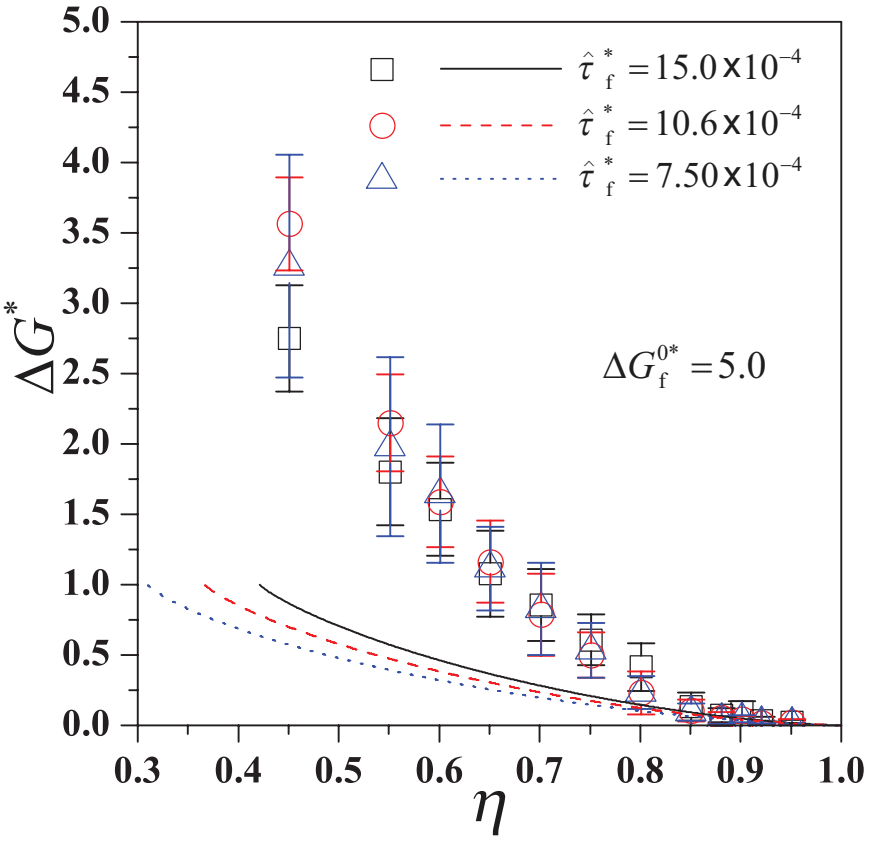

Figure 5.7: Normalized overall activation energy vs. applied load, for different forest stresses at fixed solute strength $\hat{\tau}_s^* = 8.5 \times 10^{-4}$. Symbols: EO simulations; lines: predictions of the Kocks model (equation (5.13))

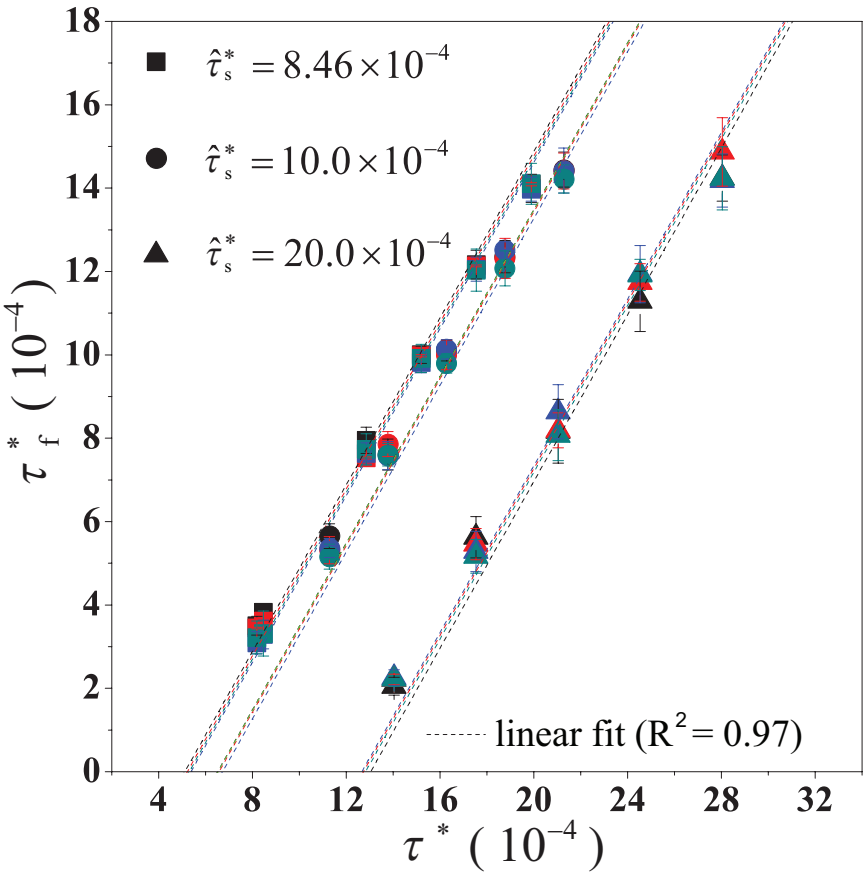

Figure 5.8: Average stress on extended forest obstacle during the thermally activation process versus the applied flow stess, for different forest energy barriers ΔG_f^* and solute strength $\hat{\tau}_s^*$ at fixed strength $\hat{\tau}_f^* = 15 \times 10^{-4}$. Symbol colors in the figure refer to different values of ΔG_f^*; black, $\Delta G_f^{0*} = 1$, red, $\Delta G_f^{0*} = 2.5$, blue, $\Delta G_f^{0*} = 5$, green, $\Delta G_f^{0*} = 10$

solutes. The observation of a fixed dislocation curvature during thermal activation in the EO simulation suggests that the stress acting on the extended forest, $\tau_{\mathrm{f}}(\dot{\varepsilon}, T)$, remains constant, on average, during the thermal activation process. From the EO simulations, we can explicitly compute the average force f_{f}^* acting on the forest obstacle during thermal activation using the simulated dislocation curvature, and then determine the stress acting on the forests as $\tau_{\mathrm{f}}^* = f_{\mathrm{f}}^*/d_{\mathrm{f}}^*$. Figure 5.8 shows the measured stress τ_{f}^* acting on the forest versus the flow stress $\tau^* = \eta(\hat{\tau}_{\mathrm{s}}^* + \hat{\tau}_{\mathrm{f}}^*)$ for a fixed $\hat{\tau}_{\mathrm{f}}^* = 15 \times 10^{-4}$ and varous $\hat{\tau}_{\mathrm{s}}^*$. The calculated values of τ_{f}^* are independent of the zero-stress activation energy $\Delta G_{\mathrm{f}}^{0*}$ and, more importantly, vary linearly with the flow stress τ^*. This suggests that there exists an effective backstress τ_{b}^* due to the solutes acting on the forests, so that $\tau_{\mathrm{f}}^* = \tau^* - \tau_{\mathrm{b}}^*$. The values of τ_{b}^* for different $\hat{\tau}_{\mathrm{s}}^*$, and for different temperatures, are listed in table 5.1. We note that the ratio $\tau_{\mathrm{b}}^*/\hat{\tau}_{\mathrm{s}}^*$, i.e. the backstress provided by the solutes relative to the zero-temperature solute strength, varies with the temperature T, reflecting that the thermal activation through the solute field in between the forests remains operative. Given the stress τ_{b}^* carried by the field of solutes at the flow stress $\tau(\dot{\varepsilon}, T)$, we can compute the activation energy for the solutes from equation (5.6) as

$$\Delta G_{\mathrm{s}} = \Delta G_{\mathrm{s}}^0 \left(1 - \left(\frac{\tau_{\mathrm{b}}}{\hat{\tau}_{\mathrm{s}}}\right)^{2/3}\right)^{3/2} \tag{5.14}$$

Furthermore, with $\tau_{\mathrm{f}}(\dot{\varepsilon}, T) = \tau(\dot{\varepsilon}, T) - \tau_{\mathrm{b}}(T)$, the activation energy for the forest obstacles follows from equation (5.7) as

$$\Delta G_{\mathrm{f}} = \Delta G_{\mathrm{f}}^0 \left(1 - \frac{\tau - \tau_{\mathrm{b}}}{\hat{\tau}_{\mathrm{f}}}\right)^{3/2} \tag{5.15}$$

Combining equation (5.14) and (5.15) yields the overall activation energy

$$\Delta G(\tau, T) = \Delta G_{\mathrm{f}}^0 \left(1 - \frac{\tau - \tau_{\mathrm{b}}}{\hat{\tau}_{\mathrm{f}}}\right)^{3/2} + \Delta G_{\mathrm{s}}^0 \left(1 - \left(\frac{\tau_{\mathrm{b}}}{\hat{\tau}_{\mathrm{s}}}\right)^{2/3}\right)^{3/2} \tag{5.16}$$

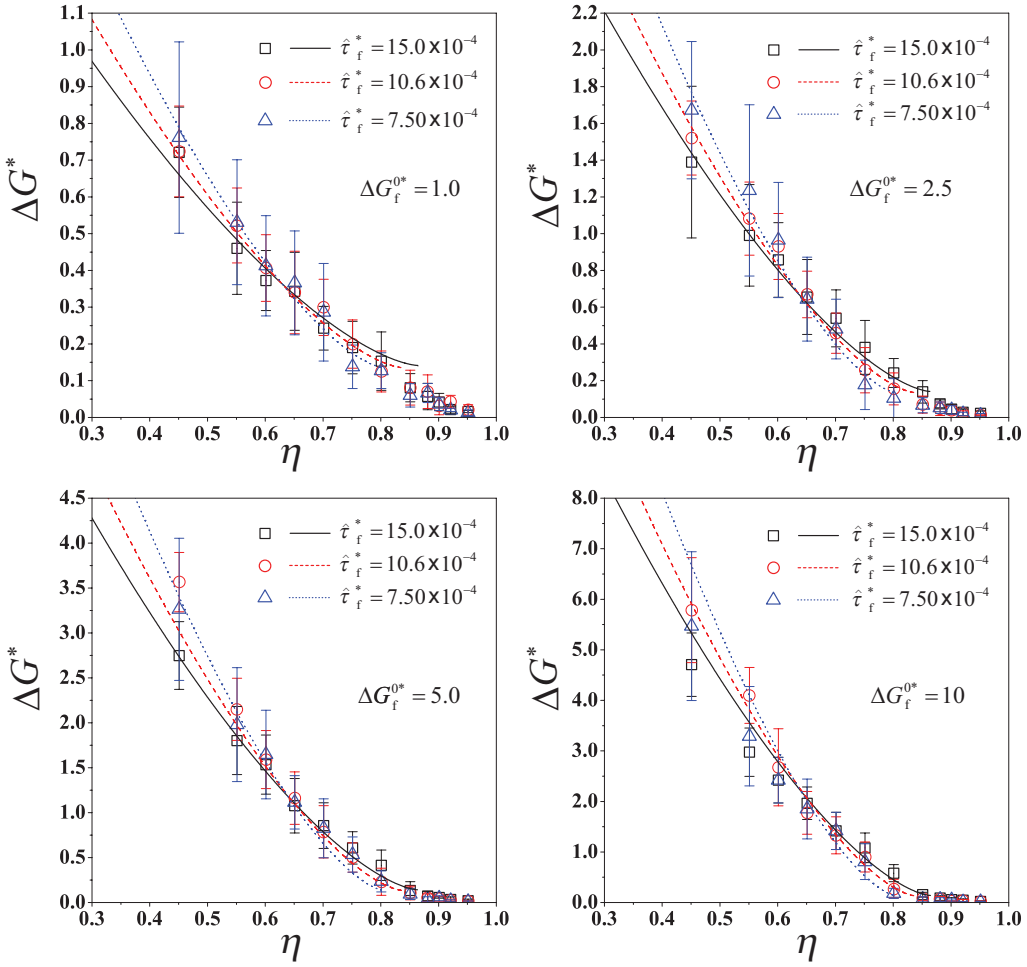

Figure 5.9: Variation of the overall activation energy with flow stress given $\hat{\tau}_s^* = 8.5 \times 10^{-4}$. Symbols: EO simulations; lines: prediction of equation (5.16)

where the temperature dependence is implicit through the dependence of τ_b on temperature. Note that equation (5.16) does not apply when $\tau > \tau_b + \hat{\tau}_f$, where linear additivity (the Kocks model) explains the results, as discussed above. Figure 5.9 shows the predicted value of ΔG^* using equation (5.16) in its range of validity; good agreement is found for all values of $\hat{\tau}_f^*$ and ΔG_f^{0*}. Similar agreement is found for other solutes strength $\hat{\tau}_s^*$ with the corresponding values of τ_b^* listed in table 5.1. Moreover, the predictions at two different temperatures agree well with the EO simulations, as shown in figure 5.10.

One key feature of our result is that the activation energy itself depends on tem-

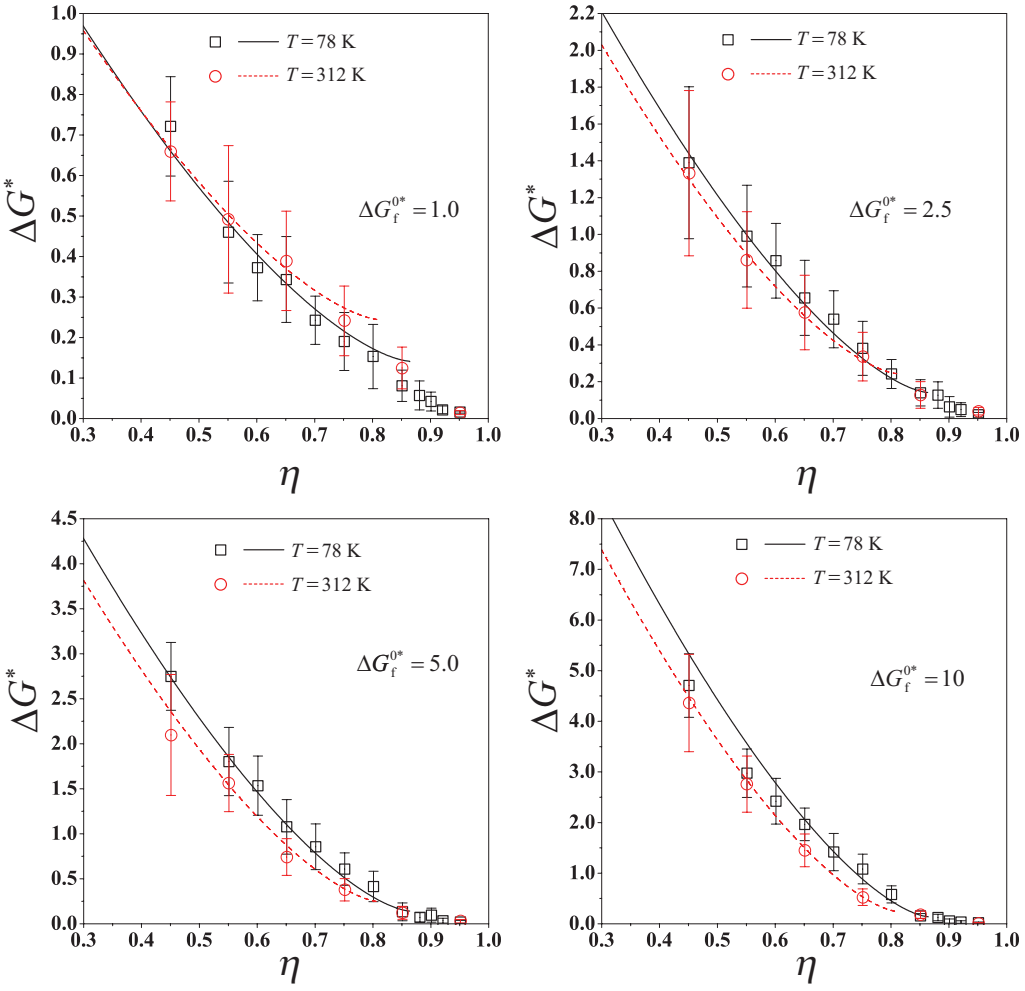

Figure 5.10: Variation of the activation energy with flow stress at two different temperature, given $\hat{\tau}_{\mathrm{s}}^{*} = 8.5 \times 10^{-4}$ and $\hat{\tau}_{\mathrm{f}}^{*} = 15 \times 10^{-4}$

T(K)	$\hat{\tau}_{\rm s}^*(\times 10^{-4})$	$\tau_{\rm b}^*(\times 10^{-4})$	$\tau_{\rm b}^*/\hat{\tau}_{\rm s}^*$
78	8.46	5.33	0.63
	10.00	6.59	0.65
	20.00	12.60	0.53
312	8.46	4.02	0.48

Table 5.1: The fitted values of the effective solute backstress $\tau_{\rm b}^*$, for different zero-temperature solute strengths $\hat{\tau}_{\rm s}^*$ and different temperatures T

perature in this forest-controlled regime. This is outside the standard modeling of thermally-activated processes, but arises because the phenomenon here is controlled by two intersecting thermally-activated processes affecting the motion of the dislocation line. The implication of equation (5.16) is then that strain rate and temperature are not interchangeable variable usually occurring only as the product $k_B T \ln(\dot{\varepsilon}_0/\dot{\varepsilon})$, as in equation (5.9).

The EO simulations clearly show that the finite interaction length between dislocation and the forest obstacle completely modifies the thermal activation process, as compared to the PP simulation, with the stress dependence of the activation barrier (equation (5.16)) controlled by the forests and with the solutes contributing a fixed increment to the activation barrier. We have no prediction for the measured values of the temperature-dependent effective solute backstress $\tau_{\rm b}$, but the analytic model of equation (5.16) otherwise explains the low stress regime very well. The high stress regime is adequately explained by the Kocks model (equation 5.13). The two models have different values of ΔG^* right at the "transition" stress of $\tau = \tau_{\rm b} + \hat{\tau}_{\rm f}$ and the slopes are notably different at this point — the transition from the high stress to low stress regime is thus not captured by the models here.

5.3.4 Discussion

The EO simulations confirm the influence of the finite interaction length $w_{\rm f}$ on the finite temperature flow stress in the presence of mixed-type obstacles when $w_{\rm f} \gg d_{\rm s}$. Equation (5.16), based on EO simulations, accounts for the finite interaction length

effect. For pure metals, $\hat{\tau}_{\rm s}$ and $\tau_{\rm b}$ are both equal to 0 and equation (5.16) yields equation (5.7) for the forests operating alone. Overall, our analysis suggests that for extended obstacles at high ΔG, the thermal activation is controlled by the extended forest obstacles while at low ΔG the thermal activation energy barrier follows the Kocks model. Experimentally, ΔG is related to the temperature and strain rate at which the experiments are conducted (see equation 5.9). In typical experiments, the temperature usually ranges from 78 K to room temperature ($\sim$ 300 K) and the strain rate from 10^{-5} to 0.1 $\rm s^{-1}$. For $\dot{\varepsilon}_0 \sim 10^5$ $\rm s^{-1}$, typical values of ΔG span from 0.1 eV to 0.6 eV. For $\Delta G_{\rm s}^0 = 1$ eV, as used in our EO simulations and typical of solute strengthening energetics [57] and $\Delta G_{\rm f}^0 \sim 5$ eV as derived for Cu [28] our results suggest that experiments over this range of temperatures span $\Delta G^* = 0.1$ to 0.6 and actually cross over between the two regimes described by equation (5.13) and (5.16).

To compare with general experimental observations, we now examine the activation area as predicted by the various models. For mixed point obstacles, the linear additivity Kocks model is known to lead to the linear additivity of the inverse activation area [23, 22, 50], so that

$$\frac{1}{\Delta a} = \frac{b}{k_B T} \frac{\partial \left(\tau_{\rm s}(\dot{\varepsilon}, T) + \tau_{\rm f}(\dot{\varepsilon}, T)\right)}{\partial \ln \dot{\varepsilon}}\Big|_T = \frac{1}{\Delta a_{\rm s}} + \frac{1}{\Delta a_{\rm f}} \tag{5.17}$$

where $\Delta a_{\rm s}$ and $\Delta a_{\rm f}$ are the activation area at T and $\dot{\varepsilon}$ for solutes and forests, respectively. Since $\tau_{\rm f} \sim 1/d_{\rm f}$ and $\Delta a_{\rm f} \sim d_{\rm f}$, we have $1/\Delta a_{\rm f} = \beta \tau_{\rm f}(\dot{\varepsilon}, T)$ leading to the well-known result

$$\frac{1}{\Delta a} = \frac{1}{\Delta a_{\rm s}} + \beta \left(\tau(\dot{\varepsilon}, T) - \tau_{\rm s}(\dot{\varepsilon}, T)\right) \tag{5.18}$$

where the slope parameter β, revealed in a Haasen plot [32], is identical to the slope parameter when the forests operate alone. However, experiments on various solute-strengthened materials at low temperature (corresponding to small $\Delta G = k_B T \ln(\dot{\varepsilon}_0/\dot{\varepsilon})$) show a slightly lower slope than measured in the pure alloy [23, 22].

At high temperatures or very low strain rate, i.e. larger values of $\Delta G = k_B T \ln(\dot{\varepsilon}_0/\dot{\varepsilon})$,

we would expect equation (5.16) to be applicable. From equation (5.16), the inverse activation area at fixed $\dot{\varepsilon}$ and T is given by

$$\frac{1}{\Delta a} = \frac{3b}{2\Delta G_{\mathrm{f}}^0} \frac{\tau - \tau_{\mathrm{b}}}{\left(\frac{k_B T \ln(\dot{\varepsilon}_0/\dot{\varepsilon})}{\Delta G_{\mathrm{f}}^0} - \frac{\Delta G_{\mathrm{s}}}{\Delta G_{\mathrm{f}}^0}\right)^{1/3} - \left(\frac{k_B T \ln(\dot{\varepsilon}_0/\dot{\varepsilon})}{\Delta G_{\mathrm{f}}^0} - \frac{\Delta G_{\mathrm{s}}}{\Delta G_{\mathrm{f}}^0}\right)} \tag{5.19}$$

where $\Delta G_{\mathrm{s}} = \Delta G_{\mathrm{s}}^0 \left(1 - (\tau_{\mathrm{b}}/\hat{\tau}_{\mathrm{s}})^{2/3}\right)^{3/2}$. In this case, the apparent yield point is τ_{b}, and plotting $1/\Delta a$ versus $\tau - \tau_{\mathrm{b}}$ yields a zero intercept in the Haasen plot, i.e., no initial activation area $1/\Delta a_{\mathrm{s}}$ at low (near-zero) forest strength. The predicted slope in equation (5.19) can be either larger or smaller than the slope when forests operate alone, depending on the experimental strain rate and the value of ΔG_{f}^0. As a consequence, our results here fail to explain the reduced Haasen slope observed in experiments for solute-strengthened alloys at larger ΔG.

With no analytical models matching experiments, we revisit simply the raw simulation data. Given the uncertainty of the simulation results, we could represent the computed activation energy as a function only of the stress variable η, at any fixed temperature, as

$$\Delta G = \Delta G_{\mathrm{s}}^0 f(\eta, \Delta G_{\mathrm{f}}^0) \tag{5.20}$$

This form neglects any dependence of ΔG on $\hat{\tau}_{\mathrm{f}}$, a dependence that is weakly indicated in our simulations. The activation area based on equation (5.20) would be

$$\frac{1}{\Delta a} = \frac{1}{\Delta a_0} + \frac{1}{\Delta a_0 \hat{\tau}_{\mathrm{s}}} \hat{\tau}_{\mathrm{f}} \tag{5.21}$$

The slope of the Haasen plot for solute-strengthening alloys would then be consistent with experiments. The intercept value $1/\Delta a_0$ would not, however, necessarily be the value corresponding to the solute-only activation area. But at low temperature and low forest strengthening, where the numerical results are in reasonable agreement with the Kocks model, the intercept value would have to asymptotically approach $1/\Delta a_0 = 1/\Delta a_{\mathrm{s}}$, and this would then agree with the low temperature experiments

of Diak et al., as shown in the reference [21]. However, the explicit form postulated by Curtin(2010) [21]

$$\Delta G = \Delta G_{\mathrm{s}}^{0} \left(1 - \eta^{2/3}\right)^{3/2} \tag{5.22}$$

does not quantitatively agree with the EO simulation results, as shown in figure 5.6, most notably failing to predcit the dependence of the activation barrier on $\Delta G_{\mathrm{f}}^{0}$. An ad-hoc form given by

$$\Delta G = \Delta G_{\mathrm{s}}^{0} \left(1 + \Delta G_{\mathrm{s}}^{0} / \Delta G_{\mathrm{f}}^{0}\right)^{1/2} \left(1 - \eta^{2/3}\right)^{3/2} \tag{5.23}$$

yields reasonable results across the entire specturm of data at high stresses, as shown in figure 5.6. This form has no formal justification and $1/\Delta a_0 \neq 1/\Delta a_{\mathrm{s}}$, but is of the form of equation (5.21) that agrees with experiments.

At elevated temperatures and low stresses, the intercept value could differ from the value of the solutes only, reflecting the influence of the forest hardening and forest activation energy. The role of temperature and of the apparent solute backstress that emerges from the simulations would complicate microscopic interpretation of the parameters obtained from the Haasen plot.

Finally, we note that we are unable to computationally probe the limit of $\hat{\tau}_{\mathrm{f}} \to 0$, i.e. when the initial forest density ρ_{f} is very low, which corresponds to the very early stages of deformation in a well-annealed alloy. Conclusions drawn about behavior occurring at low levels of forest strengthening must thus be done with caution. The simulations (figure 5.8) suggest that the backstress τ_{b} is effectively a lower-bound on the strength at finite temperature; when $\tau < \tau_{\mathrm{b}}$, the forest would contribute an activation energy $\Delta G_{\mathrm{f}}^{0}$ which is far larger than can be achieved through thermal activation. Resolution of this issue is achieved in part by considering the contributions to the strain rate from dislocation motion through the solutes in regions between the low density of forests, along with the lines of Schoeck [98], leading to an overall

strain rate

$$\dot{\varepsilon} = \rho_{\mathrm{m}} b \nu_0 \frac{1}{\sqrt{\rho_{\mathrm{f}}} \exp\left(\frac{\Delta G}{k_B T}\right) + \sqrt{\rho_{\mathrm{s}}} \exp\left(\frac{\Delta G_{\mathrm{s}}}{k_B T}\right)} \tag{5.24}$$

where ρ_{m} is the mobile dislocation density, ΔG is the overall activation energy computed from equation (5.16), ρ_{s} is the solutes density and ΔG_{s} is the activation barrier associated with solute only field. However, when ΔG is large, even at very small ρ_{f} and low $\hat{\tau}_{\mathrm{f}}$, the thermal activation energy is dominated by the forest. This conclusion is similar to Picu's [85] observation that the SRS parameter is very sensitive to the existence of 'strong' obstacles.

5.4 Summary

In summary, we have numerically and theoretically studied the plastic flow in the presence of two different obstacle strengthening mechanisms, especially focusing on the influence of a finite dislocation-obstacle interaction length on the rate- and temperature-dependent flow stress. Our results show that the linear additivity of the flow stresses due to different strengthening mechanisms can be extended from zero temperature to finite temperature only when all strengthening obstacles are point-like obstacles. Finite-length interactions between dislocation and forest obstacles becomes important when $w_{\mathrm{f}} \gg d_{\mathrm{s}}$, i.e. when the forest interaction length is longer than the spacing between the point obstacles. In this regime, the solutes appear to exert a constant backstress on the forest dislocation during the thermal activation process, and we have proposed an analytical model reflecting this behavior and agreeing well with our simulations with no adjustable parameters. We have discussed the implications of our simulations on interpretations of experimental data, in particular the activation area. Discrepancies remain between all analytical models and experiments, although a generic and ad-hoc fitting of our data could show the general trend exhibited by experiments (equation 5.23). While our simulations are perhaps the most extensive ever undertaken for this problem, the limitations of a

line-tension model, point solute obstacles, and simple extended forest obstacles, may not lead to sufficiently accurate physical insights to aid in understanding detailed thermally-activated deformation in metal alloys. This points toward more-detailed simulation methods and multiscale models as a means to capture true atomistic response of the dislocation/solute/forest-junction interactions.

Chapter 6

Summary and Conclusion

This thesis mainly contains the numerical and theoretical studies of how coupled strengthening mechanism in metal alloys operate together to generate an overall plastic resistance. The first part of this thesis focuses on the CRSS, i.e., zero-temperature flow stress due to solid-solution strengthening combined with forests strengthening, trying to explore underlying physics of previous empirical rule of mixture, $\hat{\tau}^k = \hat{\tau}_1^k + \hat{\tau}_2^k$ and provide guideline of choosing appropriate exponent k when the mixture rule is used to interpret the experimental observations.

For this purpose, we firstly use line tension simulation where strengthening obstacles are approximated as point pinning obstacles to model the dislocation glide through two types of point obstacles. One obstacle type is of weak strength but high density, corresponding to solutes strengthening; and the second obstacle type is stronger but lower density, mimicking the forests strengthening. Our results shows that additive strengthening $k = 1$ is obtained when the densities of the two obstacle types differ by more than a factor of 67, while a transition to $k = 2$ occurs with increasing density of the second obstacle, that is forest dislocations. Most importantly, we confirm clearly the long-held metallurgical wisdom regarding additivity of solute or friction strengthening with other strengthening mechanisms and also demonstrate that apparent intermediate scaling law with $1 \leq k \leq 2$ can arise for a range of rela-

tive obstacle densities, proposing that the exponent k can be evaluated by measuring the relative obstacle densities which are evolved in the hardening process.

Quantitative agreement in between the simple line tension simulation and experimental studies requires accurate line tension value of dislocation. Therefore, we developed a simple but robust method to calculate values of line tension for dislocation in metals at atomistic scale. Using the bow-out configuration obtained from loading a infinite isolated dislocation line pinned by a periodic array of immobilized atom clusters, the line tension of dislocation of different characters in various crystal structures is measured. Besides providing a reliable data set for higher-scale studies of dislocation interactions, dislocations, dislocation dynamics and models where a continuum line tension is required, our simulations conclude that an accurate line tension measurement requires a sufficient obstacle spacing, (or dislocation line length), a small obstacle size, and a sufficient applied stress. Disparate values quoted in the literatures for aluminum are shown to arise due to violation of one or more of these requirements. Furthermore, the procedure here can be easily extended further to address anisotropy line energy analysis for dislocations in solids.

The simple line tension simulation implies the interaction may exist in between individual strengthening mechanism, which results in the total strength lower than the linear summation of individual strength. Another important factor that needs be treated with care is the limitation of point-pinning assumption, which usually fail under relative high solute concentration and dislocation-junction structures. Building on these, we performed atomistic simulation to rule out the point-pinning limitation and obtained the detailed information of solute/dislocation-junction interaction with atomistic resolution. The Molecular Statics models the motion of an initial straight edge dislocation of infinite length pinned by two forest dislocations in aluminum matrix strengthened by Mg solute atoms. The numerical results shows noticeable difference compared to the DD simulations. The observed screening effect in DD due to solute hardening which reduces the junction length at free state is not observed

at atomistic scale. The solute contribution on the dislocation-junction can be very well predicted by the analytical model based on Labusch statistics. Consequently, the linear supposition rule ($k = 1$) has the ability to account for the combination of solute strengthening and dislocation-junction strengthening in metal alloys at atomistic scale. The agreement between analytical model for the solute strengthening suggests that in the frame work of multiple strengthening, the the characteristic of solute strengthening can still be defined by its Labusch length. Usually the Labusch length is in order of $\sim$10 nm, which is in the same order of magnitude of dislocation-junction length in the dislocation network. The usage of line energy analysis on dislocation junction structure has been proven successful for predicting the junction strengthes. With the atomistic numerical details in hands, combing the success of two analytical model for individual strengthening mechanisms to make further theoretical progress becomes feasible and necessary.

Thermally activated phenomena ultimately control the strain rate and temperature dependence of plastic flow and therefore the investigation of thermal activation is important. Previous simulations on this topic complicates the situation in which the zero-temperature flow stress themselves are not additive. Based on the analysis at zero temperature, we are now able to conduct kinetic Monte Carlo simulation in a regime of relative obstacle densities for which the zero-temperature stress is additive. Furthermore, the numerical methods consider the low-density "forest obstacles first as point obstacles and then as extended obstacles having a finite interaction length with the dislocation, while the high-density "solute obstacles are treated as point obstacles. Results show that the finite temperature flow stresses due to different obstacle strengthening mechanisms are additive, as proposed by Kocks et al., only when all strengthening obstacles can be approximated as point-like obstacles. When the activation distance of the low-density extended obstacles exceeds the spacing between the high-density obstacles, the finite-temperature flow stress is non-additive. Based on the simulation results, an analytical model for the activation energy ver-

sus flow stress is proposed to account for the effect of the finite interaction length. In this model, for high forest activation energies, the point-pinning solute obstacles provide a temperature-dependent backstress σ_{b} on dislocation and the overall activation energy is otherwise controlled by the forest activation energy. The model predictions agree well with numerical results for a wide range of obstacle properties, showing clearly the effect due to the finite interaction between dislocation and the obstacles. The implications of our results on the activation volume are discussed with respect to experimental results on solute-strengthened fcc alloys. While our simulations are perhaps the most extensive ever undertaken for this problem, discrepancies still remain between all analytical models and experiments. This inspires more-detailed simulation methods and multiscale models as a means to capture true atomistic response of the multiple strengthening mechanisms at finite temperature.

Bibliography

[1] A Akhtar and E Teghtsoo. Substitutional solution hardening of Magnesium single-crystals. *Philosophical Magazine*, 25(4):897–916, 1972.

[2] S. Altintas, K. Hanson, and J.W. Morris. Compter simulation of plastic deformation through palar glide in an idealized crystal. *Journal of Engineering Materials and Technology-Transactions of the ASME*, 98(1):86–91, 1976.

[3] S. Altintas and J.W. Morris. Computer simulation of dislocation glide. 1. Comparison with statistical theories. *Acta Metallurgica*, 34(5):801–807, 1986.

[4] A.S. Argon. *Strengthening Mechanisms in Crystal Plasticity*. Oxford Series on Materials Modelling. Oxford University Press, 2007.

[5] R. J. Arsenault and T. W. Cadman. Kinetics of a dislocation surmounting two different strength barries. *Physica Status Solidi A - Applied Research*, 24(1):299–304, 1974.

[6] R. J. Arsenault and S. Li. Computer-simulation of thermally activated dislocation-motion. 3. In FCC solid solutions. *Metallurgical transactions A - Physical Metallurgy and Materials Science*, 20(8):1429–1437, 1989.

[7] S. Aubry, S. P. Fitzgerald, S. L. Dudarev, and W. Cai. Equilibrium shape of dislocation shear loops in anisotropic alpha-Fe. *Modelling and Simulation in Materials Science and Engineering*, 19(6), 2011.

[8] D. J. Bacon, U.F. Kocks, and R.O. Scatterg. Effect of dislocation self-interaction on orowan stress. *Philosophical Magazine*, 28(6):1241–1263, 1973.

[9] D.J. Bacon, Osetsky Y.N., and Rodney D. Chapter 88 dislocation-obstacle interactions at the atomic level. volume 15 of *Dislocations in Solids*, pages 1 – 90. Elsevier, 2009.

[10] J.R. Beeler. *Radiation effects, computer experiments*. Defects in solids. North-Holland Pub. Co., 1983.

[11] E. Bitzek and P. Gumbsch. Dynamic aspects of dislocation motion: atomistic simulations. *Materials Science and Engineering A-Structural Materials Properties Microstructure and Processing*, 400:40–44, JUL 25 2005.

[12] E. Bitzek, P. Koskinen, F. Gaehler, M. Moseler, and P. Gumbsch. Structural relaxation made simple. *Physical review letters*, 97(170201), 2006.

[13] L. M. Brown and R. K. Ham. *Strengthening methods in crystals*, chapter Dislocation-particle interaction, pages 143–183. Applied Science Publisher, London, 1971.

[14] V. V. Bulatov, L. L. Hsiung, M. Tang, A. Arsenlis, M. C. Bartelt, W. Cai, J. N. Florando, M. Hiratani, M. Rhee, G. Hommes, T. G. Pierce, and T. D. de la Rubia. Dislocation multi-junctions and strain hardening. *Nature*, 440(7088):1174–1178, 2006.

[15] V.V. Bulatov and W. Cai. *Computer Simulations of Dislocations*. Oxford University Press, 2006.

[16] N. Buttner, K.D. Fusenig, and E Nembach. On the additivity of precipitation and solid-solution hardening in under-aged and over-aged single-crystals of (Cu-Au)-Co. *Acta Metallurgica*, 35(4):845–854, 1987.

[17] D. Caillard and J. L. Martin. *Thermally Activated Mechanisms in Crystal Plasticity*. Pergamon Materials Series. Pergamon, 2003.

[18] Q. Chen, X.Y. Liu, and S.B. Biner. Solute and dislocation junction interactions. *Acta Materialia*, 56(13):2937–2947, 2008.

[19] Y. Cheng, E. Bitzek, D. Weygand, and P. Gumbsch. Atomistic simulation of dislocation-void interactions under cyclic loading. *Modelling and Simulation in Materials Science and Engineering*, 18(2), 2010.

[20] A. H. Cottrell and R. J. Stokes. Effects of Temperature on the plastic properties of alumninium crystals. *Proceeding of the Royal Society of London series A-Mathmatical and Physical Sciences*, 233(1192):17–34, 1955.

[21] W. A. Curtin. New interpretation of the Haasen plot for solute-strengthened alloys. *Scripta Materialia*, 63(9):917–920, 2010.

[22] B. J. Diak and S. Saimoto. The determination of solute clusters in dilute aluminum alloys using strain rate sensitivity. *Materials Science and Engineering A-Structure Materials Properties Microstructure and Processing*, 234:1019–1022, 1997.

[23] B. J. Diak, K. R. Upadhyaya, and S. Saimoto. Characterization of thermodynamic response by materials testing. *Progress in Materials Science*, 43(4):223–363, 1998.

[24] L. Dupuy and M.C. Fivel. A study of dislocation junctions in FCC metals by an orientation dependent line tension model. *Acta Materialia*, 50(19):4873–4885, 2002.

[25] R. Ebeling and M. F. Ashby. Dispersion hardening of copper single crystals. *Philosophical Magazine*, 13(124):805–834, 1966.

[26] F. Ercolessi and J.B. Adams. Interatomic potentials from 1st-principle calculations - The force-matching method. *Europhysics Letters*, 26(8):583–588, 1994.

[27] R. L. Fleischer. Substitutional solution hardening. *Acta Metallurgica*, 11(3):203 – 209, 1963.

[28] P. S. Follansbee and U. F. Kocks. A constitutive description of the deformation of copper based on the use of the mechanical threshold stress as an internal state variables. *Acta Metallurgica*, 36(1):81–93, 1988.

[29] A Foreman and M.J. Makin. Dislocation movement through random arrays of obstacles. *Philosophical Magazine*, 14(131):911–924, 1966.

[30] A Foreman and M.J. Makin. Dislocation movement through random arrays of obstacles. *Canadian Journal of Physis*, 45(2P2):511–517, 1967.

[31] J. Friedel. *Dislocations*. International series of monographs on solid state physics. Pergamon Press, 1964.

[32] P. Haasen. Plastic deformation of nickel single crystals at low temperatures. *Philosophical Magazine*, 3(28):384–418, 1958.

[33] P. Haasen. *Physical Metallurgy*. Cambridge University Press, 1996.

[34] K. Hanson, S. Altintas, and Jr. Morris, J. W. Computer simulation of dislocation glide through fields of point obstacles. In *Proceedings Fifteenth Annual ACM*, volume 20 of *Conference on computer simulation for materials applications*, pages 917–928, Gaithersburg, MD, USA, 1976.

[35] K. Hanson and Jr. J. W. Morris. Estimation of the critical resolved shear stress for dislocation glide through a random mixture of distinct obstacles. *Journal of Applied Physics*, 46(6):2378–2383, 1975.

[36] K. Hanson and Jr. J. W. Morris. Limiting configuration in dislocation glide through a random array of point obstacles. *Journal of Applied Physics*, 46(3):983–990, 1975.

[37] K. Hardikar, V. Shenoy, and R. Phillips. Reconciliation of atomic-level and continuum notions concerning the interaction of dislocations and obstacles. *Journal of the Mechanics and Physics of Solids*, 49(9):1951–1967, 2001.

[38] M. Hiratani and V. V. Bulatov. Solid-solution hardening by point-like obstacles of different kinds. *Philosophical Magazine Letter*, 84(7):461–470, 2004.

[39] M. Hiratani, H. M. Zbib, and B. D. Wirth. Interaction of glissile dislocations with perfect and truncated stacking-fault tetrahedra in irradiated metals. *Philosophical Magazine A-Physics of Condensed Matter Structure Defects and Mechanical Properties*, 82(14):2709–2735, 2002.

[40] P. B. Hirsch and F. J. Humphreys. The deformation of single crystals of copper and copper-zinc alloys containing alumina particles. i. macroscopic properties and workhardening theory. *Proceedings of the Royal Society of London. A. Mathematical and Physical Sciences*, 318(1532):45–72, 1970.

[41] J. P. Hirth. On dislocation interactions in the fcc lattice. *Journal of Applied Physics*, 32(4):700–706, 1961.

[42] J.P. Hirth and J. Lothe. *Theory of dislocations*. Krieger Pub. Co., 1982.

[43] D. Hull and D.J. Bacon. *Introduction to Dislocations*. Materials science. Butterworth-Heinemann, 2001.

[44] Jr. J. W. Morris and D. H. Klahn. Statistics of the thermally activated glide of a dislocation through a random array of point obstacles. *Journal of Applied Physics*, 44(11):4882–4890, 1973.

[45] Jr. J. W. Morris and C. K. Syn. Point-obstacle representation of the dislocation-obstacle interaction. *Journal of Applied Physics*, 45(2):961–963, 1974.

[46] Honeycutt J.D. and H.C. Andersen. Molecular-dynamics study of melting and freezing of small lennard-jones clusters. *Journal of Physical Chemistry*, 91(19):4950–4963, 1987.

[47] D. Klahn, D. Austin, A. K. Mukherjee, and J. E. Dorn. The importance of geometric statistics to dislocation motion. *Advances in Applied Probability*, 4:pp. 112–150, 1972.

[48] U. F. Knocks. Strength of metals and alloys. volume 3 of *Proceedings of the Fifth International Conference in the Strength of Metals*, pages 1661–1680, 1979.

[49] U. F. Kocks. Kinetics of solution hardening. *Metallurgical Transactions A-Physical Metallurgy and Materials Science*, 16(12):2109–2129, 1985.

[50] U. F. Kocks, A. S. Argon, and M. F. Ashby. Thermodynamicsand kinetic of slip. *Progress in Materials Science*, 19:1–281, 1975.

[51] U. F. Kocks and H. Mecking. Physics and phenomenology of strain hardening: the FCC case. *Progress in Materials Science*, 48(3):171–273, 2003.

[52] U.F. Kocks. Statistical treatmen of penetrable obstacles. *Canadian Journal of Physics*, 45(2):737–755, 1967.

[53] T. J. Koppenaal and K. Kuhlmann-Wilsdorf. The effect of prestressing on the strength of neutron-irradiated copper single crystals. *Applied Physics Letters*, 4(3):59–61, 1964.

[54] R. Labusch. A statistical theory of solid solution hardening. *Physica Status Solidi (b)*, 41(2):659–669, 1970.

[55] R. Labusch. Statistical theory of dislocation configurations in a random array of point obstacles. *Journal of Applied Physics*, 48(11):4550–4556, 1977.

[56] U. Lagerpusch, V. Mohles, D. Baither, B. Anczykowski, and E. Nembach. Double strengthening of copper by dissolved gold-atoms and by incoherent SiO2-particles: How do the two strengthening contributions superimpose? *Acta Materialia*, 48(14):3647–3656, 2000.

[57] G. P. M. Leyson, W. A. Curtin, L. G. Hector, Jr., and C. F. Woodward. Quantitative prediction of solute strengthening in aluminium alloys. *Nature Materials*, 9(9):750–755, 2010.

[58] G. P. M. Leyson, L. G. Hector, Jr., and W. A. Curtin. First-principles prediction of yield stress for basal slip in mg-al alloys. *Acta Materialia*, (unpublished), 2012.

[59] G. P. M. Leyson, L. G. Hector, Jr., and W. A. Curtin. Solute strengthening from first principles and application to aluminum alloys. *Acta Materialia*, 60(9):3873–3884, 2012.

[60] X.Y. Liu, J.B. Adams, F. Ercolessi, and J.A. Moriarty. EAM potential for magnesium from quantum mechanical forces. *Modelling and Simulation in Materials Science and Engineering*, 4(3):293–303, 1996.

[61] X.Y. Liu, P.P. Ohotnicky, J.B. Adams, C.L. Rohrer, and R.W. Hyland. Anisotropic surface segregation in Al-Mg alloys. *Surface Science*, 373(2-3):357–370, 1997.

[62] R. Madec, B. Devincre, L. Kubin, T. Hoc, and D. Rodney. The role of collinear interaction in dislocation-induced hardening. *Science*, 301(5641):1879–1882, 2003.

[63] R. Madec, B. Devincre, and L.P. Kubin. From dislocation junctions to forest hardening. *Physical Review Letters*, 89(25), 2002.

[64] G. Monnet. Investigation of precipitation hardening by dislocation dynamics simulations. *Philosophical Magazine*, 86(36):5927–5941, 2006.

[65] G. Monnet. Mechanical and energetical analysis of molecular dynamics simulations of dislocation-defect interactions. *Acta Materialia*, 55(15):5081–5088, 2007.

[66] G. Monnet and B. Devincre. Solute friction and forest interaction. *Philosophical Magazine*, 86(11):1555–1565, 2006.

[67] J. W. Morris and D. H. Klahn. Thermally activated dislocation glide through a random array of point obstacles-computer-simulation. *Journal of Applied Physics*, 45(5):2027–2038, 1974.

[68] N.F. Mott and F.R.N. Nabarro. Dislocation theory and transient creep. Physical Society Bristol Conf. Report, pages 1 – 19, 1948.

[69] R. A. Mulford. Analysis of strengthening mechanisms in alloys by means of thermal-activation theory. *Acta Metallurgica*, 27(7):1115–1124, 1979.

[70] R. A. Mulford and U. F. Kocks. Effect of solute on the obstacle profiles for dislocation interaction and solution strengthening in Ni-alloys. *Scripta Metallurgica*, 13(8):729–732, 1979.

[71] R. A. Mulford and U. F. Kocks. New observations on the mechanisms of dynsmic strain aging and jerky flow. *Acta Metallurgica*, 27(7):1125–1134, 1979.

[72] F Nabarro. Dislocations in a simple cubic lattice. *Proceedings of the Physical Society*, 59(332):256–272, 1947.

[73] G. Neite, M. Sieve, M. Mrotzek, and E. Nemback. Deformation of multi-phase and particle-containing materials. In *Proceedings of the 4th Risϕ International Symposium on Metallurgy and Materials Science*, page 447, Gaithersburg, MD, USA, 1983.

[74] E Nembach and C.K. Chow. Experimental investigation into the relation between $\gamma\prime$ particle dispersion and the yield stress of PE16. *Materials Science and Engineering*, 36(2):271–279, 1978.

[75] E. Nembach and M. Martin. Superposition of solid-solution and particle strengthening in (Cu-Au)-Co single-crystals. *Acta Metallurgica*, 28(8):1069–1075, 1980.

[76] T. Nogaret, W. A. Curtin, J. A. Yasi, L. G. Hector, Jr., and D. R. Trinkle. Atomistic study of edge and screw ¡ c plus a ¿ dislocations in magnesium. *Acta Materialia*, 58(13):4332–4343, 2010.

[77] T. Nogaret, C. Robertson, and D. Rodney. Atomic-scale plasticity in the presence of Frank loops. *Philosophical Magazine*, 87(6):945–966, 2007.

[78] T. Nogaret and D. Rodney. Finite-size effects in dislocation glide through random arrays of obstacles: Line tension simulations. *Physical Review B*, 74(13), 2006.

[79] D.L. Olmsted, K.Y. Hardikar, and R. Phillips. Lattice resistance and Peierls stress in finite size atomistic dislocation simulations. *Modelling and Simulation in Materials Science and Engineering*, 9(3):215–247, 2001.

[80] D.L. Olmsted, L.G. Hector, and W.A. Curtin. Molecular dynamics study of solute strengthening in Al/Mg alloys. *Journal of the Mechanics and Physics of Solids*, 54(8):1763–1788, 2006.

[81] Y.N. Osetsky and D.J. Bacon. An atomic-level model for studying the dynamics of edge dislocations in metals. *Modelling and Simulation in Materials Science and Engineering*, 11(4):427–446, 2003.

[82] S. Patinet and L. Proville. Depinning transition for a screw dislocation in a model solid solution. *Physical Review B*, 78(10), 2008.

[83] R Peierls. The size of a dislocation. *Proceedings of the Physical Society*, 52(Part 1):34–37, 1940.

[84] R. C. Picu and R. Li. On the superposition of flow stress contributions at finite temperatures and in the athermal limit. *Acta Materialia*, 58(16):5443–5446, 2010.

[85] R. C. Picu, R. Li, and Z. Xu. Strain rate sensitivity of thermally activated dislocation motion across fields of obstacles of different kind. *Materials Science and Engineering A-Structural Materials Properties Microstructure and Processing*, 502(1-2):164–171, 2009.

[86] R. C. Picu and M. A. Soare. Asymmetric dislocation junctions exhibit a broad range of strengths. *Scripta Materialia*, 62(7):508–511, 2010.

[87] L. Proville and S. Patinet. Atomic-scale models for hardening in fcc solid solutions. *Physical Review B*, 82:054115, 2010.

[88] L. Proville, D. Rodney, Y. Brechet, and G. Martin. Atomic-scale study of dislocation glide in a model solid solution. *Philosophical Magazine*, 86(25-26):3893–3920, 2006.

[89] S. Queyreau, G. Monnet, and B. Devincre. Orowan strengthening and forest hardening superposition examined by dislocation dynamics simulations. *Acta Materialia*, 58(17):5586–5595, 2010.

[90] S. Rao, T. A. Parthasarathy, and C. Woodward. Atomistic simulation of cross-slip processes in model fcc structures. *Philosophical Magazine A-Physics of Condensed Matter Structure Defects and Mechanical Properties*, 79(5):1167–1192, 1999.

[91] B. Reppich, Kuhliein W., G. Meyer, D. Puppel, M. Schulz, and G. Schumann. Duplex γ praticle hardening of the superalloy nimonic PE-16. *Materials Science and Engineering*, 83(1):45–63, 1986.

[92] E. Rodary, D. Rodney, L. Proville, Y. Brechet, and G. Martin. Dislocation glide in model Ni(Al) solid solutions by molecular dynamics. *Physical Review B*, 70(5), 2004.

[93] D. Rodney. Molecular dynamics simulation of screw dislocations interacting with interstitial frank loops in a model FCC crystal. *Acta Materialia*, 52(3):607–614, 2004.

[94] D. Rodney and G. Martin. Dislocation pinning by glissile interstitial loops in a nickel crystal: A molecular-dynamics study. *Physical Review B*, 61:8714–8725, 2000.

[95] D Rodney and R Phillips. Structure and strength of dislocation junctions: An atomic level analysis. *Physical Review Letters*, 82(8):1704–1707, 1999.

[96] Plimpton S. Fast parallel algorithms for short-range molecular-dynamics. *Journal of Computational Physics*, 117(1):1–19, 1995.

[97] G Saada. On the interaction between a fixed dislocation and a mobile dislocation in its slip plane. *Acta Metallurgica*, 8(3):200–208, 1960.

[98] G. Schoeck. The superposition of thermal-activation in dislocation movement. *Physica Status Solidi A-Applied Research*, 87(2):571–581, 1985.

[99] R. B. Schwarz and R. Labusch. Dynamic simulation of solution hardening. *Journal of Applied Physics*, 49(10):5174–5187, 1978.

[100] V. B. Shenoy, R. V. Kukta, and R. Phillips. Mesoscopic analysis of structure and strength of dislocation junctions in fcc metals. *Physical Review Letters*, 84(7):1491–1494, 2000.

[101] V. B. Shenoy and R. Phillips. Finite-sized atomistic simulations of screw dislocations. *Philosophical Magazine A-Physics of Condensed Matter Structure Defects and Mechanical Properties*, 76(2):367–385, 1997.

[102] M. A. Soare and R. C. Picu. Multiscale modeling of the negative strain-rate sensitivity in solid solutions: A constitutive formulation. *International Journal for Multiscale Computational Engineering*, 3(4):415–435, 2005.

[103] S. G. Srinivasan, X. Z. Liao, M. I. Baskes, R. J. McCabe, Y. H. Zhao, and Y. T. Zhu. Compact and dissociated dislocations in aluminum: Implications for deformation. *Physical Review Letters*, 94(125502), 2005.

[104] A. Stukowski. Visualization and analysis of atomistic simulation data with OVITO-the Open Visualization Tool. *Modelling and Simulation in Materials Science and Engineering*, 18(1), 2010.

[105] D. Y. Sun, M. I. Mendelev, C. A. Becker, K. Kudin, Tomorr Haxhimali, M. Asta, J. J. Hoyt, A. Karma, and D. J. Srolovitz. Crystal-melt interfacial free energies in hcp metals: A molecular dynamics study of mg. *Physical Review B*, 73:024116, 2006.

[106] D. Terentyev, D. J. Bacon, and Yu N. Osetsky. Interaction of an edge dislocation with voids in alpha-iron modelled with different interatomic potentials. *Journal of Physics: Condensed Matter*, 20(44), 2008.

[107] L.K. Wickham, K.W. Schwarz, and J.S. Stolken. Rules for forest interactions between dislocations. *Physical Review Letters*, 83(22):4574–4577, 1999.

[108] C. Woodward, D. R. Trinkle, L. G. Hector, Jr., and D. L. Olmsted. Prediction of dislocation cores in aluminum from density functional theory. *Physical Review Letters*, 100(045507), 2008.

[109] Z. Xu and R. C. Picu. Thermally activated motion of dislocations in fields of obstacles: The effect of obstacle distribution. *Physical Review B*, 76(9), 2007.

[110] J. A. Yasi, T. Nogaret, D. R. Trinkle, Y. Qi, L. G. Hector, Jr., and W. A. Curtin. Basal and prism dislocation cores in magnesium: comparison of first-principles and embedded-atom-potential methods predictions. *Modelling and Simulation in Materials Science and Engineering*, 17(055012), 2009.

[111] S. J. Zhou, D. L. Preston, P. S. Lomdahl, and D. M. Beazley. Large-scale molecular dynamics simulations of dislocation intersection in copper. *Science*, 279(5356):1525–1527, 1998.

[112] A. W. Zhu, A. Csontos, and E. A. Starke. Computer experiment on superposition of strengthening effects of different particles. *Acta Materialia*, 47(6):1713–1721, 1999.

[113] A. W. Zhu and E. A. Starke. Strengthening effect of unshearable particles of finite size: A computer experimental study. *Acta Materialia*, 47(11):3263–3269, 1999.